8-2017

DESIGN AND EXPERIMENTATION OF CABLE-DRIVEN PLATFORM STABILIZATION AND CONTROL SYSTEMS

Matthew Newman
University of Nebraska - Lincoln, mbnewman91@gmail.com

DESIGN AND EXPERIMENTATION OF CABLE-DRIVEN PLATFORM STABILIZATION AND CONTROL SYSTEMS

by

Matthew Newman

A THESIS

Presented to the Faculty of

The Graduate College at the University of Nebraska

In Partial Fulfillment of Requirements

For the Degree of Master of Science

Major: Mechanical Engineering and Applied Mechanics

Under the Supervision of Professor Ben Terry

Lincoln, Nebraska

August, 2017

DESIGN AND EXPIREMENTATION OF CABLE-DRIVEN PLATFORM STABILIZATION AND CONTROL

Matthew Newman, M.S.

University of Nebraska, 2017

Advisor: Benjamin S. Terry

Agricultural researchers are constantly attempting to generate crops superior to those currently in use by the world. Whether this means creating crops with greater yield, crops that are more resilient to disease, or crops that can tolerate harsh environments with fewer failures, test plots of these experimental crops must be studied in real-world environments with minimal invasion to determine how they will perform in full-scale agricultural settings. To monitor these crops without interfering on their natural growth, a noninvasive sensor system has been implemented. This system, instituted by the College of Agricultural Sciences and Natural Resources at the University of Nebraska – Lincoln, uses a network of cables to support and maneuver a sensor platform above the crops at an outdoor phenotyping site.

In this work, a cable-driven parallel robot (CDPR) to be used by the university's agricultural researchers is modeled for static behavior. This model is then compared to scaled-down CDPRs to confirm its accuracy. Second, the scaled-down CDPRs are used to study the dynamics of cable systems, test scaled-down end-effectors, and develop a CDPR control scheme. Third, a novel stabilization system is developed to maintain sensor platform orientation, improving data collection by use of a multirotor stabilization

system. Multiple prototype systems are developed and experimented with to determine the capabilities and limitations of such a system. Finally, a portable CDPR system for use in remote fields is analyzed for cost feasibility and design considerations.

ACKNOWLEDGEMENTS

Gratitude goes out to Yue Sun and Iman Salafian for their research into cable driven robotic dynamics and designs. Gratitude also goes out to Blake Stewart, Weston Lewis, and Alex Schueth for their aid in the design of robot devices and the conduction of multiple system experiments.

The author wishes to acknowledge Dr. Benjamin S. Terry and Dr. Art Zygielbaum for their advice and counsel in the design of these systems.

Table of Contents

List of Figures

CHAPTER 1. INTRODUCTION

The research presented in this report centers around the design of a cable-driven field phenotyping facility. The research focused on the design, modeling, and optimization of the cable system as well as the development of a stabilization system for suspended payloads. What follows is an introduction to phenotyping and the current state of the art in this field.

1.1 Phenotypic Research

Agricultural productivity is dependent on the development of crops that can meet certain requirements, such as resilience in the face of environmental or pest stressors, or a level of productivity (yield) despite restrictions in nutrients or water. Breeding such crops is an iterative process where the result of crossing the genes of sets of plants causes measureable changes in successive generations. These changes are determined by measuring the plants' phenotypes – observable characteristics [1]–[5].

Phenotyping in a greenhouse can now be done rapidly using automated equipment. Many commercial greenhouse systems are available. One company that has been used by the University of Nebraska – Lincoln for its greenhouses is LemnaTec. This particular company offers a variety of agricultural sensory systems (see Figure 1-1) for use in both laboratory and greenhouse settings [6], [7]. Plants grown under these controlled conditions, however, are different from plants grown in an outdoor field environment. Outdoors, light conditions are different, soils are less uniform, and wind encourages the growth of support structures within the plants. Assuring that measurements in a greenhouse are trustworthy predictions of field performance is an important aspect of

phenotyping. To this end, field-grown plants must be studied to evaluate their growth in real-world, agricultural conditions.

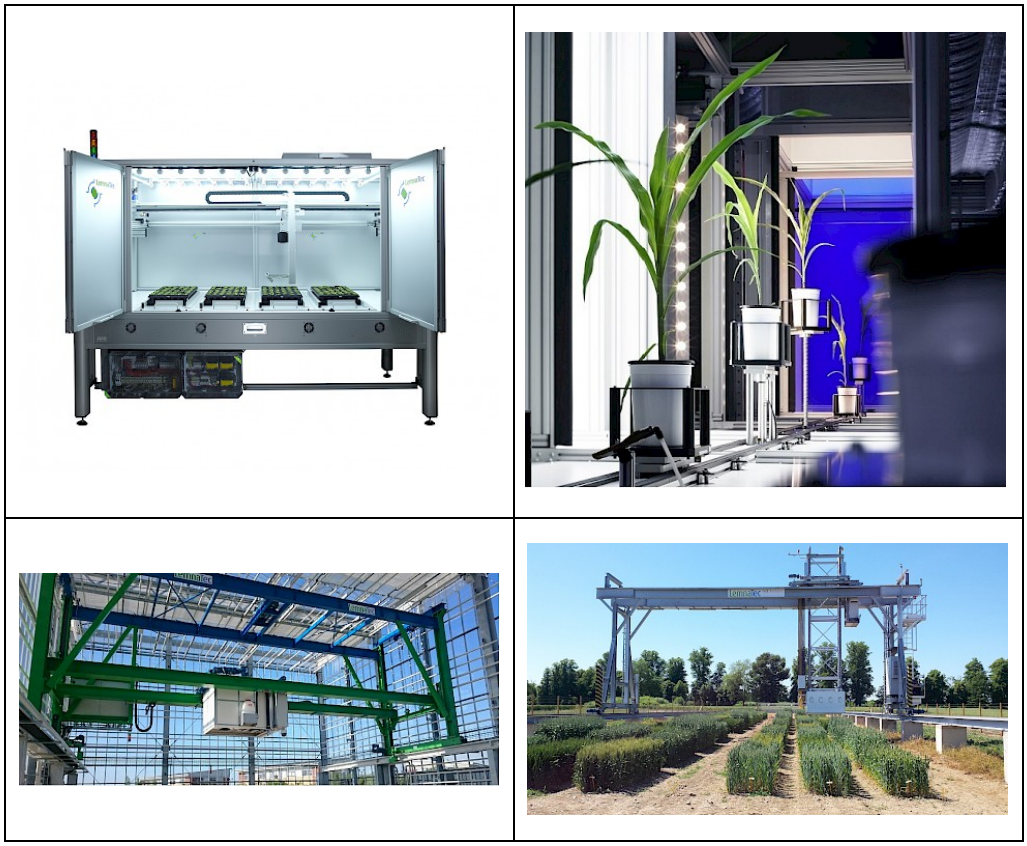

Figure 1-1. LemnaTec Systems. (top-left) Lab system. [7] (top-right) Greenhouse conveyor system. [6] (bottom-left) Greenhouse gantry. [6] (bottom-right) Outdoor gantry. [8]

While LemnaTec and other companies offer methods to study field crops [8], [9], they all offer significant restraints. For example, the outdoor gantry system designed by LemnaTec (Figure 1-1) is capable of rigidly supporting a large sensor platform for reliable data collection. However, the system works by driving the system down a set of rails along either side of an isle of crops. As a result, the width of the field a system can monitor is limited by the system's structure. Additionally, the structural supports of the system cast shadows and reflections that can impact imaging quality as well as affect plant growth. Other methods of collecting data in the field include manual data

collection, where researchers walk through the field with an equipment backpack and sensors mounted to the end of a long rod (Figure 1-2). They may also use a sensor package fixed to the end of a long arm, extending from a large vehicle that drives down the aisles of a field or around the perimeter (Figure 1-2). The backpack system requires many man-hours, and the user must walk through the field, interfering with the crops. The vehicle system can cast significant shadows and reflections over the field as well as generate significant heat and fumes that may affect plant growth. It also requires a large, expensive vehicle as well as a field designed to accommodate it.

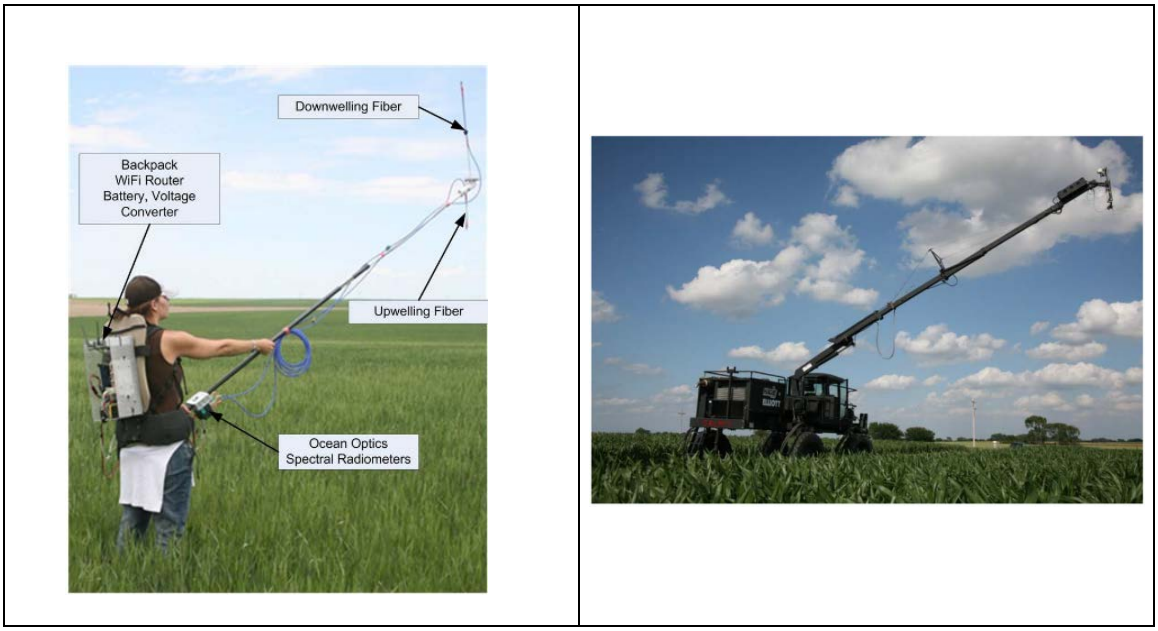

Figure 1-2. Alternate field phenotyping methods. (left) Manual field phenotyping. (right) Hercules research platform. [9]

These examples all exhibit the primary limitations of most field phenotyping systems: scalability of implementation and interference with the plants. To study larger fields with minimal invasion, two primary methods have been used by researchers to collect data.

The first method involves the use of unmanned aerial vehicles (UAVs) as in Figure 1-3. The concept is to use one or more UAVs (fixed-wing, helicopter, or multirotor vehicles) to make passes over the field and collect data [10]–[14]. The data can then be retrieved from the vehicle for later research. The benefits to this system are minimal hardware – compared to terrestrial vehicles or field-size gantries – no required construction, scalability to any size of field, the potential for system automation, and the availability of commercial technology.

Figure 1-3. Agricultural drone. [15]

However, there are significant obstacles with this methodology. First, due to the increased use of UAVs, or drones, in recent years for both commercial and recreational uses, many regulations have been passed to limit their use [16]. Most notably, the FAA requires commercial users to possess a Pilot Airman Certificate to operate the drone. Another significant challenge presented by the use of drones is safety. Using a drone continuously throughout the day, every day, leads to a high probability of hardware malfunction that could cause the device to crash, potentially damaging itself, the crops,

surrounding structures, or personnel in the area. As a result the FAA also requires the operator to remain within line-of-sight with the device and it may not fly over personnel. [17]

Different types of drones also have their own specific limitations. For example, traditional fixed-wing UAVs by design are required to be in constant motion to remain in the air. As a result, they can only be used for high altitude shots due to the relative speed of the camera field of view and would be best suited for field-wide images as opposed to images of specific plants. Multirotor systems, such as quadcopters, are capable of hovering, allowing them to stay in place above a specific plant. However, several key challenges have been found when using multirotor systems. First, the airflow from the rotors creates a downwash, or rush of air downwards, towards the crops that can cause the plants to sway, disrupting the data collection and potentially damaging the plants. Additionally, the device can have difficulties remaining stationary during scanning when exposed to extensive wind, a significant problem in Nebraska [18]–[20]. The final challenge, and one that applies to all UAVs, is flight time. Typically, these devices are intended for flights of up to a few minutes for multirotor systems or possibly a few hours for fixed wing drones or high-end multirotor drones. Researchers generally want to be able to continuously monitor crops. Taking the time to replace batteries on a quadcopter a few times an hour can greatly inhibit a researcher's ability to obtain continuous, consistent data.

High endurance and high precision vehicles are under development by several companies. The Hercules, available for pre-order at the time of writing, is a

gasoline/battery hybrid copter designed by Advanced Aircraft Company. IT is intended to be capable of supporting a nine pound payload for up to 3.5 hours, and one of its intended applications is precision agriculture [21]. While drone technology will continue to advance in the future, current technology is still limited, primarily by FAA regulations, safety restriction, and reliability. As a result, work continues to develop an alternative to drone-based phenotyping.

Besides UAVs, one other method of field-based phenotyping data collection has received significant attention in recent years. That method is the use of a multi-cable support system to position a suspended payload over a field. The cables are then actuated by a network of winches to reposition the end-effector within the field's workspace. Similar devices have been used for years for multiple processes. Most recently, The Chinese Academy of Sciences has developed a 500 meter aperture telescope known as FAST. This system, modeled in Figure 1-4, uses six cables to position the cabin above the reflective dish below [22], [23].

Figure 1-4. FAST 500 meter aperture radio cable system. [17]

These systems offer several benefits over both gantry and UAV based phenotyping systems. First, while this system requires rigid support structures, they are much smaller than those for similarly sized gantry systems. Therefore, it has the potential to be considerably cheaper to construct and simpler to scale to larger fields. Larger fields only require taller or stronger towers to support the cable system over greater distances. The actuation of the end-effector is accomplished with cables, which are cheap, low-weight alternatives to large, steel beams. Additionally, the cables and significantly smaller end-effector cast smaller shadows and fewer reflections than the large gantry components. The system is also capable of moving at higher speeds than a gantry system as the moving mass is much smaller. This can lead to faster scan times and more consistent data throughout the field.

The primary disadvantage that this system has is its lack of rigidity [24]. Due to the support of the end-effector through long cables, wind and system acceleration can induce vibrations that can deflect the end-effector, impairing data collection. Additionally, supplying power to the end-effector becomes a challenge when there is no rigid framing to attach the power system to. Three primary methods are available for transporting power to a suspended end-effector. The first method is to use batteries built into the end-effector. This requires constant maintenance to charge or replace batteries. Additionally, the additional weight of the batteries can have a negative impact on the structural requirements of the system. The second method is to drape power cables from the support cables, as done by the FAST system [22]. See Figure 1-5. This method allows for continuous operation of the system without switching batteries; however, the draping of the wire alters the behavior of the support cables, causing modeling and control complications. These complications become more prevalent as the support cable shortens, causing large amounts of power cable to bunch up, potentially tangling.

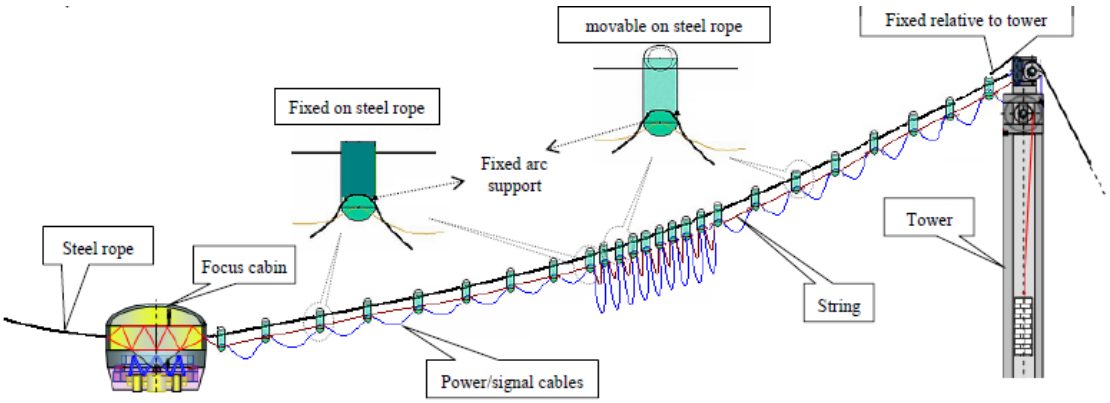

Figure 1-5 FAST power delivery system. [22]

The final method of power delivery investigated by this work involves passing a conductive core cable through the center of the support cables to supply power to the end-effector. Due to its potential for continuous operation and the fact that the cables have consistent properties along their lengths since the conductive cable is not draped across its length, this method has the potential to be the least obstructive method of the three. However, it does offer complications as passing the conductor through the support cable would increase the cable's weight and stiffness. It also requires power to be passed through the winch used to actuate the cable, requiring a slip ring in the winch as well as several secondary considerations.

The primary advantages that a cable-driven system has over a UAV are reliability and unrestricted time of operation. In the case of hardware malfunction or power loss, the UAV would be unable to support the payload, causing it to fall, damaging itself, crops, or personnel. In the case of hardware malfunction or power loss for the cable robot, the system may be inoperable, but as long as proper safety measures are taken to ensure that the winches are incapable of breaking the cables and that power loss causes the winches'

brakes to be applied, the payload should remain secure. Additionally, because the system is fixed to the ground, power can be supplied to the system without batteries, allowing for continuous operation. Cable systems also do not involve the legal requirements of commercial UAV flight. Lastly, anend-effector is capable of lowering all the way into the canopy of its crops without disrupting them with large amounts of airflow.

1.2 Cable system Design Considerations

One cable-driven phenotyping system (shown in Figure 1-6) has already been built in Zurich, Switzerland by the Swiss Federal Institute of Technology (ETH) and has been used for phenotypic research for a few years. While the infrastructure (towers, shelters, power system, and irrigation system) are custom made, the cable system and end-effector were developed through a partnership with Spidercam, a company that has historically provided cable-driven camera systems to sport venues [25].

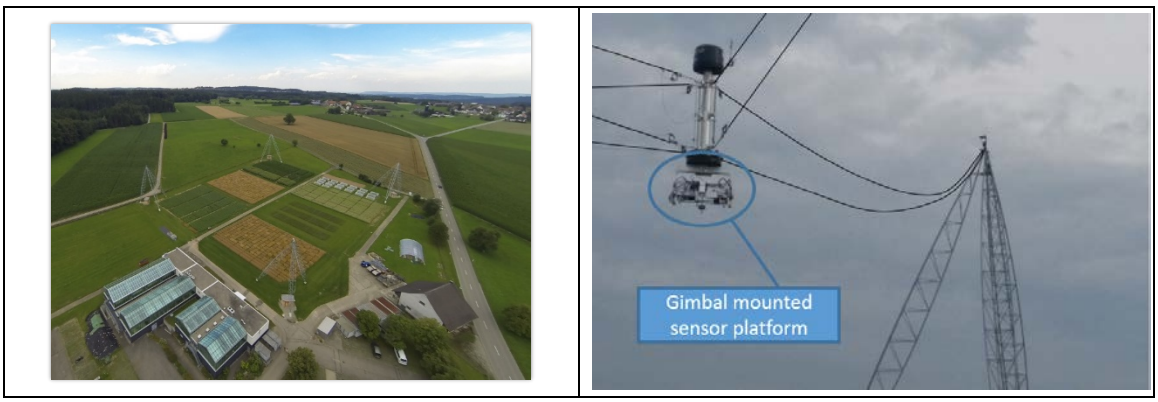

Figure 1-6. ETH phenotyping system. (left) Aerial view of facility. (right) System end-effector.

This system uses eight cables supported by four towers surrounding the field. The end-effector main body consists of a rigid structure that houses equipment, such as batteries to power the sensors located on its lower platform, and connects to the eight support cables. The lower half of the end-effector, or the sensor platform, consists of a plate attached to

the main body of the end-effector through a two-axis active gimbal. This gimbal allows for the reorientation of the sensor platform with respect to the main body of the end-effector. This is required because the main body of the end-effector tilts as it approaches the edges of the workspace, distorting the sensor platform's orientation (see below for further detailes).

Although this is an eight-cable system, it remains an over constrained, three degree-of-freedom robot. As covered in detail by Hiller [26], a robot capable of moving in three-dimensional space requires three cables to be fully constrained. To control position and orientation of an end-effector – in other words, a six degree-of-freedom robot – requires six cables. The first question concerning the design of the ETH system is, why are four cables used instead of three or six? While three cables are capable of positioning an end-effector to a given position, fields are typically constructed in a rectangular or circular workspace. As Figure 1-7 illustrates, a three-cable system requires the towers to be positioned far outside of the workspace compared to four or even six cables.

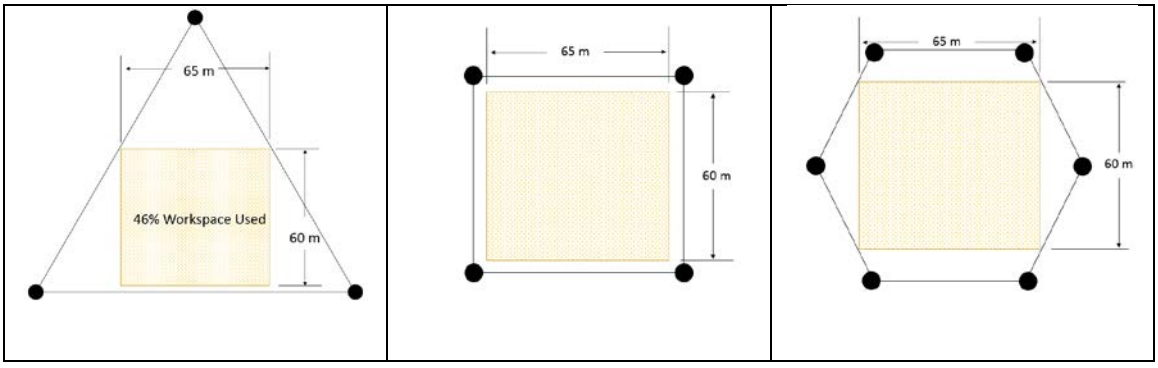

Figure 1-7. Potential cable system layouts. (left) Three-tower system. (center) Four-tower system. (right) Six-tower system.

While the six-tower system could theoretically allow for six degree-of-freedom control of the end-effector, in practice, this would likely prove difficult due to the geometry of the

workspace and flexibility of the cables. Additionally, it would require the construction of two additional winches and towers, increasing system cost. Therefore, using four towers becomes a compromise between spacial and fiscal efficiency.

As shown by Figure 1-6, the ETH system was built using eight cables, two from each of the four towers. The purpose of this setup was to attempt to restrict the motion of the end-effector, maintaining its vertical orientation. As explored further in later chapters, as an end-effector approaches the boarders of its workspace when using a three degree-of-freedom cable robot, the end-effector begins to tilt, pitching towards the center of the field. It is believed that the eight-cable system was designed to prevent this.

In rigid robot design, if a four bar linkage is designed so that opposing linkages are of the same length, as in Figure 1-8, they will remain parallel, regardless of length or orientation.

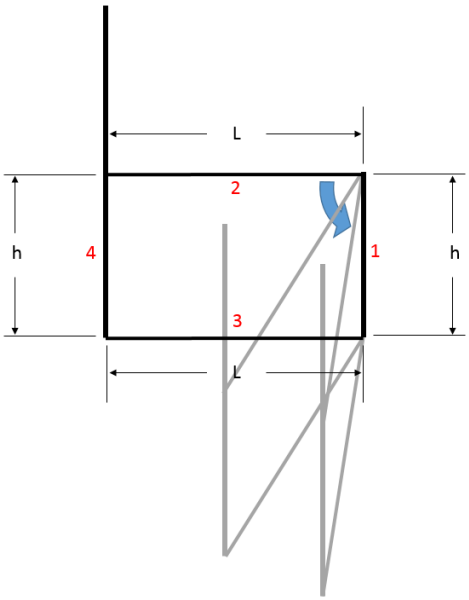

Figure 1-8. Parallel rigid linkage concept.

Based on this concept, linkages two and three may be extended or shortened, allowing linkage four (in the case of the robot, this would be the end-effector) to move while remaining vertical, as in Figure 1-9. However, in the case of flexible linkages with significant sag, this is not true. When using flexible linkages, the uneven distribution of load between linkages two and three causes one to extend more than the other, causing them to no longer be of the same length. As a result, linkage four, or the end-effector, pitches toward the center of the workspace. This was seen in the ETH system, as in Figure 1-10. The system designed by Spidercam for the ETH system implemented this concept by creating winches with two drums that would feed two cables at the same rate.

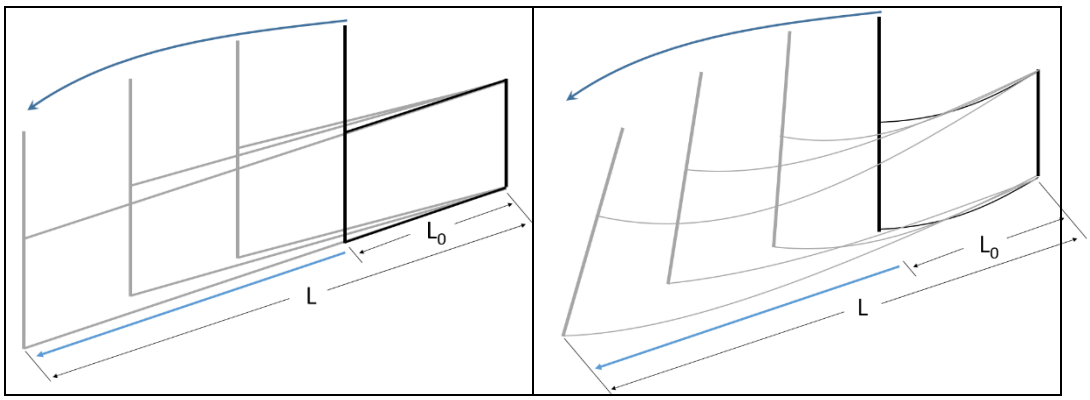

Figure 1-9. Parallel linkage motion. (left) Rigid linkages. (right) Flexible linkages.

While this system offers some restraint as opposed to supporting the system with only three or four cables, it has been shown to not maintain orientation. As a result, the cable system focused on as a part of this research only use four cables to support the end-effector and alternative methods are researched to maintain end-effector orientation.

Figure 1-10. ETH end-effector experiencing tilt as it approaches the edge of workspace.

While the use of eight cables was not continued as a part of this research, a method was developed early on that would allow for their use to orient the end-effector without the expense of adding four additional winches. As illustrated by Figure 1-11, a single winch

can be used to rotate two drums, feeding both the blue and the orange cables at the same rate, as with the ETH system. However, unlike the ETH system, the orange cable can pass through a network of sheaves before reaching the end-effector. By actuating one of the sheaves, cable spanning from the tower to the end-effector would be drawn in or released, causing the bottom of the end-effector to shift. The blue cables can then be thought to support the end-effector and control its position while the orange cables possess limited control over the end-effector orientation. This would only require four linear actuators as opposed to four additional winches for the same control.

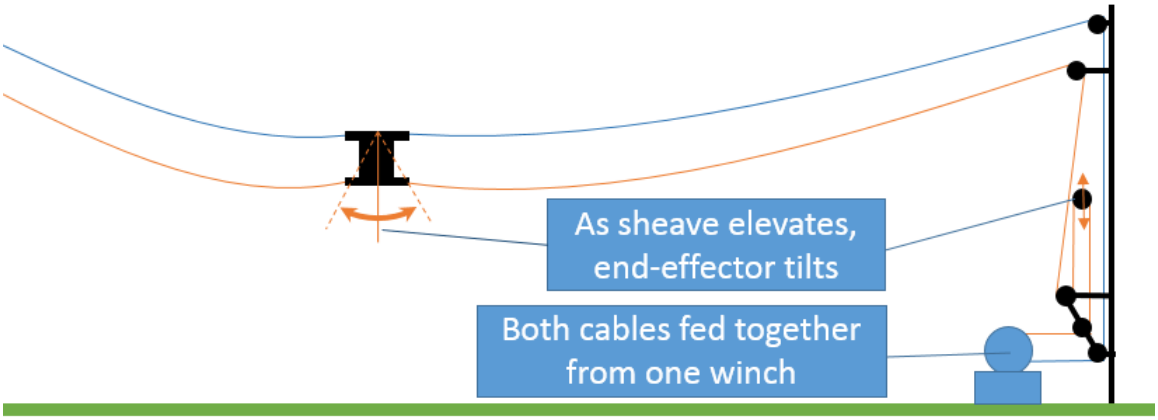

Figure 1-11. Eight-cable system using four winches.

This method was eventually abandoned when the University of Nebraska decided to partner with Spidercam to develop their system as it would have involved a significant amount of integration between University and Spidercam designs. It was instead decided that the University would focus on the end-effector and system infrastructure while Spidercam would focus on the cable and control systems.

CHAPTER 2. CABLE-DRIVEN ROBOT STATIC ANALYSIS

To better understand the future behavior of the phenotyping system, extensive modeling was conducted for cable suspended systems. These models were used to predict static system behavior and to develop the optimal system design.

2.1 Background

A cable-driven parallel robot (CDPR) is a robotic manipulator designed to control the position and/or orientation of its end-effector within the system's workspace by use of actuated cables. CDPRs provide several benefits over traditional rigid-leg serial and rigid-leg parallel manipulators in the study of crop phenotyping. CDPRs offer minimal interference with the crops compared to rigid-support systems. Traditional serial or parallel manipulators interfere with plant growth because they are composed of large supports and machinery, which reflect and obstruct light and air flow. In addition, CDPRs are generally lighter and, therefore, capable of greater accelerations while maintaining high energy efficiency compared to rigid-linkage robots [26]. However, CDPRs have several design challenges. Cables can only perform while in tension, which puts limitations on end-effector position and greatly influences positional accuracy and system vibrations [27], [28].

CDPRs can be broken into three basic categories based on the number of cables and the mobility of the system: fully constrained, under constrained, and over constrained. A fully constrained parallel robot requires at least one more cable than the degrees of freedom of the end effector. In the case of three-dimensional translational motion, as is the focus of this paper, a fully constrained system requires four cables for full control of

position. The number of cables can be reduced if a constant external force, such as gravity, is applied to the end-effector. This force acts as an additional cable on the end-effector, reducing the number of physical cables needed to fully constrain the system [26].

This paper focuses on the suspended four-cable parallel robot. In these systems, the end-effector is supported by four cables with gravity delivering a downward force on the end-effector, behaving as a fifth cable. The four-cable configuration is beneficial over three-cable systems as the same system footprint has an expanded available workspace, and the cable load is reduced by distributing the load to an additional cable. However, using four cables creates a redundancy in the support system and complicates the system modeling and control as no unique cable configuration exists for an arbitrary location in the workspace [26].

Further modeling and design considerations come from the scale of the CDPR. In many CDPRs, cables can be assumed to have negligible mass, greatly simplifying system modeling and control. However, in the case of large-scale systems, cable weight can induce catenary sag in the cables, which strongly influences positional accuracy as well as system dynamics and vibration.

Significant work has been accomplished in the area of CDPRs, including kinematic design [26], [27], [29], [30] and dynamic analysis [28], [31]–[34]. Additionally, a large amount of research has been conducted in the area of cable mechanics[33], [35]–[37]. However, limited research exists in the field of large-scale suspended CPDRs where cable sag can play a major role in system dynamics and control. One of the few examples

of research into the area of cable sag in cable-driven manipulators is the FAST telescope, a newly constructed five hundred meter CDPR in China [22].

Substantial research has been performed by the FAST project on vibrations and stabilization of large scale CDPRs. However, the high speed requirements of the phenotyping system and the proportionally lower weight end-effector and cables result in significantly different system requirements and dynamics for a phenotyping system with four cables. One objective of this research is to develop a CDPR design and control scheme that can autonomously and rapidly move between crop plots. This system must be functional during harsh weather conditions, pass through the crop canopy with minimal crop interference, and provide stability for the phenotyping sensors mounted on the end-effector. The purpose of this chapter is to present a static model of the system as a first step to aid future system design optimization and dynamic modeling of a CDPR for crop phenotyping. In addition, a scaled-down system is built to gather experimental results and confirm the validity of the developed theoretical models.

2.2 Derivation

This section focuses on computing the inverse kinematics for a CDPR to be later verified experimentally. The solution begins with an analysis of a single cable to obtain the cable profile and tension. This solution then determines the force equilibrium equations for the four-cable system supporting a point-mass end-effector. The resulting force vectors are then applied to the end-effector model using the moment equilibrium equations to determine the orientation of the end-effector. In order to simplify calculations, cables are

assumed to be inextensible due to low tension values predicted in the cables compared to their elastic modulus and the predicted dominance of cable sag on cable flexibility[36].

Until construction of the full-scale system was complete, drive and control systems tests had to be performed using a scaled system. Vibrations and stability of the scaled system are not thoroughly investigated due to scaling incompatibilities between the test platform and the full-scale system. Because of the difficulties associated with scaling cable properties, the dynamic experimentation is assumed to not scale to the full-scale system. As such, controls tests and system properties including system stiffness and vibration predictions are beyond the scope of this work and not discussed.

In flexible cables with significant, evenly distributed mass, the weight of the cable provides varying vertical load along the length of the cable, which generates a curve as defined by (2-1) and is illustrated in Figure 2-1 [38].

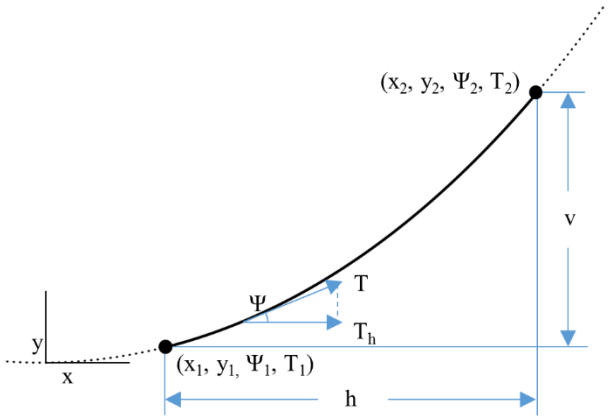

Figure 2-1. Sagging cable catenary parameters.

$$y = A * \cosh\left(\frac{x}{A}\right) \tag{2-1}$$

Here, A is the relationship between the constant horizontal tension seen in the cable, T_h, and the linear weight density of the cable, w.

$$A = \frac{T_h}{w} \tag{2-2}$$

Cable length, S, can then be calculated based on the arc length formula, integrating from cable end points, (x_1, y_1) and (x_2, y_2).

$$S = \int_{x_1}^{x_2} \sqrt{1 + \left(\frac{dy}{dx}\right)^2}\, dx = A * \sinh\left(\frac{x_2}{A}\right) - A * \sinh\left(\frac{x_1}{A}\right) \tag{2-3}$$

The angle between the cable and x-axis at any point along the cable, Ψ can also be solved geometrically using (2-4). Combining this angle with angle θ_n in Figure 2-2, the orientation of the cable with respect to ground (X, Y, Z) can be defined. Here, X and Y define the horizontal plane of the workspace while Z defines the elevation of the end-effector.

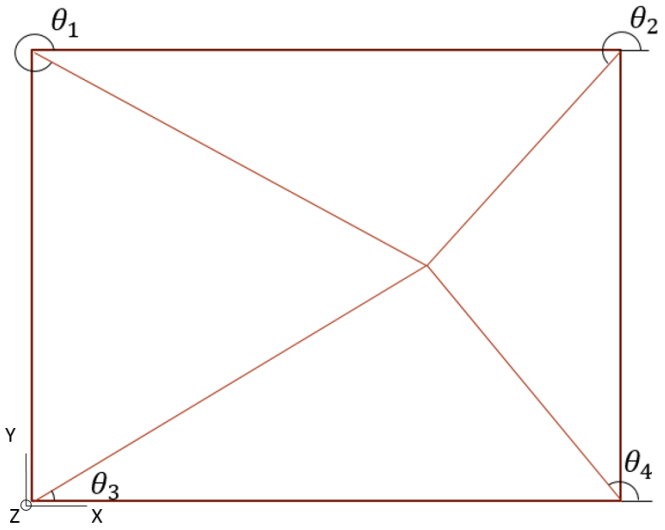

Figure 2-2. Top-down view of cable orientation.

$$\tan(\Psi) = \frac{dy}{dx} = \sinh\left(\frac{x}{A}\right) \tag{2-4}$$

A cable can only experience axial load; as a result, the force applied on the end-effector by the cable, T_1, must be in line with the cable. Knowing angle θ_n and Ψ_1 for cable n determines the direction of the force T_1 for cable n. Examining the forces along the cable, the only horizontal forces are located at the end points of the cable. Additionally, the only force acting along the length of the cable is gravity. Therefore, the horizontal tension component, T_h, is constant along the length of the cable. Cable tension can then be determined for any point along the cable:

$$T = T_h \sec(\Psi) \tag{2-5}$$

Solving (2-4) for Ψ, and substituting into (2-5),

$$T = T_h * \cosh\left(\frac{x}{A}\right) = A * w * \cosh\left(\frac{x}{A}\right) \tag{2-6}$$

For any given point in the field, the horizontal and vertical distances between the end-effector and the cable anchor point, h and v respectively, are known.

$$h = x_2 - x_1 \tag{2-7}$$

$$v = y_2 - y_1 = A * \cosh\left(\frac{x_1+h}{A}\right) - A * \cosh\left(\frac{x_1}{A}\right) \tag{2-8}$$

Reducing the system of equations produces three equations with four unknowns, A, S, T_1, and x_1.

$$v = A * \cosh\left(\frac{x_1+h}{A}\right) - A * \cosh\left(\frac{x_1}{A}\right) \tag{2-9}$$

$$S = A * \sinh\left(\frac{x_1+h}{A}\right) - A * \sinh\left(\frac{x_1}{A}\right) \tag{2-10}$$

$$T_1 = A * w * \cosh\left(\frac{x_1}{A}\right) \tag{2-11}$$

Solving the inverse kinematics for CDPRs involves solving static equilibrium equations of the system. In the four-cable CDPR with a point-mass end-effector, there are three translational degrees of freedom. The system is therefore defined by the equations for static equilibrium,

$$\sum \underline{F} = 0 = \sum_{i=1}^{4} \left(T_i * \underline{R_i} \right) + \underline{W} \tag{2-12}$$

where T_i is the tension value of the i^{th} cable, $\underline{R_i}$ is the unit vector in the direction of force $\underline{T_i}$, and $\underline{W}$ is the weight vector of the end-effector.

As indicated previously, each cable is defined by a system of three equations (2-9) – (2-11) that, given the current known geometric variables, depend on four unknowns (x_1, A, S, and T). In the three-cable CDPR, adding the equations for three cables to the three static equilibrium equations (2-12) produces a balanced system of equations that can be solved. Except in special circumstances, numerical methods must be used to solve the system as no explicit solution exists for this system of equations.

In the four-cable CDPR, there is one more unknown value than equilibrium equations available. The use of four cables in a three degree-of-freedom CDPR results in a redundant cable which generally suggests no unique solution exists for any given point in the system workspace. To solve this system of equations, a constrained optimization condition must be included with the problem. In this study, it was chosen to optimize the distribution of load on the cables by increasing the load on the lowest tension cable until the ratio between the highest and lowest tension is minimized. To achieve this, the model initially selects the position in the workspace to be considered. The length of the cable

anchored the furthest away from the end-effector is then set to a predefined percentage greater than the straight-line distance between the anchor point and the end-effector. Knowing the length of a cable as well as the locations of the cable endpoints with respect to each other fully defines the cable. With one cable fully defined, the system of equations and unknowns become balanced and can be solved iteratively. By progressively shortening the length on the predefined cable, the cable's tension increases as it becomes tauter. By increasing the tension on the prescribed cable, its tension gradually approaches that of the next lowest cable tension, more evenly distributing load between the cables until the system is considered optimized, and the resulting tensions, cable lengths, and cable profile are recorded. This is the optimization procedure used for this model. Multiple others are possible. For example, the simulation could attempt to optimize the angle of the cables to ensure that they provide the optimal rigidity for the system.

Thus far, the system end-effector has been assumed to be a point-mass. However, a potentially important parameter of CDPR design is the predicted orientation of the end-effector in different regions of the workspace. In the phenotyping system, end-effector orientation impacts the use of sensors intended to be downward facing as well as the range of motion of the end-effector gimbal.

Orientation is predicted by utilizing the force equilibrium results, applying them to a rigid body end-effector, and solving moment equilibrium equations,

$$\sum \underline{M} = 0 = \sum_{i=1}^{4} \underline{R_i} \times \underline{F_i} \tag{2-13}$$

where $\underline{F_i}$ is the force vector generated by the tension in the i^{th} cable and $\underline{R_i}$ is the position vector from the center-of-mass of the end-effector to the attachment point of the i^{th} cable. $\underline{R_i}$ is obtained by taking the position vector of the cable attachment point according to the end-effector frame of reference, $\underline{R_i}^*$, and passing it through three rotation matrixes representing the rotation about the system x, y, and z axis.

$$[R]_x = \begin{bmatrix} 1 & 0 & 0 \\ 0 & \cos(\alpha) & -\sin(\alpha) \\ 0 & \sin(\alpha) & \cos(\alpha) \end{bmatrix} \tag{2-14}$$

$$[R]_y = \begin{bmatrix} \cos(\beta) & 0 & \sin(\beta) \\ 0 & 1 & 0 \\ -\sin(\beta) & 0 & \cos(\beta) \end{bmatrix} \tag{2-15}$$

$$[R]_z = \begin{bmatrix} \cos(\gamma) & -\sin(\gamma) & 0 \\ 0 & \sin(\gamma) & \cos(\gamma) \\ 0 & 0 & 1 \end{bmatrix} \tag{2-16}$$

$$R_i = [R]_{z''} * [R]_{y'} * [R]_x * R_i^* \tag{2-17}$$

The three moment equilibrium equations can be solved numerically for the three angles. With an orientation of the end-effector predicted, the force equilibrium[1] and moment equilibrium equations can be iteratively solved until the orientation prediction converges.

The outputs of this model can be used to predict tension along the cables, cable lengths, cable profiles, and end-effector orientation. To accelerate simulation, it is assumed that system behavior is symmetrical across the geometric symmetry planes of the system.

[1] After the first iteration of solving the force and moment equilibrium equations is performed, the end-effector is changed from a point-mass to a rigid body, oriented based on the prediction created by the results of the first iteration of moment equations.

Thus, the same tension values are predicted in each quadrant of the field, but are associated with the mirrored cables.

Based on this assumption, cable tensions are solved across one quadrant of the workspace, and the behavior of the system in all other quadrants is then extrapolated based on the symmetry of the workspace. Figure 2-3 displays tension for a single cable as a function of end-effector position in the field at a fixed height. [2] Figure 2-3 also illustrates the amount that the end-effector is predicted to tilt as a function of end-effector position in the field at a fixed height.

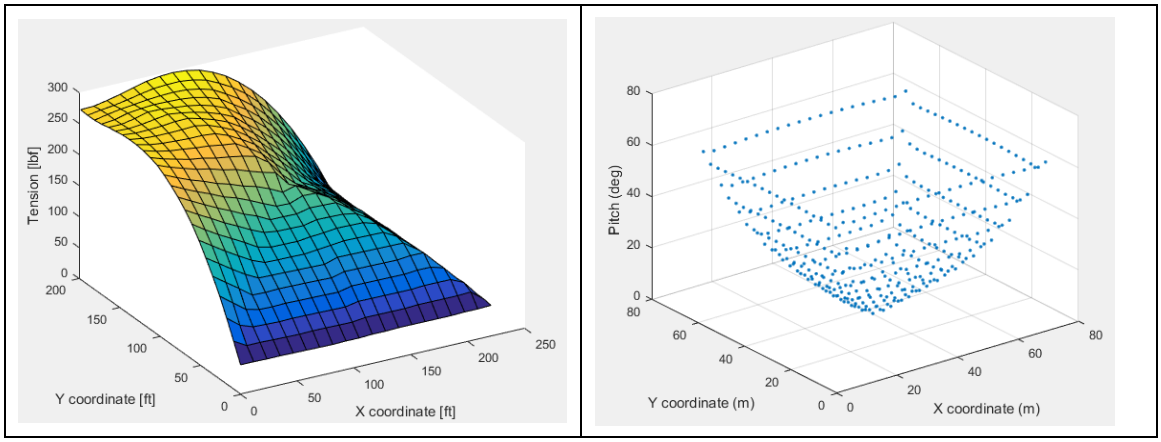

Figure 2-3. Model mesh outputs. (left) Theoretical cable tension. (right) Theoretical end-effector pitch.

2.3 Simulation

This static model was implemented using a MATLAB script (see Appendix A). The script was designed to output static cable tensions and dimensions based on the end-effector's location in the workspace. To evaluate the system and generate figures, such as

[2] Data given for 68 kg end-effector, 3m above ground.

in Figure 2-3, this function was inserted into a parent function that would generate a mesh of points throughout the workspace and iteratively call the modeling function for every node. These data were then automatically compiled and exported to an Excel file for later analysis. The last step of the parent file was to create surface plots as in Figure 2-3.

Several hundred separate simulations were generated, varying every parameter, from tower locations and height, to cable and end-effector weight and size. Simulations were run on CPDRs the size of the system being constructed for the university down to the size of a desktop system. These simulations were all collected and analyzed to achieve a better understanding of how certain parameters affect static behavior and to develop the ideal system configuration.

2.4 System Dimensional Optimization

Modeling CDPRs requires knowledge of seven key system parameters (Figure 2-4):

- Field width, W_F
- Field depth, D_F
- End-effector mass, M
- Cable density, ρ
- Width between cable feed points, W_P
- Depth between cable feed points, D_P
- Height of cable feed points, H

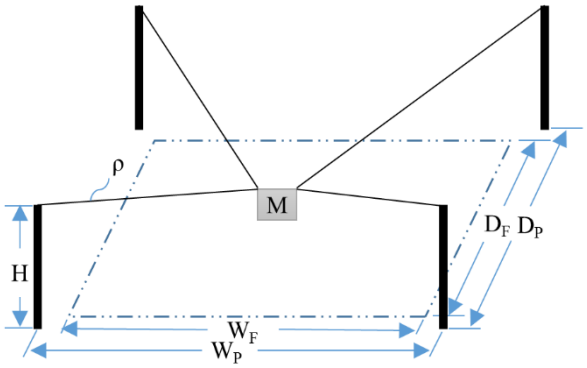

Figure 2-4. System parameters of a four-cable CDPR system.

Field dimensions and end-effector operational height were predetermined by the design of the phenotyping facility and are presented in Table 2-1. During system design, it was chosen to use a custom Kevlar cable with a fiber optic core for sensor data transmission. Use of the selected cable defines the cable density and adds an additional constraint by limiting tension in the cables.

Table 2-1 CDPR full-scale system parameters.

Defined parameters		Variable parameters	
Field width	67 m	End-effector mass	45-90 kg
Field depth	60 m	Tower footprint width	75-100 m
Maximum end-effector height	10 m	Tower height	15-26 m
Cable density	10 g/m		
Tower aspect ratio	10:9		
Maximum tension	1500 N		

The primary objective of this analysis is to determine the most appropriate location for the towers supporting the cable system and to determine the maximum required height for the cable-feed pulleys. The end-effector design is currently incomplete; therefore, studies investigating multiple end-effector weights are analyzed alongside of tower layout and height.

To optimize tower location and height as well as end-effector weight, three measurements must be analyzed:

- Maximum cable tension in consideration of cable strength
- Tension distribution in consideration of system stabilization
- End-effector orientation in consideration of end-effector reorientation capabilities

Many simulations were generated with different permutations of tower height, tower distancing, and end-effector mass. Selected results from these simulations are presented in Figures 2-5 and 2-6. Figure 2-5 shows the influence of all three variables on the predicted maximum tensions for the system within the operational workspace.

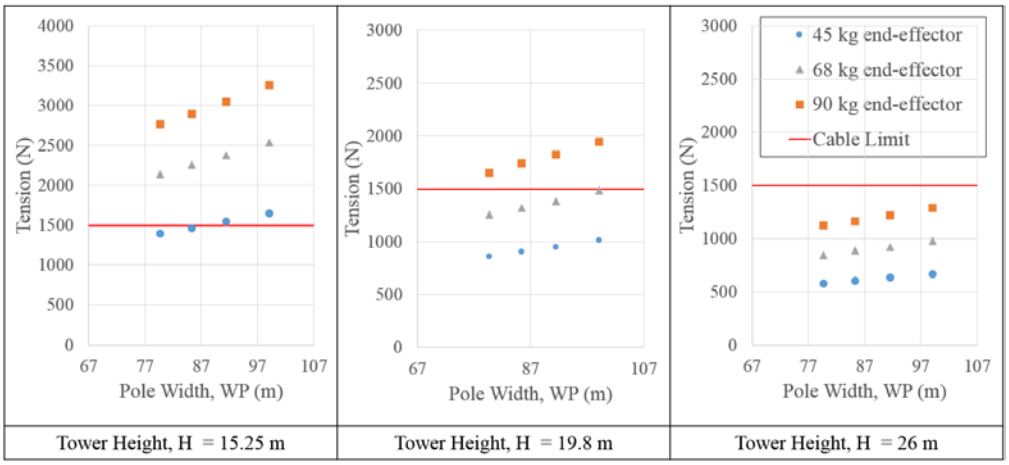

Figure 2-5. Theoretical maximum tension in field.

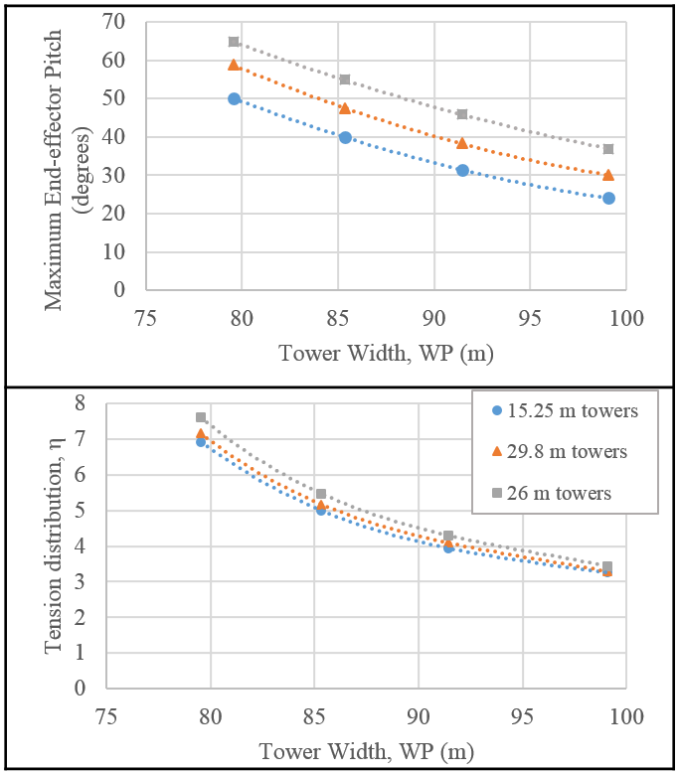

Figure 2-6. Dimensional considerations. (top) Theoretical end-effector pitch. (bottom) Theoretical tension distribution.

The even distribution of load between cables has a substantial impact on cable control and system vibrations [27]. The distribution of load between the cables can be parameterized by the variable η as follows:

$$\eta_{xyz} = \frac{T_{max}(x,y,z)}{T_{min}(x,y,z)} \tag{2-18}$$

Where T_{max} and T_{min} are the highest and lowest cable tensions, respectively, for the given orientation. η_{max} is then the highest predicted η_{xyz} in the workspace for the given system configuration. Load distribution, and therefore cable performance, is expected to improve as η_{max} approaches one. Figure 2-6 shows the impact of tower location and height on η_{max}.[3]

As the end-effector moves radially from the center of the workspace, the uneven distribution of load on the cables causes the vertical axis of the end-effector to pitch towards the center of the field, away from the vertical axis of the workspace. This behavior can be parameterized by measuring the angle between the vertical axis of the end-effector and the vertical axis of the workspace. For a gimbaled end-effector, which is what is being used in this analysis, the maximum predicted angle is required to determine the required range of motion of the gimbal. In an end-effector without a gimbal, extreme angles can limit the use of sensors and equipment that are required to maintain a certain

[3] End-effector weight was found to have no impact on η_{max}.

orientation. Figure 2-6 shows the impact of tower location and height on the end-effector inclination angle.[4]

According to preliminary designs, the end-effector with the maximum weighted sensor package will be between 45 and 68 kg. Based on the data presented in Figure 2-5 and 2-6, the minimal system configuration that will safely support a 68 kg end-effector utilizes 19.8 m (65 ft) towers. A tower shorter than this would require placement too close to the workspace, and cable performance would likely cause the system to be uncontrollable. Taller towers reduce the load on the cables, which allow the towers to be placed further from the workspace, improving cable performance and reducing end-effector pitch. However, this introduces further design challenges. Moving the towers outwards expands the space requirements of the system by adding a large perimeter of empty space between the workspace and towers. Also, taller towers are more expensive and require larger footings for support.

With 19.8 m towers selected, the maximum allowable width between towers for the specified end-effector weight and cable strength is 99 m (325 ft). Positioning the towers this far from the workspace increases system footprint by 53% and generates an 18% increase in maximum tension compared to a system with similar towers placed 80 m apart. However, it also reduces η and end-effector inclination by 54% and 49% respectively, enhancing system performance. Positioning the towers any further out,

[4] End-effector weight was found to have no impact on end-effector inclination angle.

however, increases cable tension, reducing the safety factor for the cables. The final recommended configuration for this system is outlined in Table 2-2.

Table 2-2 Optimized system dimensions.

Parameter	Optimized dimension
Tower distance	99 x 89 m (325 x 293 ft)
Tower height	19.8 m (65 ft)
End-effector mass limit	68 kg (150 lb)

CHAPTER 3. CABLE-DRIVEN ROBOT CONTROL THEORY

A small-scale CDPR was built to perform experiments to aid in the design of the cable system and end-effector before the full-scale system was available. To conduct these experiments, a control system had to be designed to maneuver the end-effector through the workspace. The control theory developed in this chapter has applications for general four-cable CDPRs.

3.1 Background

Without the full-scale system in Mead constructed, multiple small-scale systems were designed and constructed. These systems were used to perform scaled experiments and to make general observations of CDPR behavior, beginning with a 2ft x 2ft, desktop model and eventually moving up to a 27ft x 24ft model, approximately one twelfth the size of the full-scale system. To allow for simple scalability, the system was modularized, using a separate microcontroller and power supply for each winch, all communicating wirelessly with one controlling microcontroller that may interface with a computer for automated input. For further design details see Appendix F.

The winches went through several iterations. In the desktop model and the first 12^{th} scale system, stepper motors were used to actuate 3d-printed drums (Figure 3-1). By the final design – see Appendix F for design files – the motors were replaced with DC brushed motors with encoders to remove cable-feed tracking errors caused by misstepping in the original motors. Each motor is controlled using an Arduino Pro Mini that communicates with the system controller using nRF24l01+ modules. The winches use a spring-applied tension rod, used to keep the cable tightly wound around the drum. Each winch has three

user inputs. The first is a reset button while the other two are switches used to set an address for the winch's communications so that the controller can identify the locations of the winches.

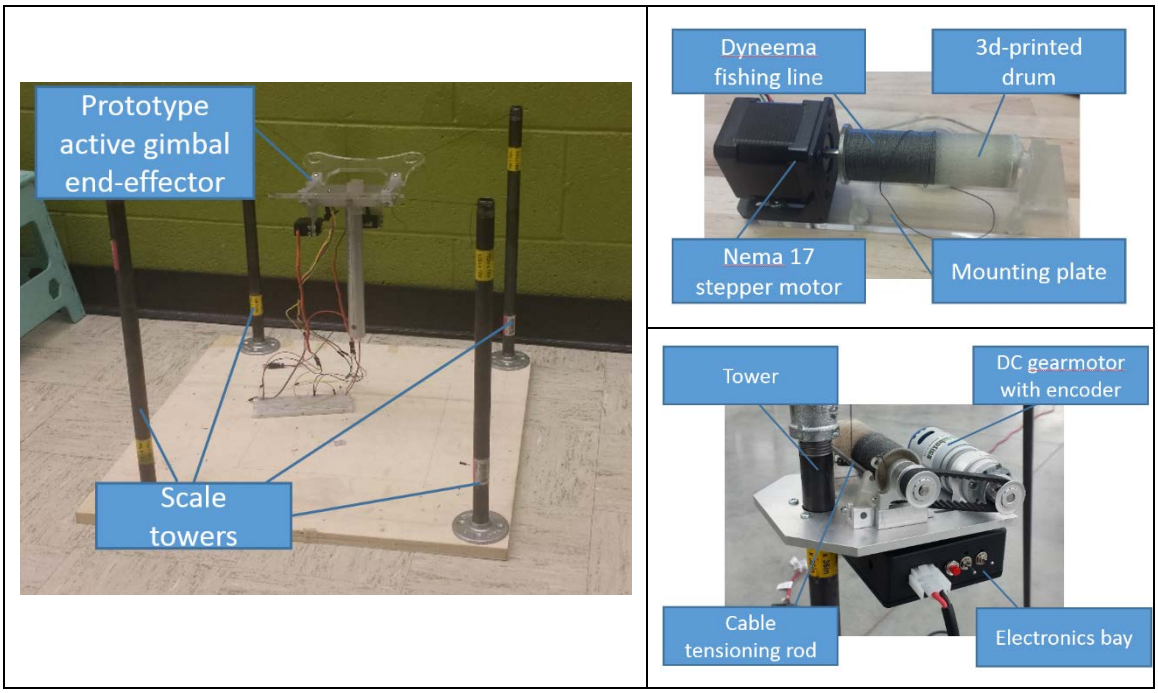

Figure 3-1. CDPR model components. (left) Desktop prototype. (right-top) Initial winch design using stepper motor. (right-bottom) Current CPDR winch, using DC gearmotor and encoder.

The controller was built around an Arduino Mega 2560 in a laser-cut, acrylic case (Figure 3-2). The inputs include two joysticks, primarily used to define the desired motion of the end-effector, and a few switches used to control system settings. The system also includes several LEDs, one red LED to indicate power, one yellow LED to indicate successful communication with the end-effector, and four green LEDs to indicate successful communication with the winches. While capable of controlling the system on its own, the controller is also capable of interfacing with a computer so that a user can input coordinates to navigate the system towards.

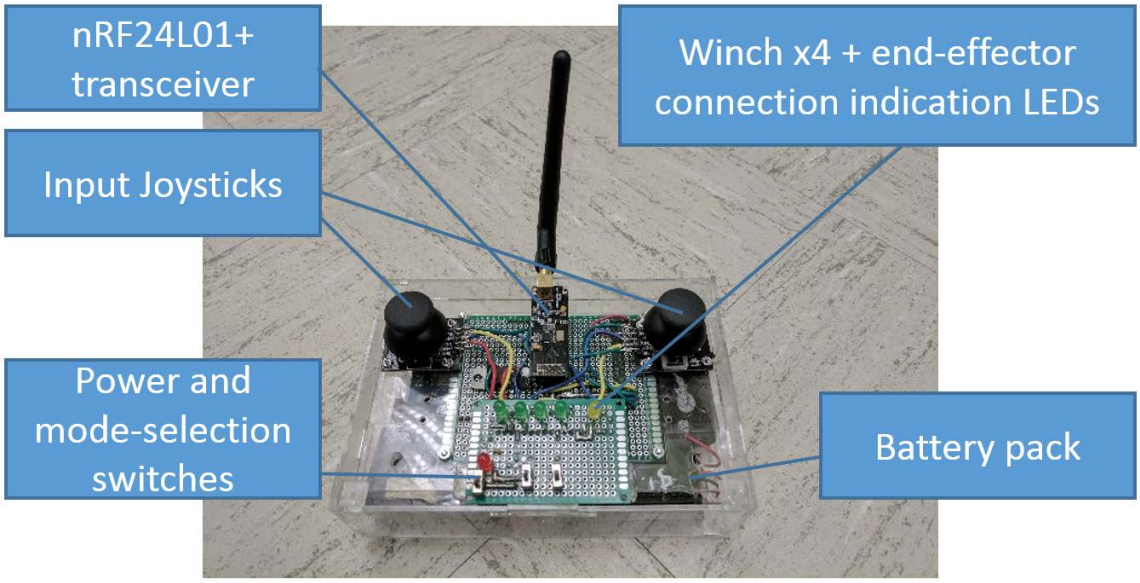

Figure 3-2. CDPR controller prototype.

3.2 Implementation

The basic CDPR control scheme is illustrated in Figure 3-3 and operates as follows. The controller receives an input from one of two sources: it receives a destination in the workspace to move the end-effector to from a PC connected to the Arduino's USB port, or it receives a desired velocity vector for the end-effector from the two on-board joysticks. The controller processes this data and determines how fast each winch is required to move in order to guide the end-effector along the target path. This speed is then transmitted to the winches, which return messages containing the length of their respective cable to allow the controller to approximate the end-effector's current position.

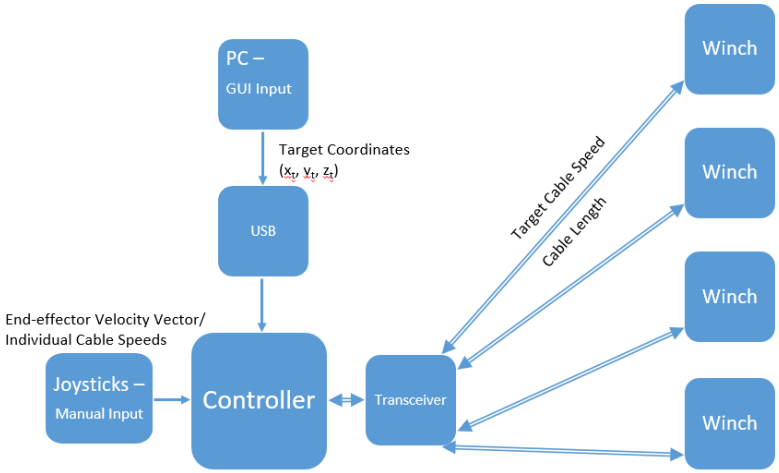

Figure 3-3. CDPR control scheme.

The CDPR control system designed operates in three basic modes:

- Manual Winch Control
- Manual Navigation
- PC Navigation

The default state for the system is Manual Navigation, while Manual Winch Control and PC Navigation must be triggered. Based on the state of the system, different commands may be transmitted from the controller to the winches. The general communication message is formatted as follows:

$$\{\langle A-D\rangle\langle\$\rangle\langle\#\#\#\rangle\langle:\rangle\}$$

Where ‘A-D’ is an identifying character indicating which of the four winches the message is meant for, ‘$’ represents the given command character/string (Table 3-1), indicating how the target winch is to respond to the input, ‘###’ represents any data that

are a part of the command (ex: target velocity), and ‘:’ is the terminating character to indicate the end of the transmission. For example, to command the winch in the bottom-left corner of the workspace to feed cable at a rate of 0.5 in/sec, the controller would transmit the following command: <CV050A:>. To command the winch in the top-right corner of the workspace to retract cable at a rate of 2.48 in/sec, the controller would transmit the following command: <BV248B:>.

Table 3-1 CDPR communication commands.

Message	Direction	Purpose
V	Controller-to-Winch	Receive cable velocity
D	Controller-to-Winch	Modify damping constant
L	Controller-to-Winch	Reset cable lengths
P	Winch-to-Controller	Return cable length
SETUP	Controller-to-Winch	Initialize winch
PAIRED	Winch-to-Controller	Confirm successful connection
STOP	Controller-to-Winch	Emergency, immediate stop

3.2a Manual Winch Control

In Manual Winch Control mode, the two joysticks are used to individually control the four cable actuation winches. The x and y-axis (or horizontal and vertical) signals from the left joystick correlate to the line-speed of cables one and two, respectively, while the

x and y-axis signals form the right joystick correlate to the line-speed of cables three and four (Figure 3-4). In this mode, the controller simply reads the four analog inputs from the joysticks, maps them to desired speeds for the winches, and transmits the speed to the appropriate winch. This mode is primarily used for fine-tuning cable lengths during initial setup or in the case that one cable becomes slack.

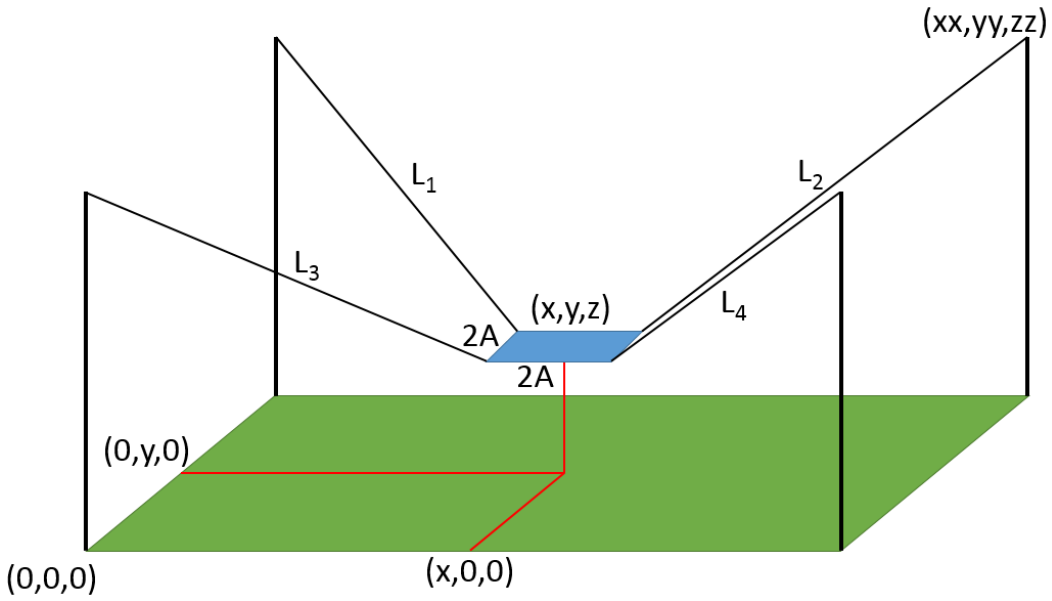

Figure 3-4. Control system dimensional layout.

3.2b Manual Navigation

In Manual Navigation mode, the two joysticks are used to define the desired velocity vector for the end-effector. The left joystick is used to define the horizontal vector components, x and y, while the right joystick is used to define the vertical vector component, z. Based on the target vector and the current position of the end-effector, individual cable speeds are calculated (see Chapter 3.3 Derivation below) and transmitted to the respective winches. Due to latency and other errors, the end-effector shows a

tendency to rise or lower as it moves radially from the center of the workspace. No feedback is used in this mode to maintain a straight flightpath.

Due to the lack of catenary sag in the cables used in the experimental setup, straight-line approximations are made to determine the distances between the base of the cables at the towers and the end-effector. This simplifies the navigational model, allowing for real-time control. However, as previously discussed, only three cables are required to define the position of a point in the workspace. The fourth cable (the cable with the lowest tension and therefore lowest rigidity) affects the distribution of load between the cables and, in essence, only tags along for the ride. As a result of the lack of sag in the cables, small errors in cable control can cause the fourth cable to shorten, increasing its tension and causing it to replace one of the other cables as a driving cable. As a result, trying to maintain all four cables at near-even tensions can cause the support system to fluctuate between different cables, inducing vibrations into the end-effector. This is most evident as the end-effector approaches the corners, where the longest cable is experiencing tensions far less than the other three cables.

To overcome this, one cable is chosen to remain a given length longer than the straight-line distance between its tower and the end-effector. As a result, the other three cables remain consistently in control of the system and this disturbance is avoided. Which cable is chosen as the slack cable is determined by the location of the end-effector in the field. The field is divided into four quadrants. Whichever cable is located in the same quadrant as the end-effector is considered the primary cable, as it experiences the highest tension

and is most critical in defining the end-effector position. The diagonal cable, as it is the longest and experiences the lowest tension, is treated as the slack cable.

The issue in this method occurs when the end-effector passes from one quadrant to another or when it approaches the center of the workspace. As the method stands, when the end-effector passes from one quadrant to another, the previously slack cable shortens while the newly slack cable extends. This can cause a momentary disturbance for the end-effector. To prevent this, the slack in the cable is a function of the distance from the x and y axis midlines of the workspace.

$$\Delta L = C * \sqrt{\Delta x^2 + \Delta y^2 + \Delta z^2} \tag{3-1}$$

where ΔL is the length added to the base length of the slack cable, Δx and Δy are the distances from the respective midlines, Δz is the distance from the base of each cable (the top of the towers), and C is a proportionality constant. Δz is included because tension increases as Δz decreases. As a result, the three supporting cables stretch, removing what little sag exists in this experimental system, and the fourth cable shortens to match.

While the remaining three cable speeds are determined based on a target velocity vector of the end-effector, the slack cable's speed is set proportional to the error between the current length and the desired length of the cable. As a result of this methodology, as the end-effector approaches either midline, the tension difference between the two cables on the opposite side of the field approaches zero, and the end-effector becomes driven by all four cables. As the end-effector approaches the center of the workspace, $\Delta L \rightarrow K * \Delta z$. When properly calibrated this additional length approximates the error in the straight-line

approximation of the cable length, causing the slack cable to approach the same tension as the other three cables.

3.2c PC Navigation

Controlling the end-effector using PC input is the same as with manual navigation, except for the derivation of the end-effector velocity vector. When the controller is interfaced with a computer via the serial port, the user may enter a set of coordinates to send the end-effector towards. When this input is received, the controller records the current position as $\underline{P_0}$ and the input coordinates as $\underline{P_{target}}$. Based on these two points, a base velocity vector $\underline{V_0}$ is calculated using (3-2), as illustrated in Figure 3-5.

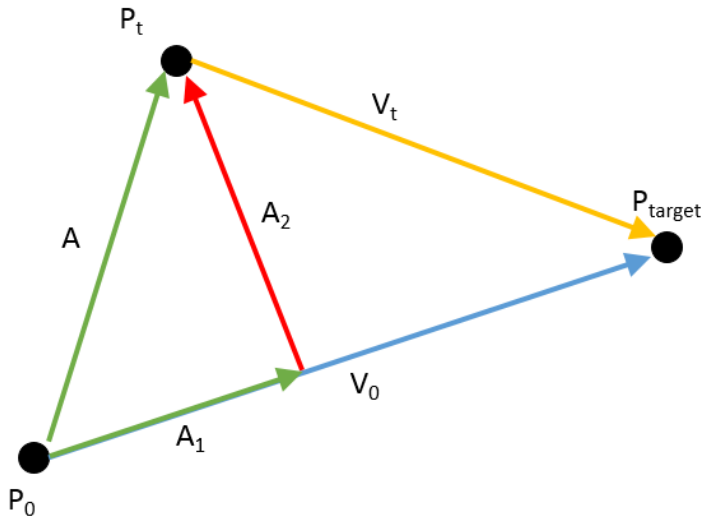

Figure 3-5. End-effector velocity vector compensation.

$$\underline{V_0} = C * \frac{\underline{P_{target}} - \underline{P_0}}{\left|\underline{P_{target}} - \underline{P_0}\right|} \tag{3-2}$$

As stated in *Manual Navigation*, when the controller is given a straight line to follow, as with $\underline{V_0}$, the end-effector tends to deviate from the path. This deviation can be corrected by updating the velocity vector to use the position at time *t*.

$$\underline{V_t} = C * \frac{\underline{P_{target}} - \underline{P_t}}{\left|\underline{P_{target}} - \underline{P_t}\right|} \tag{3-3}$$

While this will cause the end-effector to approach the target, the path becomes an arc. Depending on the initial and final positions, this arc can cause the end-effector to either lower into the crops below or rise above the operating height of the system, risking damage to the cables or winches. To minimize this arc, a correction vector is add to $\underline{V_t}$ to drive the end-effector back towards its original trajectory.

This is done by projecting the vector between points $\underline{P_0}$ and $\underline{P_t}$, vector $\underline{A}$, upon vector $\underline{V_0}$ to create the axial and radial vectors, $\underline{A_1}$ and $\underline{A_2}$, respectively.

$$\underline{A_1} = \underline{A}\frac{\underline{V_0}}{\left|\underline{V_0}\right|} \tag{3-4}$$

$$\underline{A} = \underline{A_1} + \underline{A_2} \tag{3-5}$$

$$\underline{A_2} = \underline{A} - \frac{\underline{A}}{\left|\underline{V_0}\right|}\underline{V_0} = \underline{A} - \frac{\underline{A}\cdot\underline{V_0}}{\underline{V_0}\cdot\underline{V_0}}\underline{V_0} \tag{3-6}$$

Taking $\underline{A_2}$ as the error that must be removed, a correction vector may be calculated as a vector $\underline{A_2}$ times gain *C*. substituting (3-2) and (3-3) gives an error vector that may be added to the original vector for point *t*.

$$\underline{V_{err}} = C * \left(\underline{P_t} - \underline{P_0} - \frac{\left(\underline{P_t} - \underline{P_0}\right) \cdot \left(\underline{P_{target}} - \underline{P_0}\right)}{\left(\underline{P_{target}} - \underline{P_0}\right) \cdot \left(\underline{P_{target}} - \underline{P_0}\right)} * \left(\underline{P_{target}} - \underline{P_0}\right) \right) \tag{3-7}$$

$$\underline{V} = \underline{V_t} + \underline{V_{err}} \tag{3-8}$$

Using this method, the end-effector was found to follow the straight-line vector much more closely (error imperceptible to the naked eye).

One other major sources of vibration seen with the system as it stands was jerk when beginning and ending navigation. To overcome this disturbance, velocity was set to ramp up when starting as a function of distance from the start point, and to ramp down when ending as a function of distance from the target.

$$V^* = \frac{K}{|V|} V \tag{3-9}$$

where:

$$K = \max(\min(C_1 * A, C_2 * V_t, V_{max}), V_{min}) \tag{3-10}$$

From here, cable speeds were calculated as described in *Manual Navigation* above.

3.3 Derivation

To track and navigate a CDPR system knowing only the cable lengths at any moment, one must be able convert between cable lengths and the Cartesian coordinate system. Assuming that the end-effector is always level, the length of each cable can be calculated in terms of the end-effector position (x,y,z) using the Pythagorean theorem and Figure 3-4.

$$L_1 = \sqrt{(x-A)^2 + (yy-y-A)^2 + (zz-z)^2} \tag{3-11}$$

$$L_2 = \sqrt{(xx-x-A)^2 + (yy-y-A)^2 + (zz-z)^2} \tag{3-12}$$

$$L_3 = \sqrt{(x-A)^2 + (yy-A)^2 + (zz-z)^2} \tag{3-13}$$

$$L_4 = \sqrt{(xx-x-A)^2 + (yy-A)^2 + (zz-z)^2} \tag{3-14}$$

Solving the first three equations for x, y, and z, gives:

$$x = \frac{-L_1^2+L_2^2-xx^2+2*A*xx}{4*A-2*xx} \tag{3-15}$$

$$y = \frac{L_1^2-L_3^2-yy^2+2*A*yy}{4*A-2*yy} \tag{3-16}$$

$$z = zz - \sqrt{L_3^2 - (x-A)^2 - (y-A)^2} \tag{3-17}$$

With this, a user can track the position of a suspended payload from three cables by tracking cable feed with encoders. In the previous sections it was stated that cables are actuated based on a desired speed of the end effector. By taking the derivatives of (3-15) – (3-17) with respect to time, equations of cable velocities can be created based on the velocity of the end-effector.

$$\frac{dL_n}{dt} = \frac{\partial L_n}{\partial x}\frac{dx}{dt} + \frac{\partial L_n}{\partial z}\frac{dy}{dt} + \frac{\partial L_n}{\partial z}\frac{dz}{dt} \tag{3-18}$$

$$\frac{dL_1}{dt} = \frac{(x-A)\dot{x}+(y-yy+A)\dot{y}+(z-zz)\dot{z}}{\sqrt{(x-A)^2+(y-yy+A)^2+(z-zz)^2}} \tag{3-19}$$

$$\frac{dL_2}{dt} = \frac{(x-xx+A)\dot{x}+(y-yy+A)\dot{y}+(z-zz)\dot{z}}{\sqrt{(x-xx+A)^2+(y-yy+A)^2+(z-zz)^2}} \tag{3-20}$$

$$\frac{dL_3}{dt} = \frac{(x-A)\dot{x}+(y-A)\dot{y}+(z-zz)\dot{z}}{\sqrt{(x-A)^2+(y-A)^2+(z-zz)^2}} \tag{3-21}$$

$$\frac{dL_4}{dt} = \frac{(x-xx+A)\dot{x}+(y-A)\dot{y}+(z-zz)\dot{z}}{\sqrt{(x-xx+A)^2+(y-A)^2+(z-zz)^2}} \quad (3\text{-}22)$$

The controller calculations therefore run as follows.

1. Use feedback from winch encoders to record current cable lengths
2. Using known cable lengths and (3-15) – (3-17), find the current position of the end-effector
3. Use (3-8) to solve the desired end-effector velocity vector
4. Using the desired end-effector velocity vector and (3-19) – (3-22), find the desired speed for each winch
5. Transmit the desired speed to each winch and receive the respective cable lengths in response
6. Repeat process

CHAPTER 4. SCALED SYSTEM DESIGN AND EXPERIMENTATION

A small-scale CDPR was constructed to aid in this research. Its uses included serving as a test bed for end-effector designs, developing CDPR control schemes, understanding cable system dynamics, and verifying static model results. Its development involved multiple iterations, ending with a twenty-foot wide system using mobile towers with individual power sources and wireless communications to allow the system to be easily scaled.

4.1 Design

A one-twelfth-scale model of the field phenotyping system, shown in Figure 4-1, was designed to confirm the simulator results presented in Chapter 2 and to test control system designs from Chapter 3 as well as system dynamics, and end-effector stabilization hardware and controls. Scaling factors are calculated using the Buckingham Pi theory following the procedures used by Yao, et al [27]. Dimensional parameters are listed in Table 4-1.

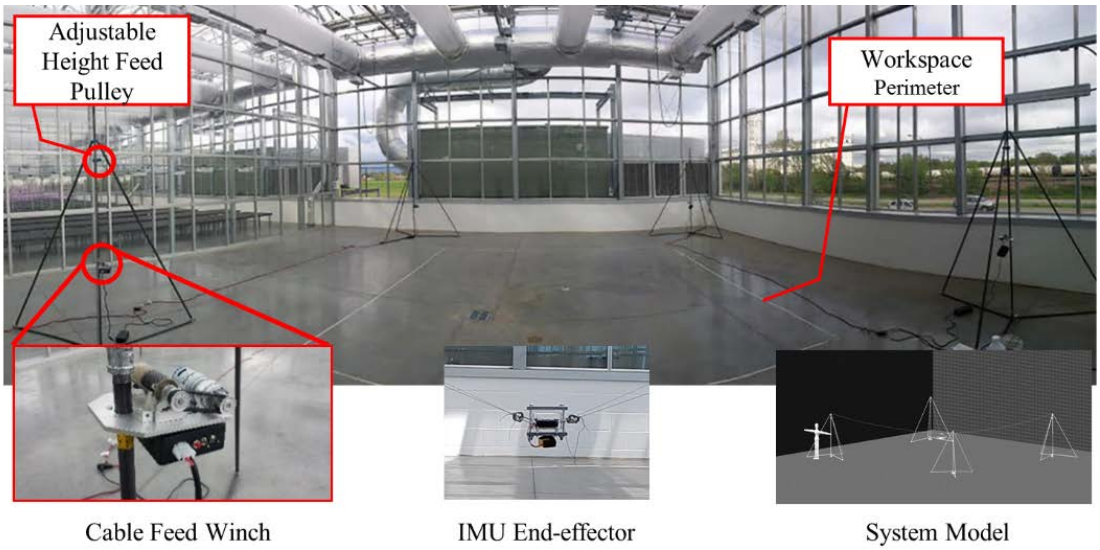

Figure 4-1. One-twelfth-scale system.

Table 4-1 One-twelfth-scale CDPR scaling parameters.

Parameter	Similarity scale	Full size dimension	Model dimension
Field width	1:12	67 m	5.60 m
Field depth	1:12	60.35 m	5.03 m
Tower height	1:12	25.91 m	2.16 m
Cable density	1:55*	10.8 g/m	0.197 g/m
End-effector mass	1:144	77 kg	0.535 kg

Covered in more depth by Yao, the scaling of the system primarily comes down to two scaling factors: a length scale and a density scale. For the system to remain similar, the dimensions defining the size of the workspace and the lengths of the cable must be the same scale. To remain similar, the density factor must remain the same as the length scale, meaning that for a one-twelfth scale system, the linear density of the cables must also be scaled by a factor of twelve. The end-effector, however, is subject to both scales. The end-effector, in theory, must be both one-twelfth the original size and the original density. However, instead of scaling both volume and density, the mass may be scaled by a factor of 144. The mass of the cable is also subject to this scaling factor, however, its

length has already been scaled by a factor of twelve by scaling the workspace. Therefore, its density is only required to be scaled by a factor of 12.

An appropriate cable was not utilized in the one-twelfth-scale system due to the challenges of scaling cable properties of density, construction, and stiffness. Dyneema fishing line with a diameter of 1 mm was instead used, resulting in a density scaling factor of 55 rather than 12. Due to this change, cable sag and stiffness are not similar between the one-twelfth-scale and full-scale systems. Thus, full-scale system dynamics cannot be predicated on one-twelfth-scale experimentation. As a result, the one-twelfth-scale system may be used in studying general CDPR behavior in the testing of stabilization and control systems; however, these results are not presented as a part of this work.

The one-twelfth-scale system was designed to test not only the determined optimal configuration from Chapter 2, but an array of system configurations. As such, towers used to support the cable system were designed as collapsible tripods to allow for easy alteration to tower layouts and system scales. Cable-feed pulleys with adjustable height were mounted on the towers to experiment with multiple cable system heights. Attached to the towers were custom winches to actuate cable feed. Each winch wirelessly communicated with the system navigational controller to drive the system with motor-mounted-encoder feedback to track cable length and approximate end-effector position.

An end-effector mounted with an inertial measurement unit (IMU) was created to measure end-effector orientation when navigated through the workspace. It was also used to observe the response to impulse disturbances on the end-effector as well as the impact

of end-effector acceleration during travel on system vibration. Additionally, a gimballed end-effector equipped with load cells at the cable connection points was used to perform experiments to measure cable tensions during travel as well as to confirm tension predictions from the simulator.

For further design details and drawings, refer to Appendix F.

4.2 Experimentation

While many experiments were conducted with the one-twelfth-scale system, three are included in this report. The first experiment was an analysis of the cable system's static behavior, including a record of cable tensions and end-effector orientation for various locations in the workspace. A static model of the CDPR was developed to aid in the design of the full-scale system. This model was used to predict system structural requirements as well as attempt to optimize the system layout. These experiments were required to verify the accuracy of the model.

The second set of experiments included in this analysis is the set of experiments used to determine the navigational stability and repeatability of the control system developed. In the beginning of this research, it was believed that the engineering team would be required to develop a control system for the CDPR. It was later determined that the Spidercam system would be used, including its control system. The custom control scheme had already been largely developed by the time this decision was made, however. It continued to be developed and used in the one-twelfth-scale system to aid in experimentation and dynamic analysis.

Rather than being individual experiments, the third section to follow is a set of observations made during all of the experiments conducted. They are observations of how the system was seen to respond to certain disturbances.

4.2a Static Analysis Confirmation

One task of the one-twelfth-scale system was to determine the accuracy of the mathematical model developed previously. Two primary criteria for confirming the validity of the simulator results were cable tension and end-effector orientation. Two tests were performed to determine the accuracy of the theoretical predictions. One test involved navigating the load-cell end-effector through a series of points (Figure 4-2). [5] At each point, average load cell readings were taken and were compared to theoretical values predicted by the simulator, as displayed in Figure 4-3.[6] The second test involved navigating the IMU end-effector through a series of points (Figure 4-2) to measure end-effector orientation, which, in turn, was compared to simulator results, as displayed in Figure 4-4. Due to the symmetry of the system, all tests are performed in one quadrant of the workspace, and the results are assumed to mirror across the symmetry planes.

---

[5] For tension testing, points are located at heights of 0.25m (lowest feasible elevation for given end-effector) and 1.14 m (maximum safe operating height for given weight).

[6] Rather than using a 0.535 kg end-effector for the tension tests, a 1.9 kg end-effector was used. This was done to increase cable tensions to a level more appropriate for the utilized load cells.

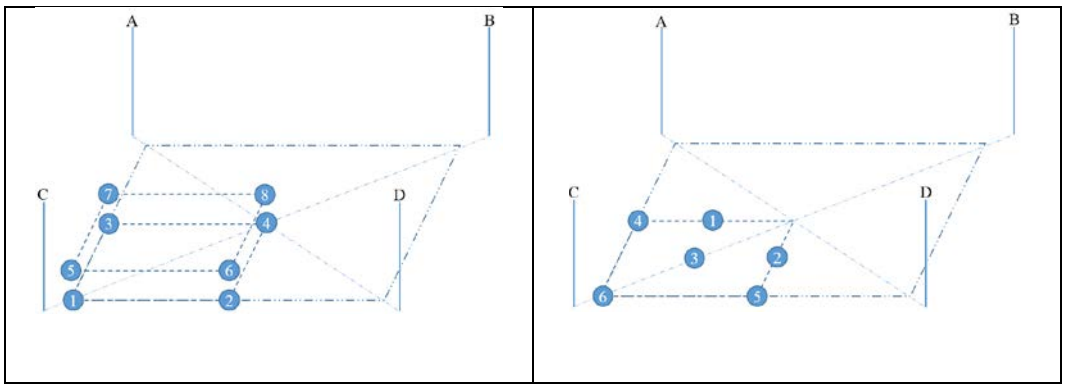

Figure 4-2. Experimental data points. (left) Tension experiment test locations. (right) Orientation experiment test locations.

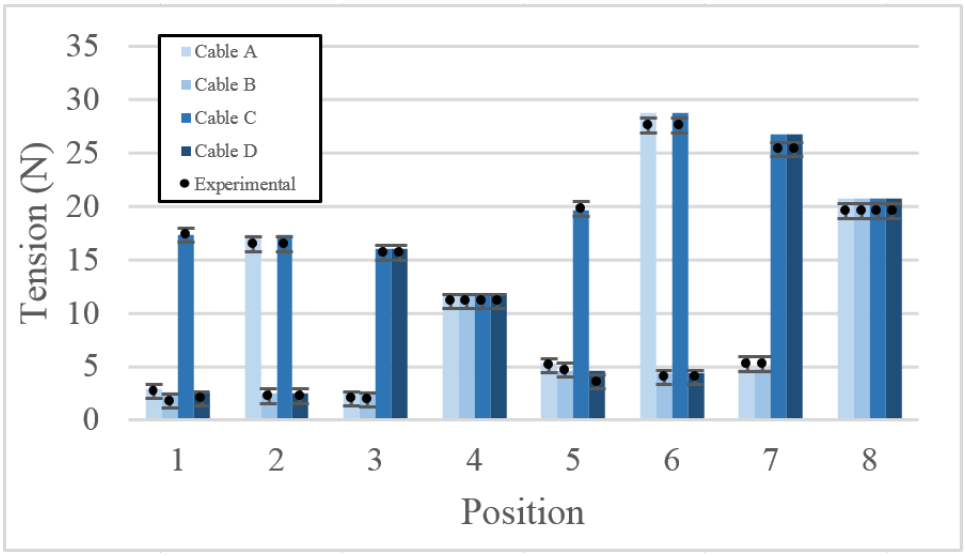

Figure 4-3. Theoretical vs. experimental cable tensions.[7]

[7] Bars represent theoretical values while points and error bars represent experimental averages and standard deviations, respectively.

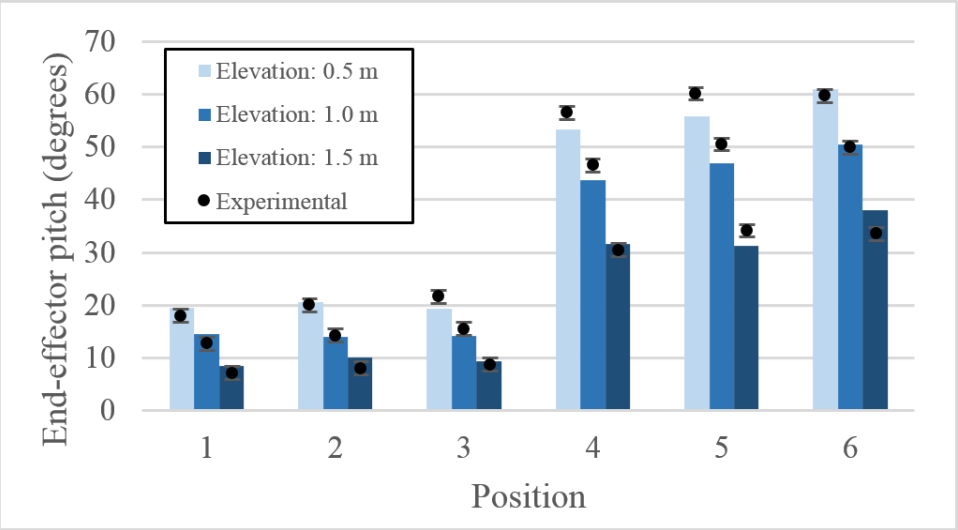

Figure 4-4. Theoretical vs. experimental values of the end-effector tilt angle. [8]

Results from the first test show that the simulator predicted cable tensions to within an error of 0.7 N with a standard deviation of 0.5 N for an end-effector of weight 18.35 N. Results from the second test were then shown to predict end-effector tilt to within 2.0 degrees with a standard deviation of 1.3 degrees. These results indicate that the designed simulator accurately predicts cable performance for the purpose of static analysis.

Based on these experiments, agreement between the simulator and physical model is adequate to justify the use of the simulator results in predicting the static behavior of the full-scale phenotyping system.

[8] Bars represent theoretical values while points and error bars represent experimental averages and standard deviations, respectively.

4.2b Control Theory Testing

To test the capabilities of the navigation system, a network of obstacles to maneuver were setup within the CDPR workspace. Using both manual/joystick input and automated/ GUI input, a dummy end-effector with a suspended plumb bob was maneuvered around the field, moving around obstacles and positioning the tip of the plumb bob directly above each obstacle, as in Figure 4-5. Data from these experiments are purely videographic and links to several videos are located in Appendix C.

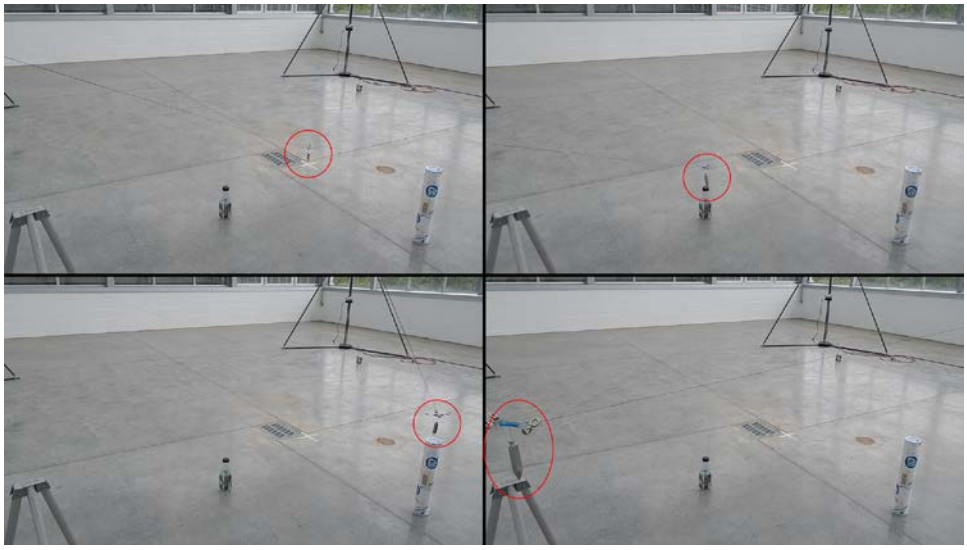

Figure 4-5. CDPR positioning experiment.

The experiments showed that the end-effector could move smoothly with joystick input. However, as previously stated, the end-effector would rise or fall as it moved towards or away from the center of the field. When using the automated control system, where destination coordinates would be inputted to the controller and the system would attempt to reach those coordinates, it was found that there were positional errors. The errors were primarily witnessed in the vertical axis. For example, the end-effector may stop an inch

short of the destination but four inches too high. This issue was inconsistent and believed to be due to multiple issues, including misalignment of the support towers, inaccuracies in winch-drum diameters, and elongation and sag of the cables. As stated, the control system assumes straight, inextensible cables. While the end-effector automated positioning system was not accurate, it was precise. During experimentation, the end-effector would be navigated to positions above obstacles at various elevations and positions throughout the field. The end-effector would always come within 0.5 inches of the previous attempt, regardless of the direction of approach. As a result, it is assumed that a model could be developed to correct for the positional errors. By navigating the end-effector through a network of calibration points and recording the error vectors, one could derive a mapping function to offset the error and bring the end-effector nearer to the target coordinates [39].

4.2c Disturbance Observations

During manual navigation of the system, few disturbances were seen. Due to the smooth motion of the DC gearmotors and the first order filter built into the winches' control systems (see Appendix B), few to no jolts were seen from the winches. The primary disturbances seen in this mode were due to the pendulum motion of the plumb bob during rapid acceleration.

During automated motion, additional disturbances were introduced by the control scheme used to attempt to maintain linear motion. The control loop took the error vector between the end-effector position and the ray connecting its initial and target positions, multiplied this vector by a gain, and added it to the base velocity vector. If this gain was too low, the

end-effector would fall or rise from the straight line trajectory. If the gain was set too high, it would oscillate about the trajectory line. If tuned correctly, the end-effector would move in a straight-line with no visible oscillations other than that created by the pendulum.

The exception to the disturbance-free motion described for the manual and automated control systems comes when crossing the boundaries between field quadrants. As stated previously, when changing quadrants, the non-supporting cable switches to a different cable. During this transition, a small skip can be witnessed. While tuning can reduce this impact, it was never fully removed from the system.

CHAPTER 5. AEROMOTIVE STABILIZATION OF A SUSPENDED PAYLOAD

One issue observed in the ETH phenotyping system is that the end-effector would tend to vibrate as a result of wind disturbance and rapid cable acceleration. Therefore, it was decided to develop an active stabilization system for the system being built for the University of Nebraska.

5.1 Motivation

To find a method of stabilizing the sensor platform, current methods of stabilizing CDPRs were explored. One primary method of stabilizing CDPRs is to use additional cables below the operating height of the end-effector to oppose the support cables, increasing cable tension and overall system rigidity [26], [33]. Due to the scale and geometry required for this application, it was determined that this method would not be feasible for a phenotyping system of significant size. Another method used to stabilize CDPR end-effectors is the use of a Stewart-platform on the end-effector, as is done in the FAST telescope [22], [40]. By suspending sensitive components from the remainder of the end-effector with a Stewart-platform, end-effector motion can theoretically be isolated to the upper portion of the end-effector, allowing the lower portion to remain stationary. The issue here is that such a system requires sophisticated controls, heavy hardware, and careful calibration. While this method is under consideration by the Universtiy of Nebraska – Lincoln, this research seeks to find a simpler, low-cost, robust method of stabilizing a suspended payload.

The primary challenge in stabilizing a suspended payload is the handling of reaction forces. Most active stabilization methods require reaction forces to be applied to a

supporting, grounded body. Due to their flexible nature, cables cannot provide consistent, grounded reaction forces. To overcome this challenge, this research focuses on providing reaction forces not with the support structures but with the surrounding air by use of a multirotor system. This system is herein referred to as the Instrument Platform Aeromotive Stabilization System (IPASS).

In recent years, multirotor systems, commonly referred to as quadcopters or drones, have exploded in popularity. Their applications range from military actions, to parcel delivery, to photography. There are even systems in place that are used for crop surveillance [11]–[14]. Currently, with the use of differential global positioning systems (DGPS) and automated controllers, systems are available that are capable of positioning over crops with accuracies within a couple of inches and that can hold that position under moderately harsh wind conditions. Due to the recent achievements in drone technology, researchers may ask why not simply use a free-flying multirotor system as opposed to a cable suspended end-effector mounted with a multirotor platform used merely for stabilization rather than support and locomotion? While long strides have been achieved in multirotor systems in recent years, there are still several key limitations to these systems for this application.

First, highly trained technicians would be required to run the system. Due to its ability to fly, such a system would require a licensed operator to use it. In addition, automation would be limited as a user would have to be constantly monitoring its performance in case of an accident [17]. By supporting the system by actuated cables, the system is no longer an unmanned aerial vehicle (UAV), and, therefore, does not fall under the same

federal scrutiny. Second, should hardware malfunction, user error, or harsh weather cause the system to crash, it can cause harm to crops, personnel, equipment, or passersby. In the case of the suspended system, should a malfunction occur or harsh weather hit, the cable system can maintain the end-effector's position, preventing harm to the surroundings as well as the end-effector itself. Finally, and most importantly for researchers, multirotor systems have limited flight times due to large power requirements. For a researcher to use drone-based systems around the clock, they would have to constantly exchange batteries in the UAV or else refuel and would experience regular downtime. Alternatively, they would require multiple UAVs running simultaneously to overlap these downtimes. This requires multiple UAVs, sensors, and operators as well as more complex coordination. By supporting the system by cables, power and communication can be wired into the end-effector, allowing for all-day, reliable use of the system without interruption.

5.2 Initial IPASS Prototype

Development of the IPASS system began with a feasibility analysis. To keep costs low and to accelerate the design, a quadcopter kit was used. An AeroQuad cyclone kit [41] was used as a starting point for its Arduino based flight controller and customizable frame.

5.2a Design

A one-twelfth-scale model of the field phenotyping system was constructed to aid system design. Its primary uses include:

- Designing control theory and hardware

- Confirming model simulations
- Studying system dynamics
- Testing full-scale end-effector stabilization systems

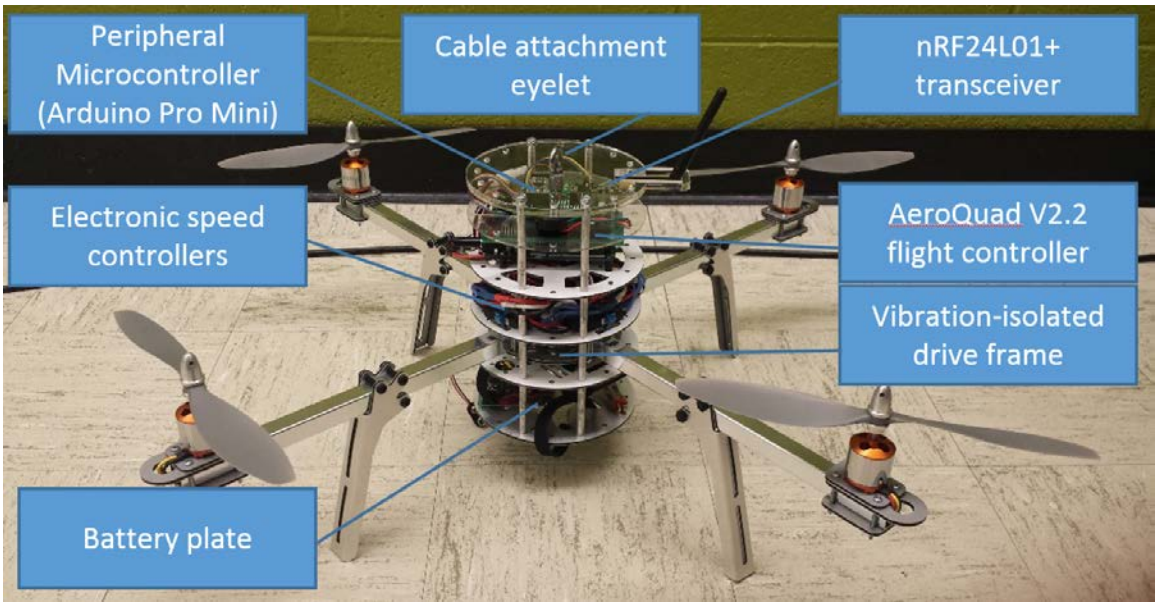

Figure 5-1. AeroQuad-based IPASS prototype. Tethers not shown.

For proof of concept, a quadcopter was suspended from the one-twelfth-scale system, and the quadcopter's response to disturbances was recorded. In addition, conceptual tests were performed to determine the feasibility of multiple control concepts discussed below. A prototype end-effector was constructed from a modified, Arduino-based quadcopter, shown in Figure 5-1, utilizing a standard quadcopter PID control based on accelerometer and gyroscope feedback [41]. This end-effector was chosen due to its hardware and software's ability to be easily modified as needed. Hardware specifications are provided in Table 5-1.

Table 5-1 Proof-of-Concept Model Design.

Component	Model
Frame	AeroQuad Cyclone Frame
Flight Controller	AeroQuad V2.2 Flight Control Board Kit
Motors	Cheetah A2217-9 Brushless Outrunner Motor
Propellers	APC 10x4.7 Propeller
ESCs	HobbyWing FlyFun Brushless ESC 30A
Battery	Fluoreon 11.1V 2200mAh Li-ion Battery
Transceiver	nRF24L01+ transceiver
Feedback IMU	Sparkfun 9DOF sensor stick
Data Acquisition Camera	GoPro Hero Session
Data Acquisition IMU	Bosch BNO055

The most notable design difference between this prototype and a standard quadcopter is that the drive system was reversed in order to push the system downwards, requiring a reversal of stabilization controls in the flight controller software. This was done to make air flow upwards, away from the crops so as to not cause the plants to sway, ruining the imaging and potentially damaging crops. In addition, should a light payload be attached, it prevents the end-effector from ever accidently attempting flight, causing it to rise into and become entangled with the cables. This also allows for temporarily increased cable tensions, increasing system rigidity. While increased tension can be achieved by using a heavier end-effector, using the stabilization system allows tension and rigidity to be

increased when stabilization is necessary but may reduce tension and thereby load on the winches, while moving, when stabilization is less important.

5.2b Experimentation

To determine the feasibility of the IPASS system, preliminary experiments, like the one shown in Figure 5-2, were conducted using the proof of concept model. From observations of full-scale systems, it was found that the primary disturbance modes are vertical translation and rotation about the roll and pitch axes. The experiments listed in Table 5-2 present the approximate settling time for several scenarios with the stability system on versus with the system off for the proof of concept model.

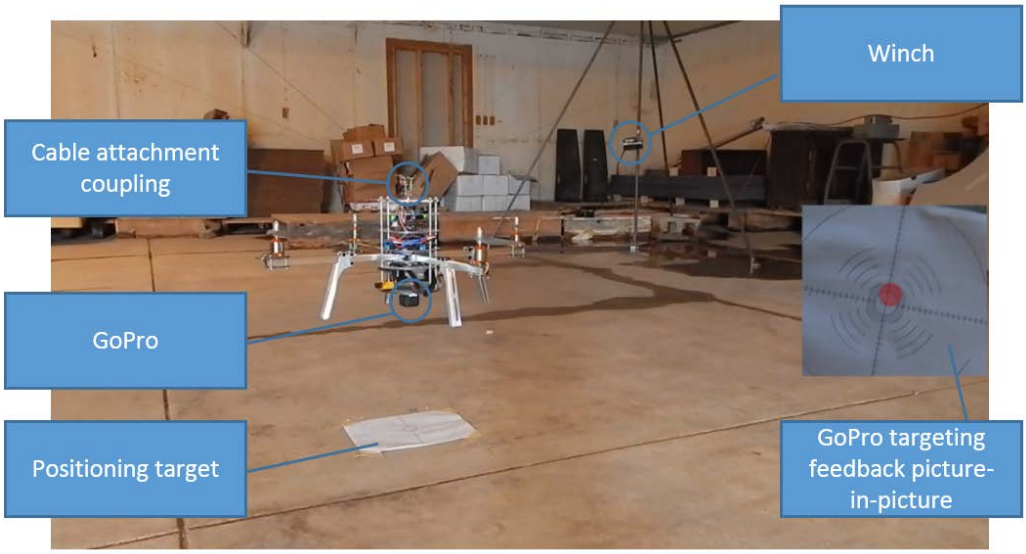

Figure 5-2. IPASS prototype experimentation video snapshot.[9]

[9] Picture-in-picture is video-feedback from downward-facing camera on end-effector, currently aimed towards a target below. The red dot is a post-processing feature to measure end-effector displacement.

For the listed experiments, it was found that the end-effector had a rotational natural frequency of 1.0 Hz and a vertical natural frequency of 2.7 Hz. Settling time for these experiments is defined as the time required for the end-effector to remain within 0.25 degrees of vertical for rotational disturbances or for no visible vertical motion[10] for vertical disturbances. Data were collected with a secondary, on-board IMU as well as two cameras. One camera was mounted on a nearby tripod while the second was mounted to the bottom of the end-effector, pointed towards a target on the floor below.

Table 5-2 Proof-of-Concept Model Setting Data.[11]

Experiment	Settling Time [System on]	Settling Time [System off]
A	2.9 sec	>30 sec
B	1.5 sec	>30 sec
C	2.0 sec	5-10 sec

A. End-effector is tilted and caused to swing with the stabilization system off. When the magnitude of oscillation reaches approximately thirty degrees off-vertical, the system is turned on and settling time is measured.

[10] These experiments were considered preliminary, proof-of-concept tests that would later be more thoroughly designed. Vertical deflection is one particular area where accurate measurements could not be taken. As a result, vertical motion was based purely on the absence or presence of motion in surveillance video.

[11] Settling times are based on frame-by-frame observations of video evidence. Therefore, the raw data could not be presented in this work. Links to videographic data are available in Appendix C.

B. The end-effector is held at approximately twenty degrees from vertical with the system on. The end-effector is then released, and settling time is measured.
C. One cable is randomly plucked to induce a vertical disturbance to the end-effector of approximately one inch vertical oscillations while the system is running. Disturbance is suddenly removed, and settling time is measured.

5.2c Design Considerations

The following behaviors were monitored to determine the capabilities of the multirotor concept, as well as to explore potential further applications:

- The effect of inverted propellers on airflow and operability
- Ability to counteract cable vibrations
- Ability to counteract oscillations from end-effector navigation
- Ability to counteract wind disturbances
- Ability to stably reorient sensors

5.2d Inverted propellers

It was observed that reversing airflow did not interfere with the stability system's performance. In addition, greatly reduced disturbances were seen below the end-effector than when airflow was directed downwards.

5.2e Cable vibrations

Experimentation showed that cable vibrations primarily lead to vertical oscillations of the end-effector. For certain disturbances, rotational oscillations were seen to build with the

stabilization system off. However, when the system was on, they remained within the 0.25 degree limits. During the experiments, it was seen that, while the end-effector would stabilize vertical disturbances quickly after the disturbances subsided, it could not cancel them out while they occurred. Given that these are predicted to be continuous disturbances at full-scale due to tower vibrations and wind, this presents an issue for this design.

5.2f Navigational disturbances

As this stabilization system is to be used on a mobile end-effector, an experiment was conducted to determine its ability to stabilize the end-effector while in motion. During this experiment, it was seen that the end-effector could remain within 0.25 degrees of vertical during motion, except when accelerating or decelerating. At these moments, jolts of up to one degree could occur depending on acceleration of the cables.

Intermittently during the experiment, a cable would jolt due to a navigational error. This would, in turn, cause the end-effector to experience minor vibrations that would subside with 1.5 seconds. These disturbances are excluded from the analysis as they are due to cable system errors and are not expected in the full-scale system. However, they serve to further indicate the high dependence of end-effector stability on cable vibrations.

5.2g Wind disturbances

To test the system's ability to compensate wind disturbances, a leaf blower was used to direct airflow over the end-effector. While this model is a poor portrayal of real wind conditions, it was used to illustrate one limitation of the stabilization system. To fight

wind, the end-effector must be able to generate a horizontal force in the opposing direction. To achieve this, the end-effector must be tilted so that the propellers are no longer directly vertical. From this experiment, it was determined that the stabilization system must be capable of providing horizontal forces without tilting the end-effector if it is to combat wind disturbances while remaining down-facing.

5.2h Sensor orientation

While phenotyping requires certain sensors to remain down-facing during scanning, certain sensors must be reoriented during scanning. Traditionally, this required mounting the sensor package to a gimbaled platform on the end-effector. This requires extra mass to be added to the end-effector. To overcome this, an experiment was conducted to test the possibility of using the stabilization system to alter end-effector roll and pitch in place of a gimbal.

The proof-of-concept model showed limited capabilities in this respect. However, it is believed that mobility was limited due to the low center of mass with respect to the support point. It is believed that the motors used lacked the power to deflect the center of mass and hold it steady on a new position. A further limiting factor was the distance between the cables and the propellers. The end-effector could not tilt beyond fifteen degrees in most orientations due to interference with the cables. However, preliminary tests demonstrated limited ability to maintain an angled position, indicating that with further design revisions, gimbal motion may be replicated in future systems.

5.3 Proof-of-Concept Results

Proof-of-concept experiments indicated that a multirotor stabilization system has the ability to overcome rotational disturbances. However, they also indicate a strong influence from cable instabilities. Additionally, this prototype is unable to reject horizontal disturbances from wind. It is therefore concluded that further measures are required to isolate the end-effector from cable disturbances as well as to generate horizontal forces without reorienting the end-effector.

5.4 Full-scale Prototype

Based on the analysis with the initial IPASS prototype, it was determined that the use of a multirotor system to stabilize a suspended payload was feasible for this application. As a result, a new, full-scale prototype was developed from scratch using a new frame, new flight controller, and new drive configuration.

5.4a Design of Full-scale IPASS

Based on the analysis from the proof-of-concept end-effector, a full scale IPASS, shown in Figure 5-3, was designed to allow for greater isolation of the platform from the cable system as well as generate horizontal forces. For further design information and drawings, reference Appendix F. For initial experimentation, the same flight control system (including propellers, motors, and electronic speed controllers (ESCs)) was used. Modular mounts and connections were used to allow for simpler upgrades in the future. An Arduino Mega continued to be used as the flight controller. However, rather than using the Aeroquad software, a new control system was developed from scratch.

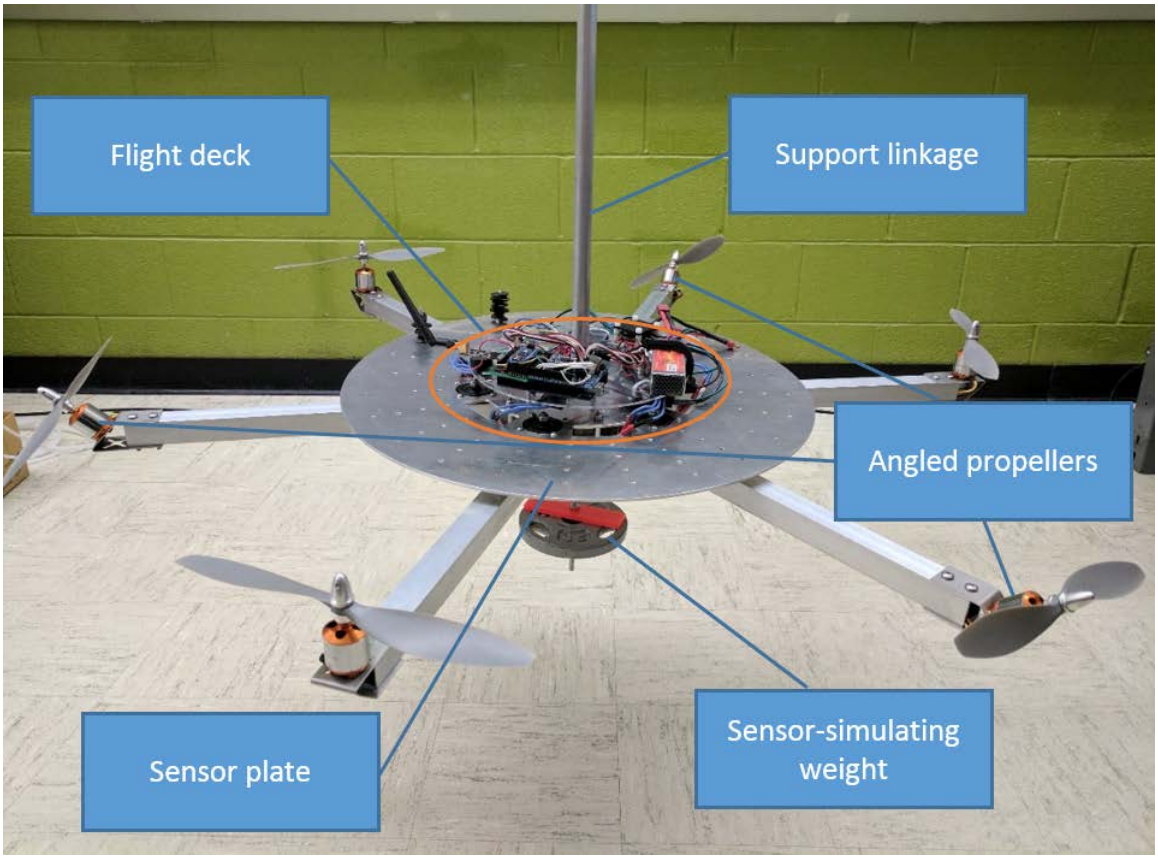

Figure 5-3. IPASS full-scale prototype, using three vertical and three angled propellers.

For sensors and peripheral controls, several changes were made. A new interfacing shield was developed for the flight controller, allowing for an Arduino Nano to be mounted to the system to perform secondary tasks, such as communicating with the system controller, controlling on-board displays and LEDs, and interfacing with phenotyping sensors. The Sparkfun 9-degree-of-freedom sensor stick was also replaced with a BNO055 9-axis absolute orientation sensor broken out on an Adafruit board [42]. This IMU is equipped with an MCU to run fusion algorithms, meaning it can return absolute orientation data rather than raw sensor data, reducing the computational load on the flight controller [43], [44]. nRF24L01+ transceivers continued to be used in this prototype to

simplify controller implementation, but should be replaced in future revisions with more reliable and powerful means of communication.

One of the primary limitations seen in the proof-of-concept experiments was the inability to counteract horizontal forces caused by wind. As this system is to operate in Nebraska, it must be capable of counteracting high wind speeds. To allow for the generation of lateral forces without tilting the end-effector, the propeller configuration was altered. Instead of using four upward facing propellers, six angled propellers were used. Three propellers were left upward facing to generate torques about the roll and pitch axes. The remaining three propellers, however, were angled forty-five degrees inwards to generate thrust vectors with lateral components to move the end-effector laterally. See Figure 5-3. Rotation and translation with respect to the vertical axis is performed by methods standard of multirotor systems: average thrust on the propellers controls the vertical translation of the end-effector, and motor torques generate rotation about the z axis. Under this configuration, six-degree motion should be achievable by correctly coordinating motor speeds.

The primary influence on settling time seen in the proof-of-concept experiments was the positioning of the end-effector center-of-mass. In the previous experiments, the mass was located so far below the support point of the end-effector that a large rotational inertia had to be overcome to stabilize the end-effector. To reduce system inertia and achieve a faster response, the center-of-mass should be located at or just below the end-effector support point, as illustrated by Figure 5-4. This introduces design challenges as the

propellers should be kept a safe distance away from the cables. To accommodate, an intermediate linkage is used between the cable attachment plate and the sensor platform.

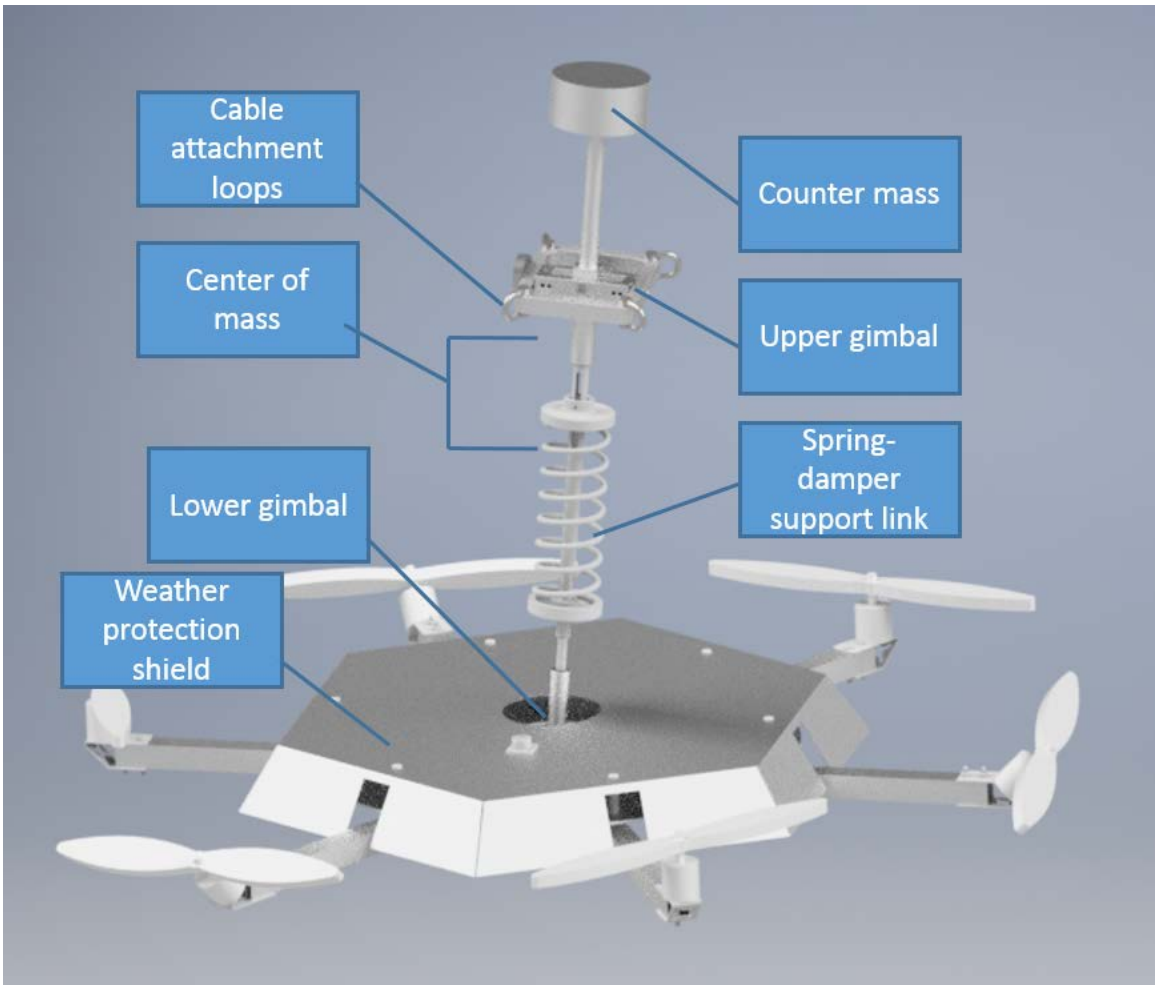

Figure 5-4. Full-scale end-effector model.

A gimbal is mounted to either end of the linkage to allow for free motion of the sensor platform with respect to the cable attachment plate. By suspending the sensor platform from the cable attachment plate, a large pendulum is created. This has the potential to require large lateral forces to stabilize should the system experience rapid acceleration. To overcome this issue, a counter mass (possibly containing non-sensor payload, such as

routers and power distribution devices) can be mounted above the cable attachment point to align the center of mass of the end-effector and linkage with the cable attachment point. In addition, the gimbal between the linkage and sensor platform can be positioned to align with the center of mass of the platform.

A secondary impact of the use of the linkage is the ability to make micro-positioning corrections. With the sensor platform attached directly to the cable attachment point, limited lateral motion is possible due to cable tensions restricting the end-effector's position. By separating the platform via the linkage, the sensors can theoretically be relocated a few inches in any direction to accommodate for cable system positioning inaccuracies. Finally, by building a spring-damper into the linkage, further vertical motion can be achieved. It also further isolates the sensor platform from cable vibrations.

The final major design change was the modified layout of the sensor platform relative to its gimbal. By more carefully designing the weight distribution of the end-effector, inertia can be reduced and faster response times could be seen with reduced power requirements. To achieve this, sensors are distributed between two plates, as shown in Figure 5-5. The first plate is located directly under the gimbal and is of a small diameter. This allows a sensor whose mass dominates the center-of-mass position to be located in-line with the gimbal, preventing the end-effector from tilting to one side. The drawback is that this can produce a significantly low center-of-mass. Therefore, the second sensor plate is located above the gimbal so that secondary sensors can be positioned with their centers-of-mass at or above the gimbal. While further tuning of the COM position can be achieved by the addition of calibration weights to the sensor plates, steps were taken to avoid this to

reduce downtime. The gimbal for the end-effector is mounted to a threaded body that is capable of adjusting its vertical position within the end-effector. This allows the user to calibrate the center-of-mass without the need to coordinate calibration weights. All that would be needed is to rotate the gimbal component until the center-of-mass is located just below the gimbal.

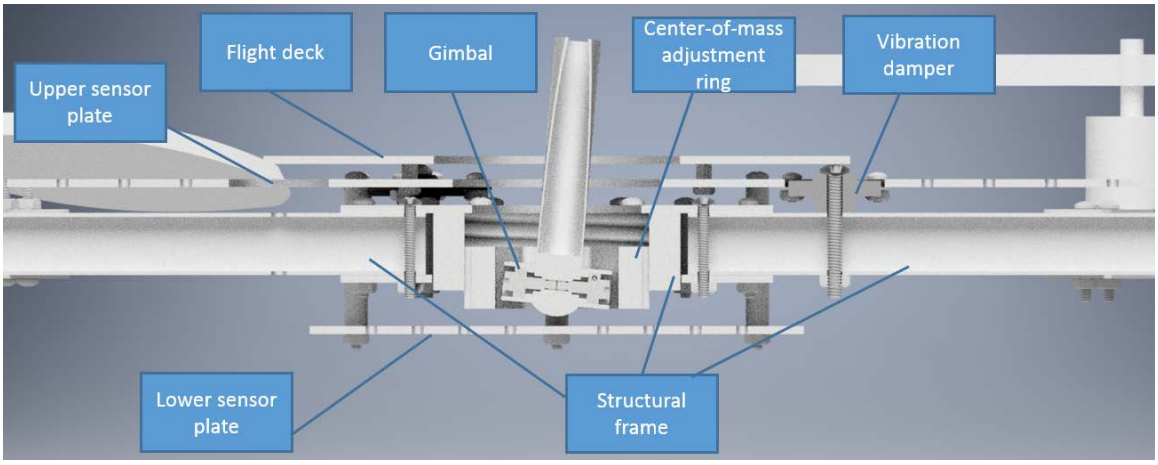

Figure 5-5. Full-scale sensor platform cross-section view.

The two sensor plates are isolated from the gimbal and sensor platform frame via rubber standoffs mounted to each of the arms of the device. This is intended to isolate the sensor plates from the vibrations generated by the motors. The flight deck is mounted to the top of the upper sensor plate. The flight circuit, including Arduinos, ESCs, and the IMU, are mounted to this plate. Due to the layout of the motors, propellers, and flight deck, the sensor platform naturally has a high center-of-mass. While this causes the device to be unstable, this design is intentional. By causing the center-of-mass of the platform to be above the gimbal, attachment of the payload will result in a center-of-mass nearer to the gimbal than if the platform's center-of-mass was below the gimbal.

5.4b Control Derivation

In order to achieve six-degree motion of the end-effector, six propellers are used in this prototype. In order to achieve horizontal forces without tilting the end-effector, not all propellers can be oriented vertically. To separate the controls, three propellers remained vertical to control roll and pitch while the other three were tilted forty-five degrees off-vertical to provide lateral forces, as illustrated by Figure 5-6. The total thrust of all six propellers would produce a vertical force against the support cables, providing control of vertical motion. Finally, both sets of three propellers would turn in opposing directions. As a result, increasing the speed of, for example, motors one, three, and five while decreasing the speed of motors two, four, and six would generate a torque about the vertical axis, inducing rotation about the vertical axis.

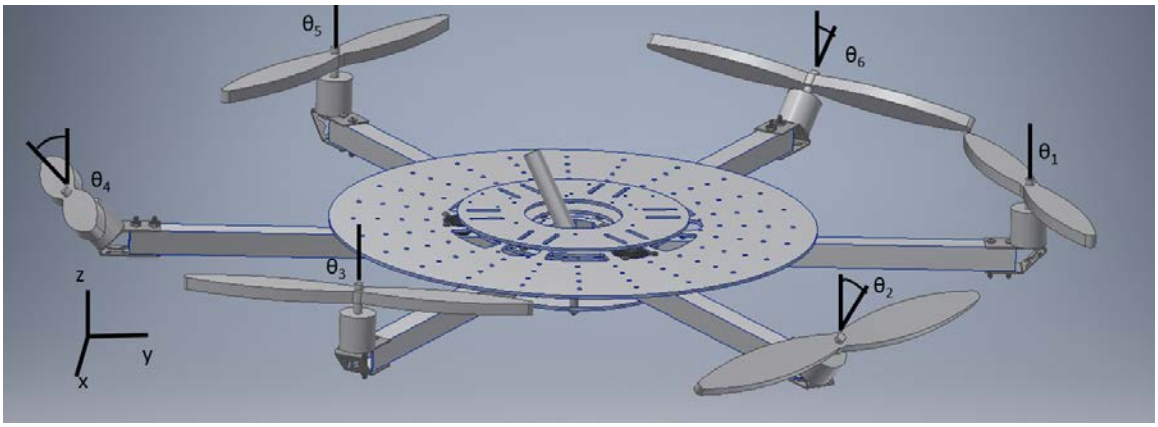

Figure 5-6. IPASS propeller layout.

Due to the substantial changes in system layout, the previous control system could not be used. The new setup had to be modeled to derive a new control system. Due to the highly symmetrical design of quadcopters, very little knowledge of the end-effector geometry or

its drive system are required. However, due to the lack of symmetry in this end-effector, the system dynamics had to be modeled.

By taking the sum of forces along the x-axis in the model:

$$\sum F_x = M\ddot{x} = -T_2 s_2 c_{30} - T_3 s_3 c_{30} + T_5 s_5 c_{30} + T_6 s_6 c_{30} - (Mg + T_1 c_1 + T_2 c_2 + T_3 c_3 + T_4 c_4 + T_5 c_5 + T_6 c_6)\frac{x}{L} \quad (5\text{-}1)$$

where M is the mass of the end effector, T_n is the thrust force generated by the n^{th} motor, s_n and c_n equal $\sin(\theta_n)$ and $\cos(\theta_n)$, respectively, and c_{30} and s_{30} equal $\cos(30°)$ and $\sin(30°)$, representing the angle between the associated motor arm and the x-axis. The portion of the equation in parentheses represents the forces generated by the support linkage. For this model, it is assumed that the weight of the end-effector dominates this force, and the remaining terms are neglected.

Similarly for the y and z-axes:

$$\sum F_y = M\ddot{y} = -T_1 s_1 - T_2 s_2 s_{30} + T_3 s_3 s_{30} + T_4 s_4 + T_5 s_5 s_{30} - T_6 s_6 s_{30} - (Mg + T_1 c_1 + T_2 c_2 + T_3 c_3 + T_4 c_4 + T_5 c_5 + T_6 c_6)\frac{y}{L} \quad (5\text{-}2)$$

$$\sum F_z = M\ddot{z} = -T_1 c_1 - T_2 c_2 - T_3 c_3 - T_4 c_4 - T_5 c_5 - T_6 c_6 + \left(-Mg + (Mg + T_1 c_1 + T_2 c_2 + T_3 c_3 + T_4 c_4 + T_5 c_5 + T_6 c_6)\frac{\sqrt{L^4 - x^2}\sqrt{L^4 - x^2}}{L^2}\right) \quad (5\text{-}3)$$

Taking the moments about the three axes:

$$\sum M_x = I_x\ddot{\alpha} = -T_1Lc_1 - T_2Lc_2s_{30} + T_3Lc_3s_{30} + T_4Lc_4 + T_5Lc_5s_{30} - T_6Lc_6s_{30} - T_2\tau c_2c_{30} + T_6\tau c_6c_{30} \quad (5\text{-}4)$$

$$\sum M_y = I_y\ddot{\beta} = T_2Lc_2c_{30} + T_3Lc_3c_{30} - T_5Lc_5c_{30} - T_6Lc_6c_{30} - T_2\tau c_2s_{30} + T_4\tau c_4 - T_6\tau c_6s_{30} \quad (5\text{-}5)$$

$$\sum M_z = I_z\ddot{\gamma} = T_1\tau c_1 - T_2\tau c_2 + T_3\tau c_3 - T_4\tau c_4 + T_5\tau c_5 - T_6\tau c_6 \quad (5\text{-}6)$$

where I is the inertia about the respective axis, L is the length of each motor arm, α, β, and γ are rotation about the x, y, and z-axes, respectively, and τ is the constant relating propeller thrust to propeller torque for the selected hardware.

By rearranging and simplifying these equations, one reaches the following model,

$$\ddot{\boldsymbol{X}} = [\boldsymbol{A}]\boldsymbol{T} - \boldsymbol{B}\boldsymbol{X} \quad (5\text{-}7)$$

Where:

$$\boldsymbol{X} = [x \quad y \quad z \quad \alpha \quad \beta \quad \gamma]^T \quad (5\text{-}8)$$

$$\boldsymbol{T} = [T_1 \quad T_2 \quad T_3 \quad T_4 \quad T_5 \quad T_6]^T \quad (5\text{-}9)$$

$$[\boldsymbol{A}] = \begin{bmatrix} 0 & \frac{-\sqrt{3}s_2}{2M} & \frac{-\sqrt{3}s_3}{2M} & 0 & \frac{\sqrt{3}s_5}{2M} & \frac{\sqrt{3}s_6}{2M} \\ \frac{-s_1}{M} & \frac{-s_2}{2M} & \frac{s_3}{2M} & \frac{s_4}{M} & \frac{s_5}{2M} & \frac{-s_6}{2M} \\ \frac{-c_1}{M} & \frac{-c_2}{M} & \frac{-c_3}{M} & \frac{-c_4}{M} & \frac{-c_5}{M} & \frac{-c_6}{M} \\ \frac{-Lc_1}{I_x} & \frac{-2Lc_2-\sqrt{6}\tau}{4I_x} & \frac{Lc_3}{2I_x} & \frac{Lc_4}{I_x} & \frac{Lc_5}{2I_x} & \frac{-2Lc_6+\sqrt{6}\tau}{4I_x} \\ 0 & \frac{2\sqrt{3}Lc_2-\sqrt{2}\tau}{4I_y} & \frac{\sqrt{3}Lc_3}{2I_y} & \frac{\sqrt{2}\tau}{2I_y} & \frac{-\sqrt{3}Lc_5}{2I_y} & \frac{-2\sqrt{3}Lc_6-\sqrt{2}\tau}{4I_y} \\ \frac{\tau c_1}{I_z} & \frac{-\tau c_2}{I_z} & \frac{\tau c_3}{I_z} & \frac{-\tau c_4}{I_z} & \frac{\tau c_5}{I_z} & \frac{-\tau c_6}{I_z} \end{bmatrix} \quad (5\text{-}10)$$

$$\boldsymbol{B} = \begin{bmatrix} \frac{Mg}{L} & \frac{Mg}{L} & 0 & 0 & 0 & 0 \end{bmatrix} \tag{5-11}$$

Angles of zero degrees for θ_1, θ_3, and θ_5 and angles of forty-five degrees for θ_2, θ_4, and θ_6 may then be substituted into **A**. To control the system, a user must be able to calculate each control input, $\boldsymbol{T}$, based on system dynamics, $\ddot{\boldsymbol{X}}$ and $\boldsymbol{X}$. By rearranging (5-7), one gets:

$$\boldsymbol{T} = [\boldsymbol{A}^{*-1}]\left(\boldsymbol{M}\ddot{\boldsymbol{X}} + \boldsymbol{B}\boldsymbol{X}\right) \tag{5-12}$$

Where:

$$\boldsymbol{M} = \begin{bmatrix} M & M & M & \frac{I_x}{L} & \frac{I_y}{L} & \frac{I_z}{\tau} \end{bmatrix}^T \tag{5-13}$$

$$[\boldsymbol{A}^{*-1}] =$$

$$\begin{bmatrix} 0.6667\frac{\tau}{L} & 0.6667 & -0.1667 & -0.6667 & 0 & 0.1667 \\ -0.8165 & -0.4714 & -0.2357 & 0 & 0 & -0.2357 \\ -0.5774 - 0.3333\frac{\tau}{L} & -0.3333 - 0.5774\frac{\tau}{L} & -0.1667 & 0.3333 & 0.5774 & 0.1667 \\ 0 & 0.9428 & -0.2357 & 0 & 0 & -0.2357 \\ -0.5774 - 0.3333\frac{\tau}{L} & -0.3333 + 0.5774\frac{\tau}{L} & -0.1667 & 0.3333 & -0.5774 & 0.1667 \\ 0.8165 & -0.4714 & -0.2357 & 0 & 0 & -0.2357 \end{bmatrix} \tag{5-14}$$

Based on (5-12), a user can generate a control scheme to drive the system based on the system dynamics. To obtain the dynamic data, it was chosen to use two separate IMUs: one for translational motion, and the other for rotational motion. The IMU chosen for this prototype was an Adafruit breakout board mounted with a Bosch BNO055 9-axis absolute orientation sensor [42]. This chip was chosen due to the fact that it contained not

only a triaxial 14-bit accelerometer, a triaxial 16-bit gyroscope, and a triaxial geomagnetic sensor, but also a 32-bit cortex M0+ microcontroller running Bosch Sensortec sensor fusion software. This meant that while the chip could provide raw sensor data, it would also calculate absolute orientation data as well. The algorithms were found to filter the results very effectively, producing very little noise in values. It also is designed to output data at a rate of up to 100 Hz, and can communicate over either I^2C or UART interfaces. The downside to the chip was that it included a baseline library, provided by Adafruit. As a result, an entirely new library had to be created (see Appendix D).

To collect rotational data, one IMU was mounted directly to the sensor platform's flight deck. Absolute orientation roll, pitch and yaw data, as well as raw gyroscope data, were retrieved from the IMU for use in the α, β, γ control loops. The primary limitation of standard IMU chips (without GPS or range finding technology) is their limited ability to track position and velocity [45]. While accelerometer data could be integrated to approximate velocity and position given known initial conditions, integration errors can compound very quickly, making the results meaningless. Therefore, to determine linear motion for use in the x, y, and z control loops, another approach was taken. A second IMU was mounted at the top of the linkage that joins the sensor platform to the cable-attachment plate. By reading rotational orientation and velocities with this IMU, translational motion of the sensor platform with respect to the cable-attachment plate frame of reference could be calculated.

$$x = H \sin \beta_2 \tag{5-15}$$

$$\dot{x} = \dot{\beta}_2 H \cos \beta_2 \tag{5-16}$$

$$y = H \sin \alpha_2 \tag{5-17}$$

$$\dot{y} = \dot{\alpha_2} H \cos \alpha_2 \tag{5-18}$$

$$z = H(1 - \cos \alpha_2 \cos \beta_2) \tag{5-19}$$

$$\dot{z} = \sqrt{\left(\dot{\beta}_2 * H * \sin \beta_2\right)^2 + (\alpha_2 * H * \cos \alpha_2)^2} \tag{5-20}$$

where H is the distance between the cable-attachment plate and the sensor platform, and α_2, β_2, and γ_2 are the orientation angles for the second IMU. As stated, these equations provide the location of the sensor platform with respect to the cable-attachment plate frame of reference, not to ground. However, due to the nature of the particular CDPR used in this research, it can be assumed for these calculations that the cable-attachment point does not move laterally based on scale testing. As a result, lateral velocity values should be accurate. Based on scale-testing, the primary translation disturbance seen in the system is vertical displacement. Therefore, it cannot be assumed that the vertical position of the cable-attachment plate is constant. However, experimentation with the proof-of-concept prototype showed that a PD controller using the vertical accelerometer data was adequate to stabilize vertical vibrations due to its oscillatory nature.

While the system has been modeled and system inputs have been accounted for, the model output, desired propeller thrust, must still be converted to a usable input to the motors. The drivers used in this prototype were HobbyWing FlyFun Brushless ESC 30A drivers [46]. These drivers use standard RC input signals to control their motors [47].

This works by transmitting a square wave signal to the driver with a period of 20,000 microseconds. By fluctuating the duration of the high-side of the pulse between 1,000 and 2,000 microseconds, the driver causes the associated motor to run at a given voltage. When the high pulse lasts 1,000 microseconds, the motor is fed zero volts. When the high pulse lasts 2,000 microseconds, the motor is fed the full supply voltage provided to the driver. The voltage is linearly related to pulse width between these two points. As a result, it is now known that the cross-over between software logic and motor response is a linear mapping between two variables. The variable on the software side, hereafter referred to as the throttle, ranges from 0 to 1,000. The 1,000 offset is removed to simplify mapping. A value of 1,000 is then added to the throttle before writing the signal to the drivers. The variable on the hardware side is the ratio between the motor voltage, V and the voltage of the system, V_{sys}.

$$throttle = \frac{V}{V_{sys}} 1000 \tag{5-21}$$

The final step is to determine the correlation between motor voltage and propeller thrust. For this prototype, APC 10x4.7SF propellers are used. Based on tables provided in their data sheets [48], propeller thrust and torque are functions of propeller speed as follows.

$$Thrust = 2.367E-7 * RPM^2 - 2.932E-4 * RPM = a * RPM^2 + b * RPM \tag{5-22}$$

$$Torque = 4.227E-9 * RPM^2 - 2.138E-7 * RPM = c * RPM^2 + d * RPM \tag{5-23}$$

where RPM is the rotation speed of the propeller.

By combining these equations, it can be found that torque can be approximated by a linear relationship to thrust. This provides the missing τ variable required back in (5-6).

$$Torque \approx \frac{c}{a} * Thrust = \tau * Thrust \tag{5-24}$$

Now that the correlation between thrust and speed have been determined based on the propellers, the correlation between speed and voltage must be found based on the motor. The motors used in this prototype are Cheetah A2217-9 brushless motors [49]. This motor has a Kv value of 950 and resistance (R) of 95 mOhms. For a brushless motor, speed can be predicted by using (5-25), where I is the current running through the motor [50].

$$RPM = K_V(V - R\mathrm{I}) = K_V\left(V - R * \frac{Torque}{K_t}\right) = K_V\left(V - R * \frac{\tau * Thrust * 2\pi * K_v}{60}\right) \tag{5-25}$$

Substituting this into (5-22),

$$Thrust = a * \left(K_V\left(V - R * \frac{\tau * Thrust * 2\pi * K_v}{60}\right)\right)^2 + b * K_V\left(V - R * \frac{\tau * Thrust * 2\pi * K_v}{60}\right) \tag{5-26}$$

Furthermore, by substituting (5-21) into (5-26),

$$Thrust = a * K_v^2\left(\frac{throttle * V_{sys}}{1000} - R * \frac{\tau * Thrust * 2\pi * K_v}{60}\right)^2 + b * K_V\left(\frac{throttle * V_{sys}}{1000} - R * \frac{\tau * Thrust * 2\pi * K_v}{60}\right) \tag{5-27}$$

By rearranging this equation, solving for throttle,

$$throttle = D_1 Thrust + D_2 + D_3\sqrt{D_4 Thrust + D_5} \tag{5-28}$$

$$D_1 = \frac{100\tau\pi RK_v}{3V_{sys}} \tag{5-29}$$

$$D_2 = \frac{-500b}{aK_vV_{sys}} \tag{5-30}$$

$$D_3 = \frac{500000}{aK_vV_{sys}} \tag{5-31}$$

$$D_4 = \frac{a}{250000} \tag{5-32}$$

$$D_5 = \frac{b^2}{1000000} \tag{5-33}$$

In addition to this analytical solution, an equation was derived experimentally to determine throttle as a function of desired thrust. This experiment consisted of mounting a single motor and propeller to one end of a load cell while the other end was mounted to a long shaft, allowing to the apparatus to be held away from the user and surrounding obstructions to airflow. The device is shown in Figure 5-7. The throttle was then held at multiple values for a duration of five to ten seconds. The thrust generated over that period was averaged and compared to the theoretical thrust to determine the accuracy of the analytical model. The results are presented in Figure 5-8.

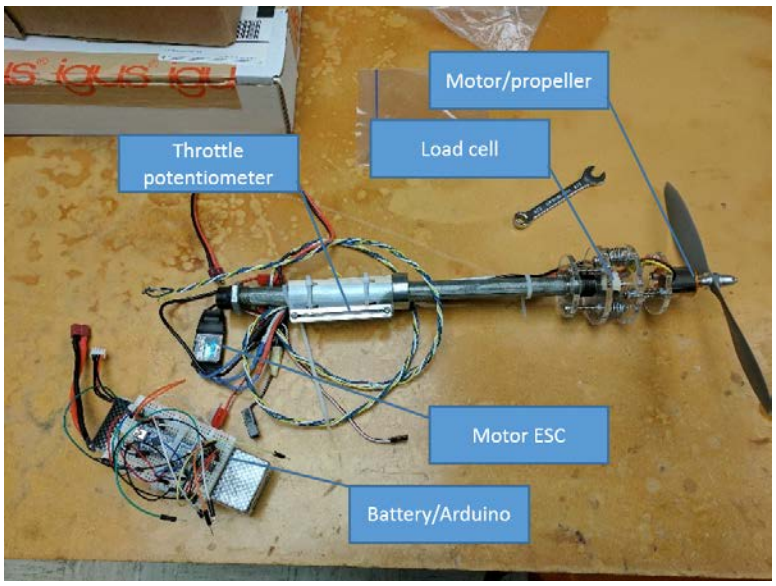

Figure 5-7. Propeller thrust measurement apparatus.

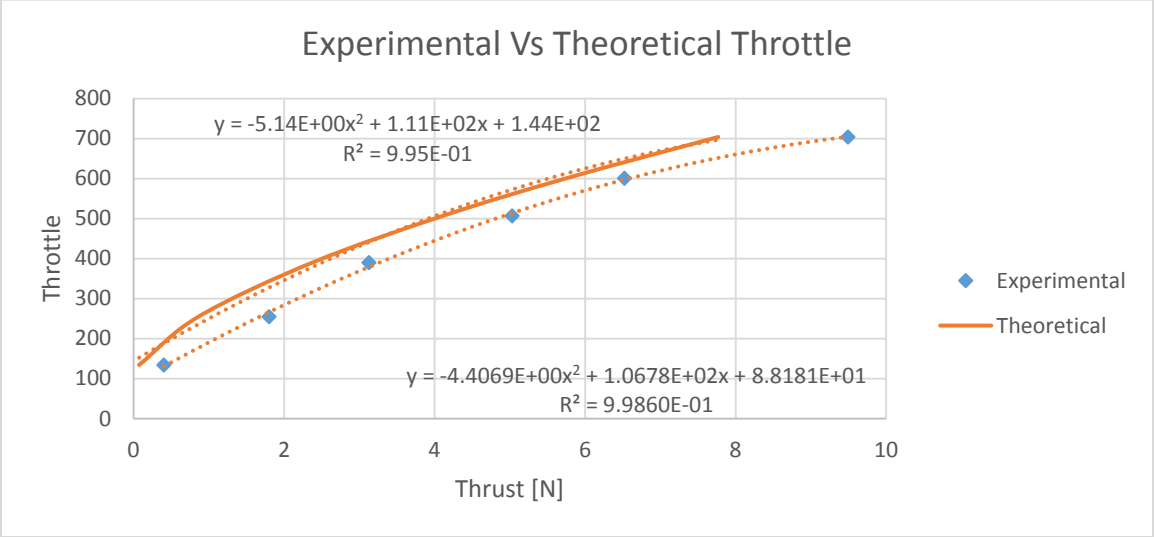

Figure 5-8. Experimental vs. theoretical throttle-thrust curves.

Both of these models were used in the software. No noticeable difference was seen in the system's performance.

With this, the model is complete and ready to be implemented into a controller. For this prototype, a simple PD controller was used. The control calculations therefore were as follows.

1. Receive input from user, either a desired sensor platform orientation or angular and translational velocity vectors
2. Receive end-effector dynamics data from IMUs
3. Compare user input to current dynamics to create error terms
4. Plug error terms into PD controller to find desired acceleration values
5. Use (5-12) to determine thrust values based on current dynamics and PD controller output
6. Calculate throttle for each motor using (5-28) or the experimental curve derived from Figure 5-8
7. Transmit throttle values to each ESC
8. Repeat

5.4c Control Design

The aeromotive control system architecture is laid out in Figure 5-9 below. Three separate microcontroller units (MCUs) are used to control the system. The first is the flight control MCU, which is responsible for performing all of the stabilization calculations and communicates with the motor drivers. The second is the peripheral controls MCU, which is mounted to the end-effector and is used to perform secondary operations such as relay control information, check battery voltage, interface with phenotyping sensors, control lights and indicators, etc. The final MCU is the Controller

MCU. This MCU is located in the user's controller and transmits user input to the peripheral MCU, which relays the data to the flight control MCU. The scripts for these MCUs can be found through Appendix D.

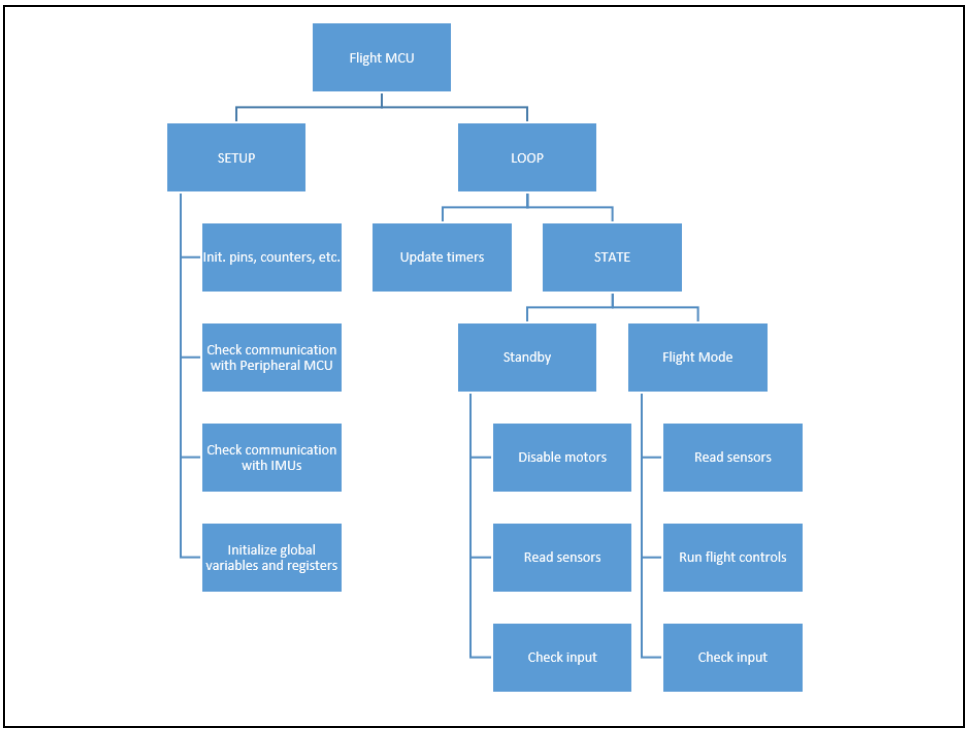

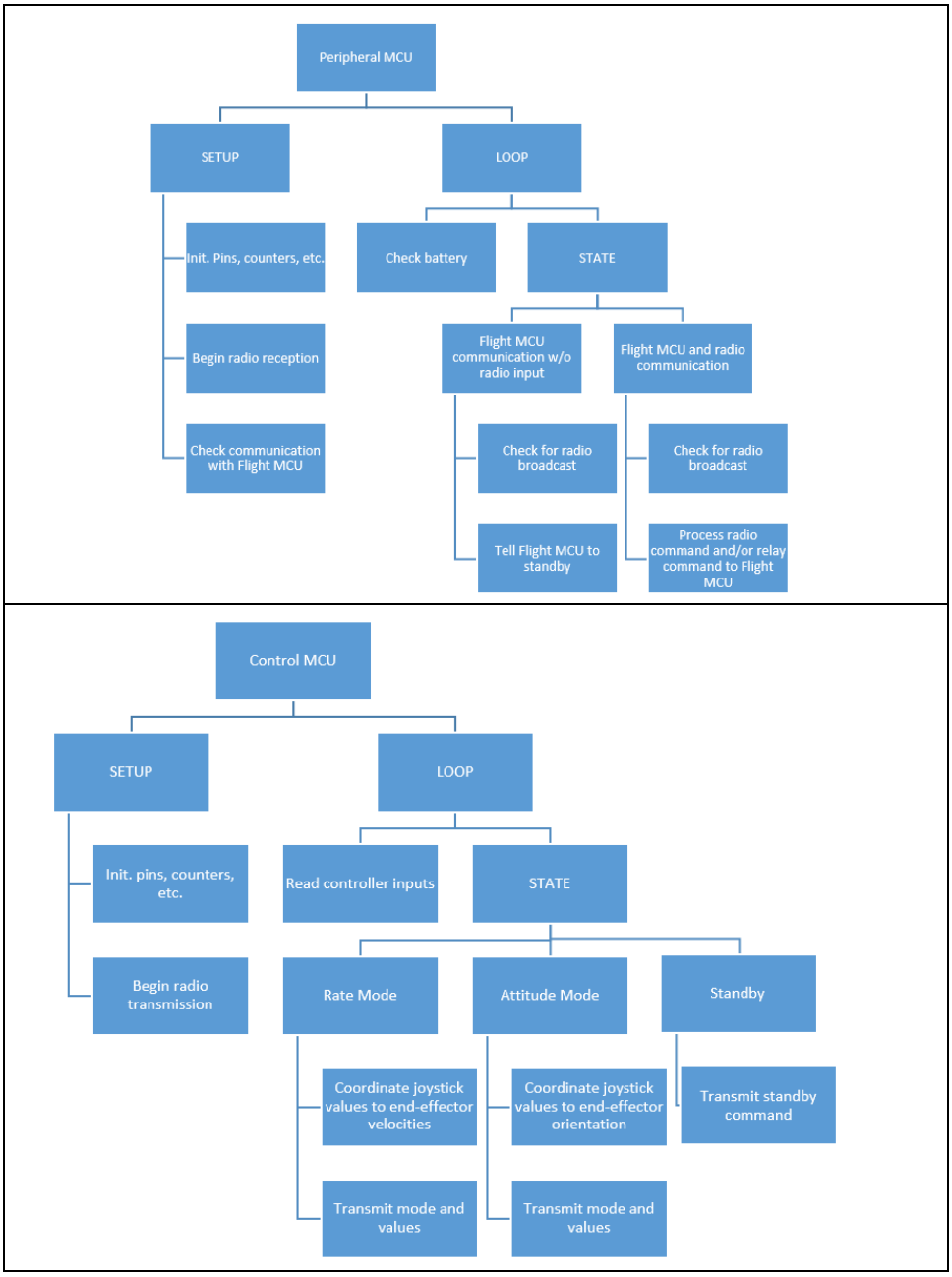

Figure 5-9. IPASS control scheme. (top) Control scheme for IMU responsible for controlling stabilization system. (center) Control scheme for IMU responsible for controlling secondary end-effector features as well as end-effector communications. (bottom) Control scheme for IMU responsible for relaying user input to the end-effector.

After the flight control MCU has performed all of its setup routines, it enters its main loop, where it runs through a state machine driven by the MCU's timers. The state

machine cases are activated at various frequencies, ranging from 1 Hz to 100 Hz to cause the associated tasks to be performed at the desired frequency. For example, the “100 Hz” flag in a status register is activated every 10 milliseconds, causing the system to enter the associated state. One function in this state reads the two system IMUs as their maximum output rate is 100 Hz. Within each state, the flight controller then determines whether the system is to behave under standby or active conditions and acts accordingly.

While the peripheral MCU is intended to be used for an array of operations, it currently only performs two tasks: monitor the battery voltage and relay information between the flight controller and the user. After running its setup routines, it enters its main loop where it first checks battery voltage. If the levels have dropped too low, the MCU sends a command to the flight controller, telling it to disable the motors. It also activates an alarm to alert the user that it is time to recharge the battery. After the battery is checked, the MCU enters a conditional state machine. If the MCU is receiving commands from the user, it sets the state to its operational mode, where it relays commands between the user and the flight controller. If communication with the user is ever lost, it switches to a standby mode and tells the flight controller to enter standby mode as well.

The controller MCU follows the same basic architecture as the other two MCUs. After running its setup routines, it enters its main loop, where it reads the controller’s joystick and switch driven inputs. These inputs are then used to determine the mode to enter in the controller’s state machine. One switch is used to enable or disable the flight system. If off, the controller transmits a standby command to the peripheral controller, which relays the command to the flight controller MCU. If this switch is active, a second switch is

used to determine whether the system should perform in rate or attitude mode. From there, the positions of the two controller joysticks are correlated to system commands, and an appropriate command is transmitted to the peripheral MCU to be relayed to the flight controller MCU.

5.4d Experimentation

Extensive work was conducted in an attempt to produce a working IPASS system that could provide six degrees of freedom; however, inadequate time was available to produce a fully operational system. The prototype developed utilized functional, albeit hobbyist, hardware, and the software was fundamentally operational. Based on preliminary experiments, the end-effector appeared to be capable of stabilizing rotational disturbances as well as the initial prototype. However, the system was never able to produce translational motion without impacting rotation. While experiments were conducted with this prototype, due to the failure to complete the stabilization system, no formal results are included in this report. One video illustrating its behavior is provided through Appendix C.

5.5 Future Work

In developing the most recent IPASS prototype, several potential modifications were found that should be implemented in the next iteration.

Due to its power requirements, the current prototype may not be feasible. Its current power draw would require a large battery bank on the end-effector, likely exceeding the weight limits of the current CDPR system. Should power be provided by a tethered

power connection running through the CDPR cables, the power could be supplied continuously; however, it is speculated that it would either require a dangerously high voltage (at least one kilovolt) or a heavy conductor that can handle a lower voltage at a higher current. This heavier conductor would greatly stiffen the cables as well as reduce their fatigue life.

If the power requirements for the IPASS system can be reduced, power can feasibly be delivered through the cables, allowing for all day use of the system without the manual intervention of replacing batteries. Two primary avenues can be explored for reducing power consumption by the IPASS. The first is to reduce the power requirements of the system. This means reducing the inertia of the system, requiring less thrust of the motors. Additionally, ensuring that the system is well balanced and aerodynamically stable would reduce the power requirements of the system. The second avenue is to use higher efficiency motors and propellers. The motors and propellers used in the current prototype are hobbyist parts, and therefore have low efficiencies and tolerances. For further details on power requirement estimations, see Chapter 6.

The biggest design hurdle for developing the next IPASS prototype is to develop a system that can stabilize lateral disturbances. The current prototype attempted to stabilize these disturbances by using three angled propellers to create thrust vectors with lateral components to counteract lateral disturbances. The remaining three down-facing propellers would then generate moments to counteract the vertical thrust components of the angled motors, isolating lateral motion from rotational motion.

However, this system was shown, with the current control scheme and hardware, to not be able to achieve this task. From preliminary analysis, it appears that the two motions cannot be isolated due to the large translational inertia of the end-effector, as compared to its rotational inertia. This difference in inertia means that translational motion requires much more thrust than rotational motion. It is believed that the hardware in this prototype's drive system lacks the precision to stabilize rotation when generating the thrusts at the scale required by the lateral control. Improved control system and hardware may be able to generate thrusts at an adequate precision to make this system work; however, these initial experiments indicate a fundamental flaw in the IPASS design: the interdependence between all six inputs and the six degrees of freedom.

To overcome this fundamental design flaw, multiple new designs have been considered for the next prototype. The main motivation for a new design is the isolation of rotational stabilization from translations stabilization, due to the drastically different input required by the current design for the two processes. The primary design recommended by this analysis is to return to a four-rotor system on the sensor platform. This system could be used for rotational stabilization. The connection rod between the cable anchor plate and the sensor platform may then be actuated to generate translations stabilization.

Multiple methods of actuation would be available for the connection rod. Servo motors may be used to maintain a certain orientation of the upper gimbal. The primary downside to this method would be the lack of support provided for the reaction forces from the motors on the cable anchor plate. Actuating the motors would not only rotate the connection rod, but also the unrestrained cable anchor plate. One alternative provided by

this report is to use a secondary aeromotive system to actuate the rod. With as few as one propeller mounted to an active gimbal at the upper end of the rod, the rod may be sufficiently controllable to counteract wind and other disturbances. Alternatively, the angled motors on the sensor platform may be rotated to 90 degrees rather than 45 degrees. The thrust that they generate would be purely lateral and would not cause the end-effector to rotate.

Design recommendations mentioned thus far are conceptual and have not been tested for feasibility. Further design considerations to be kept in mind as development continues for upcoming prototypes include:

- The use of ducted propellers may provide a more consistent thrust vector, improved efficiency, and decreased vulnerability to debris
- Higher quality motors and propellers, in general, may produce more consistent thrust vectors at higher efficiencies
- Develop an active center-of-mass positioning system to maintain end-effector balance and reduce power requirements for the IPASS
- Computation speeds faster than 100 Hz may be required for the stabilization control loop
- A more complex controller than PD may be required to stabilize this system
- Investigate the dynamic model further, removing any further assumptions and take into account dynamic properties such as the Coriolis effect

CHAPTER 6. MOBILE PHENOTYPING SYSTEM

While the phenotyping system designed for Mead, Nebraska is anticipated to address the current needs of the agricultural researchers at the University of Nebraska, its use is limited to specific growing conditions and field setup. One aspect of this research was to determine the feasibility of a mobile system that could be used to monitor established, full-sized fields. This system would also allow for the study of fields in remote or unstable locations where permanent fixtures may not be possible. With a reduced infrastructure, it could also allow for a larger number of systems to be built at a more affordable cost and to be rapidly deployed in various fields. The analysis for this system is threefold: one, the feasibility of the mechanical design and its portability, two, the power requirements and routine maintenance of the system, and third, the cost analysis for a prototype system.

6.1 Tower Selection

The first aspect of this design was finding portable support structures around which the system could be built. The portable system would require portable towers that could be rapidly deployed. In addition, it would be preferred if the towers could have their cable winches mounted directly to them at all times to reduce setup time and complication. It would also aid to have storage space available at every tower to reduce run-around during setup as well as provide protection from the elements. As a result, several companies were reached out to who design custom, portable radio towers, as in Figures 6-1 and 6-2.

Figure 6-1. HEIGHTS Tower System. [51]

Figure 6-2. Aluma Tower System. [52]

The top contenders were Heights Tower System and Aluma Tower Company. Quotes were received from both of these companies for both open and enclosed trailers and are available in Appendix E. Based on these quotes, this analysis focuses on the use of enclosed Heights Tower System trailers. These trailers were selected because the enclosure provides environmental protection for the winch, allows for additional storage

space within the trailer, allows for limited office space for a technician, and allows for either a generator to be placed inside the trailer or solar panels to be mounted on its roof.

6.2 Winch Design

The next most important component is the winch to be used to feed the cable. In the beginning of this research project, it was intended that the engineering team would design the entire system at Mead. During the preliminary designs for the Mead system, a search was made to find a company to design the winches for that system. The best candidate found at that time was The DavidRound Compnay [53]. DavidRound is a manufacturer of custom winches, such as the one shown in Figure 6-3, for a wide range of applications. While the winches for the mobile system would have slightly different specifications from the original winches quoted, the original quotes (Appendix E) were used to estimate the cost of the winches for the mobile system. After evaluating the original quotes the following equation was chosen to estimate the cost of the winches.

Figure 6-3. Example DavidRound Winch. [53]

$$Cost = \$12{,}500 + \$27 * D * C + \$550 * HP \quad (6\text{-}1)$$

where D is the diameter of the cable (in inches), C is the capacity of the drum (in feet), and HP is the power required of the winch. The diameter of the cable and its length drive the overall size of the winch while the power requirements influenced the cost of the motor, brake, and other electrical components. This relationship is illustrated in Figure 6-4.

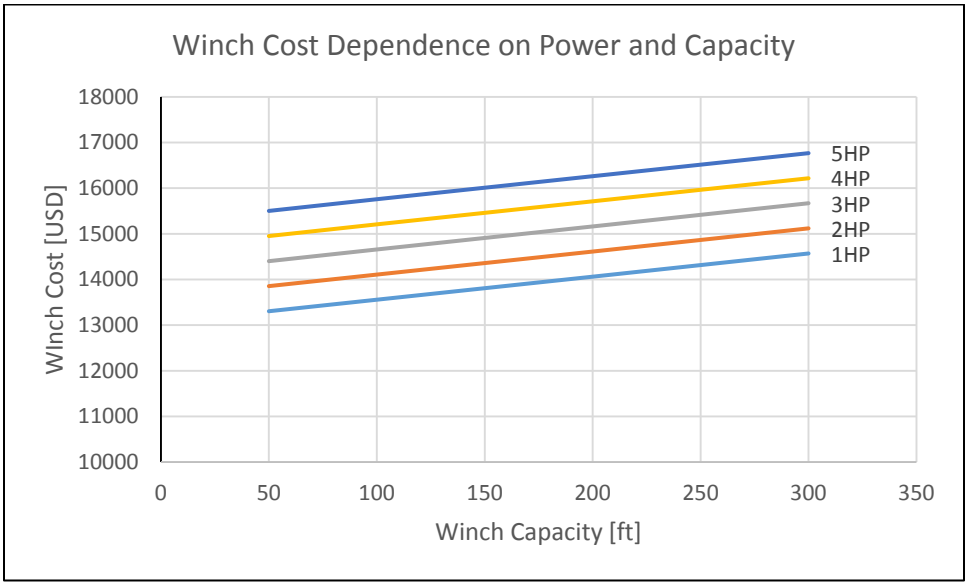

Figure 6-4. Winch cost dependence on power and capacity.

Because this design was still at the level of feasibility analysis, none of these parameters had been set. To determine these parameters, a static analysis of the system was performed using the methods presented in Chapter 2. The first step was to determine the predicted maximum tension on the cables as well as desired maximum cable speed so that the power requirements of the winches could be determined. As a basepoint, a few parameters needed to be defined. Those parameters are listed in Table 6-1 below.

Table 6-1. Mobile system predefined parameters.

Parameter	Value
Field Width	220 ft
Field Depth	220 ft
Cable	3/16” AMSTEEL-BLUE rope

During the preliminary design of the Mead system, the engineering team looked for a replacement rope for the high cost Kevlar cables with fiber optic cores that were used by Spidercam in Zurich. The cable chosen at that time was a dyneema-based 12-strand rope produced by Samson Rope Technologies. This cable is as strong as a steel cable of the same diameter while being one eighth the weight. It also exhibits “extremely low stretch, and superior flex fatigue and wear resistance” [54]. It also has high UV resistance, is chemically inert, is simple to splice, and is low cost [55].

The remaining unknowns to determine the maximum tension in the field are the weight of the end-effector and the minimum vertical distance between the end-effector and the cable-feed pulleys. Multiple simulations were run for a range of values for both parameters. The results of this analysis are presented in Table 6-2.

Table 6-2. Theoretical tension dependence on end-effector weight and pulley to end-effector height difference.

Tension [lb]		Pulley to End-effector Height [ft]			
		10	15	20	25
End-effector Weight [lb]	10	100	65	50	40
	20	160	105	80	65
	30	220	145	110	90
	40	280	185	140	115
	50	340	230	170	140

Based on these results a simplified model of the system was produced, as provided by (6-2).

$$Tension_{max} = \frac{60*W+400}{dH} \quad (6\text{-}2)$$

where W is the weight of the end-effector in pounds, and dH is the vertical distance between the end-effector and the cable-feed pulleys. This is further illustrated in Figure 6-5.

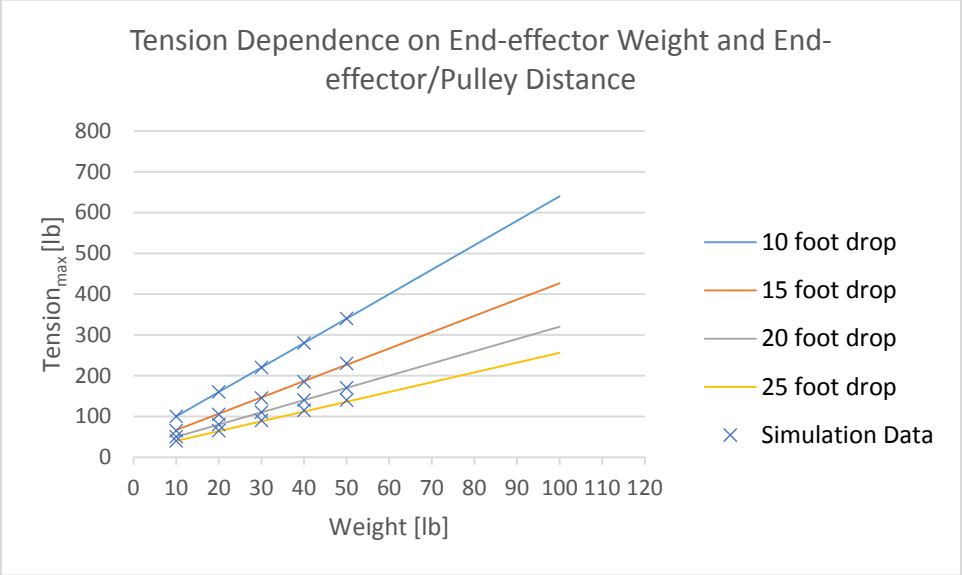

Figure 6-5. Tension dependence on end-effector weight and end-effector-to-pulley distance.

Given that the power to move an object is the product of the force acting on the object and its velocity:

$$HP_{max} = \frac{V_{max} * T_{max} * 550}{\eta} \tag{6-3}$$

where V is the cable federate in ft/sec, T is the tension in the cable and η is the efficiency of the winch. Based on this analysis, an iterative process was conducted, varying all of the model parameters listed in Table 6-3. Finally, a model was selected for the mobile system, as described by Table 6-3.

Table 6-3. Mobile system design parameters.

Parameter	Value
Tower Height	50 ft
Feed-pulley to End-effector Minimum Drop	20 ft
Tower Layout Width	220 ft
Tower Layout Depth	220 ft
Maximum Cable Speed	5 ft/sec
Cable Diameter	3/16 in
Winch Capacity	275 ft
Maximum End-effector Weight	85 lb
Maximum Cable Tension	275 lb
Winch Efficiency	70%
Winch Input Power	3.6 HP
Winch Cost	$16,200

During this analysis it was determined that the driving parameters were the height of the towers and the maximum cable tension. The towers quoted were originally designed for mounting radio antennas, dishes, and other sensors. As such, they were designed for a given lateral load due to wind; however, by supporting a cable system, they are subject to large, constant loads at all times. In addition, as the height of the towers increases, their stability and load they can handle decrease. Therefore, it was decided to limit tower heights to 50 ft while being designed to withstand 300 lb of lateral load.

6.3 Power System Design

Besides the design of the cable system, the most critical aspect to the feasibility of the mobile system is the supply and distribution of power. Extensive research was conducted into multiple means of power generation – including several generator and solar panel configurations – and distribution.

6.3a Single Generator System

With towers and winches quoted, the primary concern was how to power the system. As this system is intended for remote use, it must be capable of providing its own power. Additionally, it should be a low maintenance system that would not require a technician on site at all times or constant refueling. One option was to use a single generator located at one of the towers. By mounting a large generator and a fuel tank to a fifth trailer, power could be run to all four tower trailers from one localized source. One downside to this approach is that it would require the users to run long cables along three edges of the field to power the remote towers. While this would leave the fourth edge of the field open, it could still provide complications for the farmers.

6.3b Multi Generator System

The second option would be to use smaller generator and fuel tanks mounted to each of the winch trailers. This would mean that the system would require one less trailer to set up and every tower is completely isolated from each other (seeing as wireless communication between the towers has already been proven possible using the 12^{th}-scale system), allowing for simpler, more versatile setup. One downside to this method is that

it would require four generators and fuel tanks, increasing cost and space required in each trailer. Additionally, it would require a fuel truck to have access to all four corners of the field during refueling. This could prove troublesome and time-consuming in certain environments.

6.3c Transmitting Power through Cables

The third option considered was to use a single generator, but rather than running power cables along the ground around the perimeter of the field, pass power through the end-effector support cables. By doing so, the entire system can be powered from one easily-accessible location without interfering with the surrounding terrain or farming processes. The downside to this method is that the end-effector and three other winches would require large amounts of power. This means that either heavy gauge wires would have to pass through the support wires or power would have to pass at extremely high voltages to pass through higher gauge cables. Additionally, there are challenges in delivering power across the winch drum. The moving parts would require the power to be transmitted through a slip ring to connect to the constantly rotating drum. Additionally, the coiling of the rope about the drum would cause a constantly varying inductance in the line, presenting issues for power transmission through the system [56], [57]. As a result, it is assumed that power transmission would be required to be DC as it would be less affected by the variable inductance.

Based on preliminary experiments using short samples of $3/16^{th}$ inch dyneema rope, it was determined that 14 gauge wire with a thin coating was the largest wire that could comfortably fit through the center of the rope. However, to maintain flexibility and to

reduce cable weight and stiffness, it would be recommended not to use larger than 18 gauge. While the four winches should never simultaneously need to operate at maximum power, let's assume that, between the three remote winches and the power requirements of the end-effector, the cables must be able to support 8 kW of power at any time. Using 14 gauge wire and DC current, this would require power to be transmitted at a minimum of 2 kV to not burn out the estimated 120 meters of cable or experience a drop in voltage of greater than 2% [58].

Running the system at this voltage presents engineering and safety challenges that cause this path to be undesirable. However, it is still under consideration as a means for powering the end-effector. For this system to work, the end-effector must receive power by some means. While it could be powered by batteries, the batteries would take a large portion of the 85 lb limit set previously. Additionally, batteries would require constant oversight, likely needing to be swapped every day. To maintain an autonomous system with reduced oversight, the power can be generated at one of the trailers, scaled to a higher voltage, transmitted along one of the support cables, have the voltage be dropped down to a usable level on the end-effector, and then be grounded through a second cable. Running a quick search through Digikey's website, preliminary hardware has been found to perform this task, as illustrated by Figure 6-6. Based on [58], a 390V supply could be passed through a 14 gauge cable over the estimated span of 120 meters to supply a maximum of 1kW of power to the end-effector. Based on preliminary end-effector analysis, this should be a comfortable limit to meet.

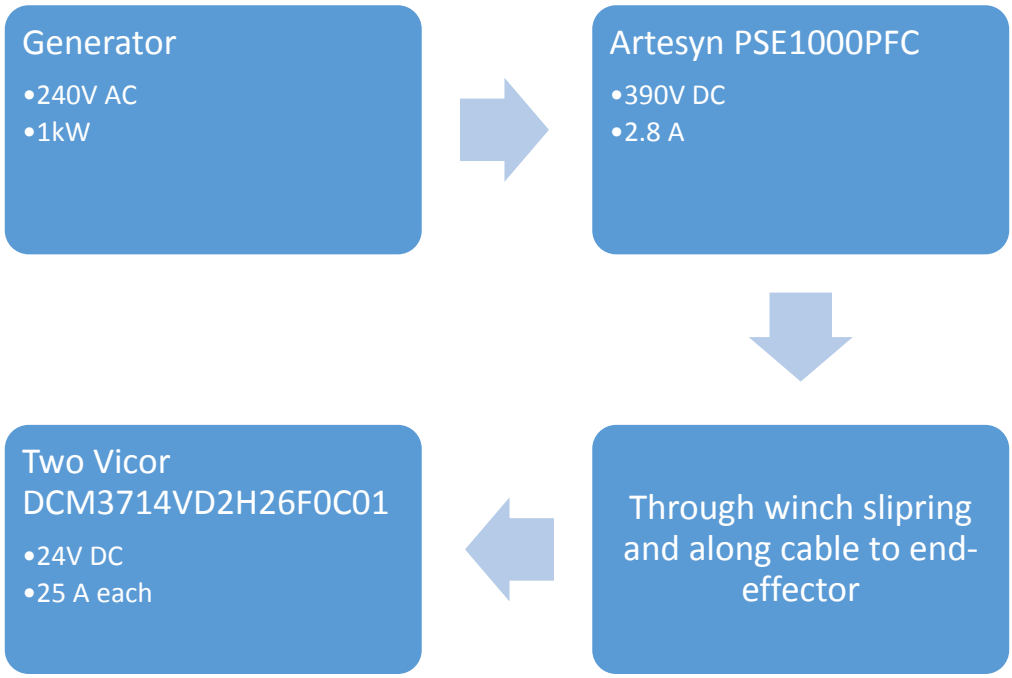

Figure 6-6. End-effector power flow. [59], [60]

The final method of powering the system investigated in this analysis was to use individual solar panels for each of the trailers. By doing this, each tower would be independent from each other, just like in the case of individual generators. In addition, it further automated the system as users would no longer need to routinely visit the site to refuel the system. The primary questions for solar power, however, is the cost and space requirements to generate and store enough power to operate one of the winches for an entire day. To resolve this, it must be determined how much power is required to scan the entire field.

6.3d System Power Requirements Estimation

During the scanning process, there are two modes that the system will behave in. One when it is traveling and the winches are drawing power and the other when it is scanning

and the sensors and stabilization system are drawing power. To solve the amount of power required to navigate the end-effector through its flight path for one scan, a field such as in Figure 6-7 is imagined.

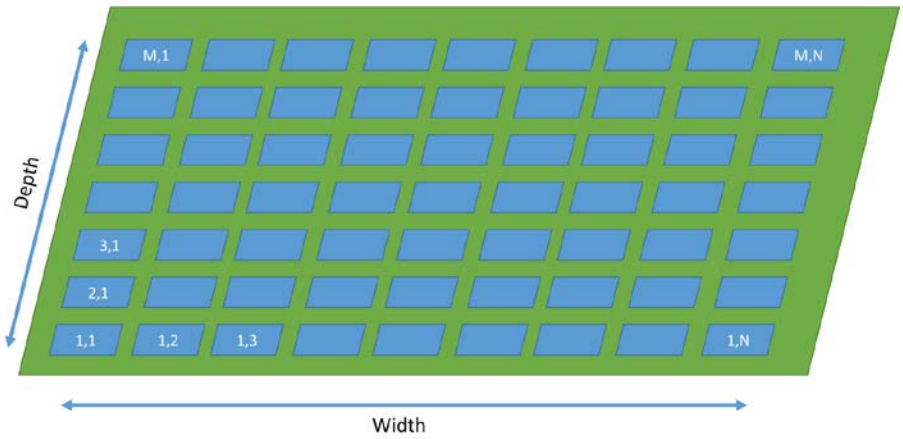

Figure 6-7. Mobile system plot layout.

Imagining a zig-zagging flight path through the field generates the following path.

$$plot_{1,1} \rightarrow plot_{1,N} \rightarrow plot_{2,N} \rightarrow plot_{2,1} \rightarrow plot_{3,1} \rightarrow plot_{3,N} \rightarrow \cdots \quad (6\text{-}4)$$

Taking the length of each of these vectors gives the total flight length:

$$Distance_{total} = D_{1,1:1,N} \rightarrow D_{1,N:2,N} \rightarrow D_{2,N:3,1} \rightarrow D_{2,1} \rightarrow D_{2,1:3,1} \rightarrow D_{3,1:3,N} \rightarrow \cdots \quad (6\text{-}5)$$

$$Distance_{total} = D_{1,1:1,N} + D_{1,N:2,N} + D_{2,N:3,1} + D_{2,1} + D_{2,1:3,1} + D_{3,1:3,N} \rightarrow \cdots \quad (6\text{-}6)$$

$$Distance_{total} = \left(Width - \frac{Width}{N}\right) + \frac{Depth}{M} + Width + \frac{Depth}{M} + \cdots \text{ [12]} \quad (6\text{-}7)$$

$$Distance_{total} = M * \left(Width - \frac{Width}{N}\right) + \left(Depth - \frac{Depth}{M}\right) \quad (6\text{-}8)$$

To simplify the analysis let's assume that the width and depth of the field are both equal to 220ft and that there is an equal number of rows as columns. In this case, (6-8) becomes:

$$Distance_{total} = N * Width - \frac{Width}{N} \quad (6\text{-}9)$$

It can also be determined at this point the amount of time required to perform each scan. This can indicate how many scans can be performed in a day as well as whether or not there would be an appreciable change in conditions during a single scanning operation, for example whether the position of the sun significantly changes. Additionally, it indicates the amount of time that the stabilization system and sensors will be drawing power during a scanning operation. Assuming the end-effector accelerates rapidly, the total time of travel for one scanning operation can be approximated by simply dividing the total distance traveled by the velocity of the end-effector. In addition to time spent traveling, each scanning operation requires a set amount of time to stabilize and scan each plot. This time can be estimated as some constant interval times the number of plots in the field, or the number of rows times the number of columns.

---

[12] The end effector does not travel to the edge of each plot as it moves along each row; it only moves to the center of each end plot. As a result, the width of half a plot must be subtracted from either end of the length of travel. The same applies for movement up the columns

$$Time_{total} = Time_{traveling} + Time_{scanning} \tag{6-10}$$

$$Time_{total} = \frac{N*Width-\frac{Width}{N}}{V_{max}} + Time_{scan} * N^2 \tag{6-11}$$

Taking the previously defined width and maximum end-effector speeds defined earlier (220 ft and 5 ft/sec respectively), this results in the times presented by Figure 6-8.

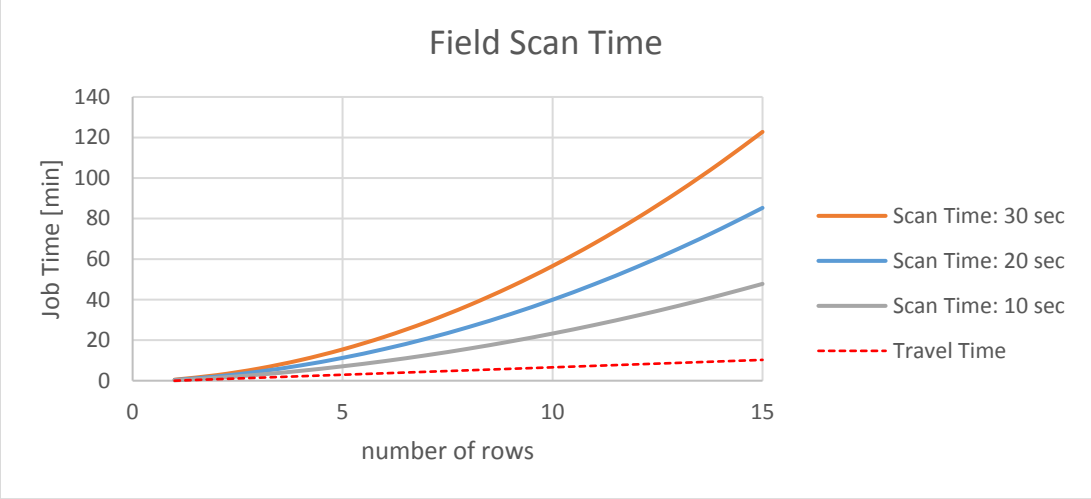

Figure 6-8. Mobile system field scan time.

Returning to solving the amount of power required to perform one scanning operation, the energy required to move the end-effector through the workspace can be approximated by taking the average cable tension throughout the workspace and multiplying it by the total distance the cable actuates during the operation. Unfortunately, the distance traveled by the end-effector is not the same as the distance traveled by each cable. The distance the end-effector moves is necessarily further than that of the cable as the end-effector does not move typically move along the axis of the cable. However, this distance is used as a conservative overestimate as this is a very preliminary feasibility calculation and

only requires a rough prediction. Therefore, it is approximated that the energy required to actuate a single cable through one scanning operation is the total distance it actuates times the average tension in the cable.

$$E_{winch} = Distance_{total} * T_{avg} \quad (6\text{-}12)$$

By running a static analysis of the designed system as in Chapter 2, it was determined that the average tension seen throughout the field is approximately 70lb. By combining this with the previously defined dimensions, the energy required to navigate the field is illustrated by Figure 6-9.

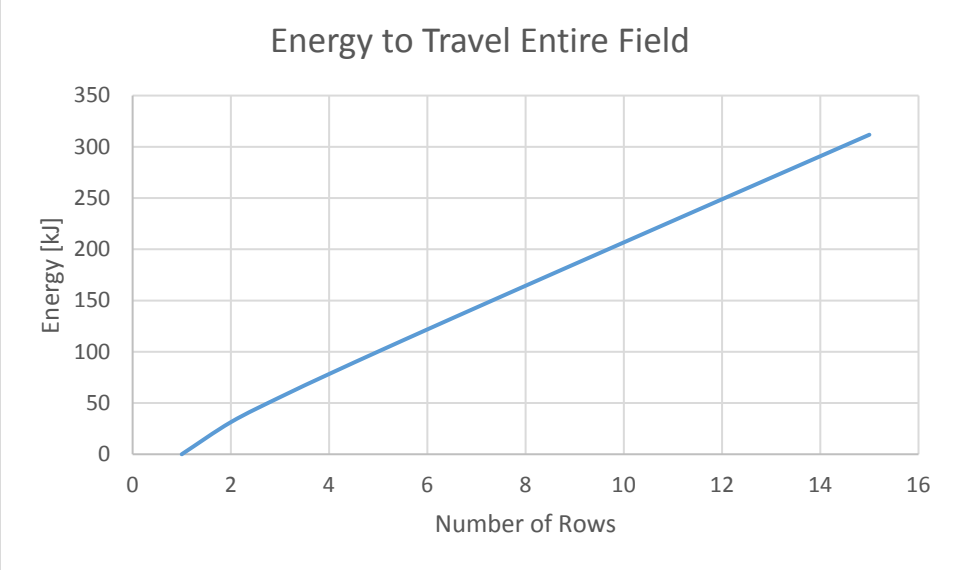

Figure 6-9. Estimated energy requirements to travel entire field.

The remaining power requirements of the system are tied to the sensor package and the stabilization system. It can be assumed that the stabilization system is only in use during scanning. Therefore, its power requirements can be taken as a function of the time to scan each plot and the number of plots in the field.

$$E_{stabilization} = C * Time_{scan} * N^2 \quad (6\text{-}13)$$

Assuming that the hardware changes described in Chapter 5 are implemented, the stabilization will be operated with six 115-Watt motors. Assuming that the stabilization system will run at a base throttle of 15% as it does with the current prototype, this means that the system will be running at an average of 103.5 Watts. Based on this model, the stabilization system energy requirements are illustrated in Figure 6-10.

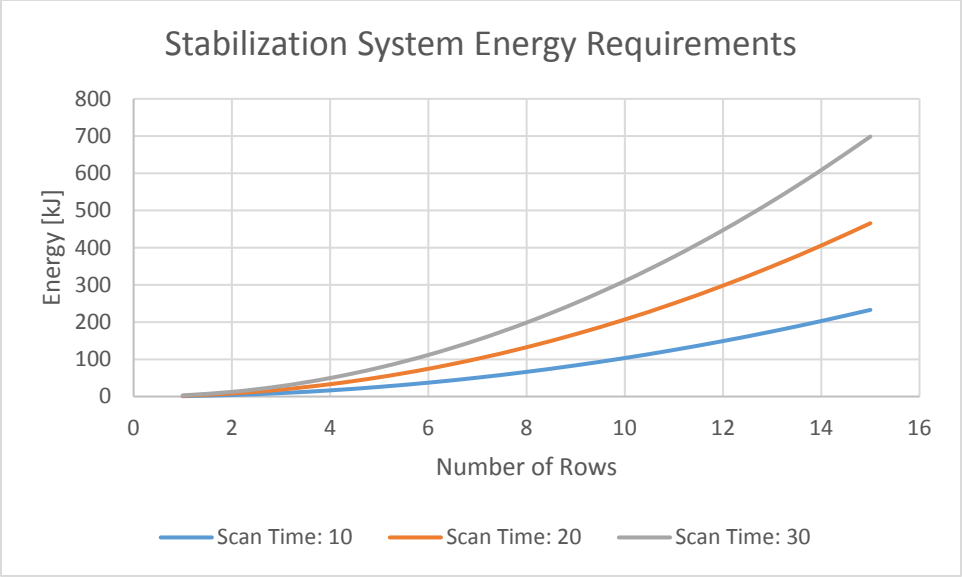

Figure 6-10. Estimated stabilization system energy requirements.

The last primary power requirement is that of the sensor platform and networking devices. For simplicity, it is assumed that 103.5 Watts is a conservative estimate for the amount of power required by the sensors, as well as the stabilization system. It can also be assumed that most of the sensors will perform in a low-energy mode when not scanning and can therefore be assumed to only require power during scanning. It

therefore follows an identical equation as (6-13) and can be estimated by Figure 6-10 as well.

Finally, the overall power draw for the system can be approximated by (6-14), as shown in Figure 6-11.

$$E_{total} = 4 * E_{winch} + E_{stabilization} + E_{Sensors} = 4 * E_{winch} + 2 * E_{stabilization} \quad (6\text{-}14)$$

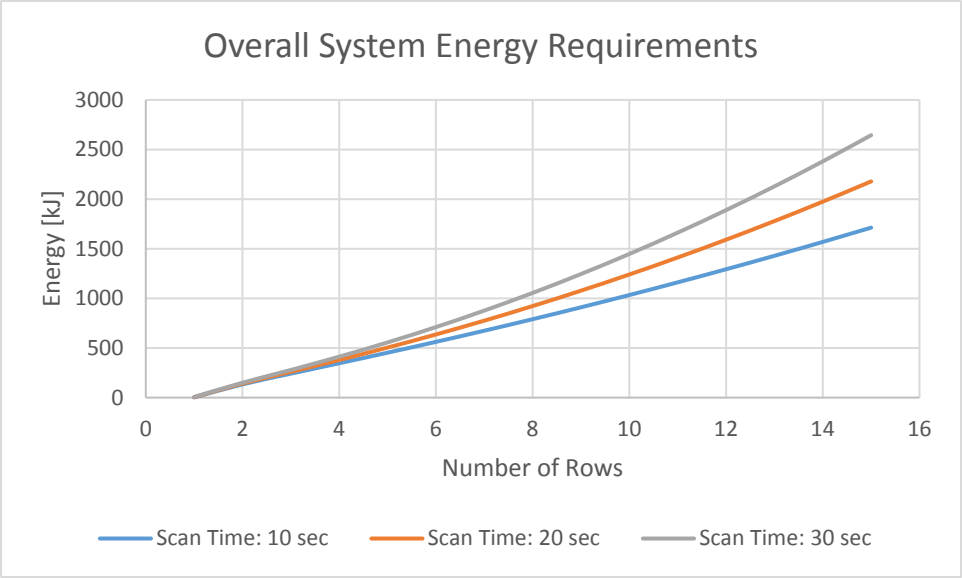

Figure 6-11. Estimated overall system energy requirements.

This represents the power requirements of a single power source. If individual power sources are used at each winch, then three of the sources will be used to power their own winch while the fourth will be used to power its winch, the stabilization system, and the sensor package. In that situation, the power requirements of the fourth source, shown in Figure 6-12, would be as follows.

$$E_{total} = E_{winch} + E_{stabilization} + E_{Sensors} = E_{winch} + 2 * E_{stabilization} \quad (6\text{-}15)$$

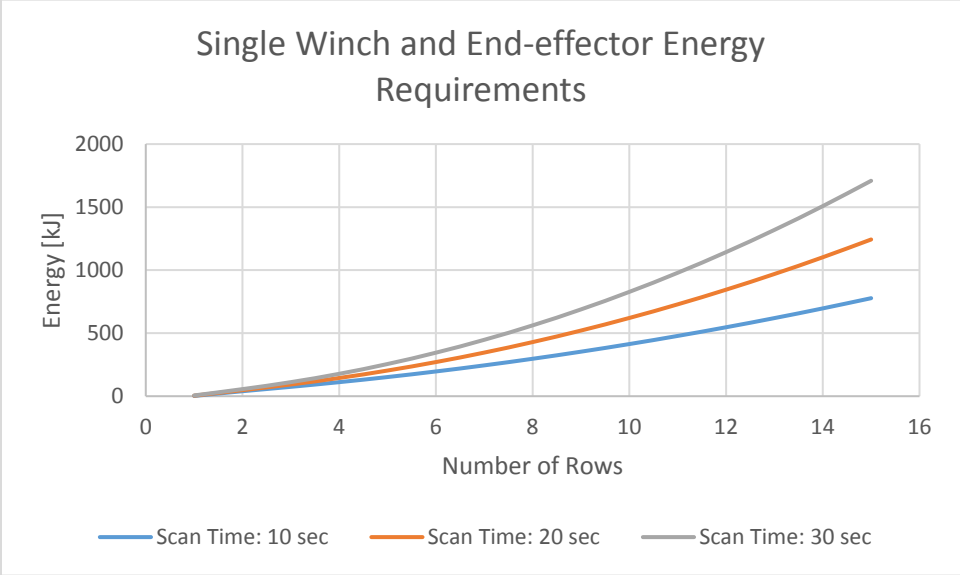

Figure 6-12. Single winch and end-effector energy requirements.

6.3e Solar Power Viability Analysis

A solar power system's ability to power this system is largely dependent on the availability of solar energy in the target area. Based on the resources made available by the US Department of Energy and illustrated in Figure 6-13, [61] the majority of Nebraska can expect an annual average of 440-520 Watt-hours per square foot per day. Provided that this system is intended to be used during summer months, when solar potential is at its highest, 440 Watt-hours per square foot per day should serve as a conservative estimate. Converting units, this becomes 144 kilojoules per square foot per day.

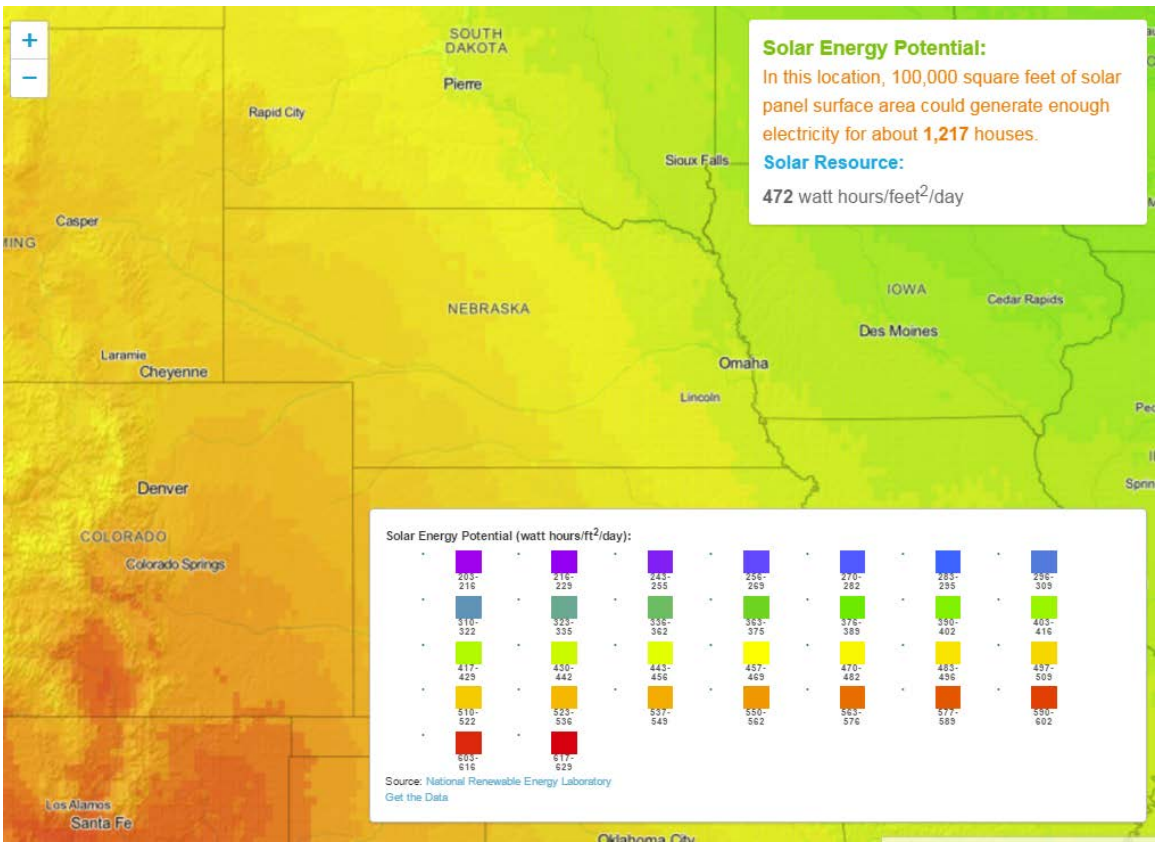

Figure 6-13. Solar Energy Potential Map. [61]

A wide range of solar panels are available through multiple distributors. This analysis assumes the use of Sunmodule Pro 345W XL Mono panels [62]. These panels are 3.3 feet wide and 6.5 feet tall with an efficiency of 17.3%. Assuming that they are to be mounted to the roofs of the enclosed trailers quoted in Appendix E, five panels can be used for each tower provided one panel hangs over the edge of the trailer a couple of inches. Based on these values, each trailer could provide 2672 kJ of power per day on average.

$$\frac{kJ}{day} = \frac{144\,kJ}{ft*ft*day} * \frac{3.3ft*6.5ft}{panel} * 5panels * 17.3\% = 2672\frac{kJ}{day} = 742\frac{Wh}{day} \quad (6\text{-}16)$$

This figure does not take into account several losses, such as panel misalignments, cloud cover, debris on the panels, obstructions – such as trees – or inclement weather. As far as weather conditions are concerned, this system is not designed to operate during harsh conditions. The remaining issues can be reduced by using experienced technicians during setup and regular maintenance.

Based on power requirement rough estimates, enough solar energy would be available to drive the winches for up to four, possibly six, complete scans of the field per day. The limitation would come from powering the end-effector systems as well as one winch from a single trailer. Should each plot only require ten seconds to scan, this system might be able to accommodate up to four scans a day; however, if scans required up to thirty seconds to complete, the system could only safely accommodate one scan per day. Multiple solutions could be implemented to improve the operation of the system. First, more efficient motors and/or a redesigned stabilization system could reduce the stabilization system's power requirements. Additionally, limiting the sensors used on the end-effector to low-power devices would further decrease the power requirements. Second, while trailer-mounted panels may be used to power the winches, a separate platform of panels could be set up to power the end-effector separate from the winch supplies. Finally, end-effector power requirements could be split between two winches rather than using only one. By running power to the end-effector through two cables and grounding the end-effector through the remaining two cables, not only is the load split between two sets of solar panels, but also, symmetry returns to the cable system, as now all four cables would have conductors running through them, giving them all the same physical properties.

Assuming that one of these paths is taken to make the solar system viable, the next issue is the storage of the power. A typical method of storing the power is to use a bank of batteries (similar to car batteries) to store the power. By wiring them in different configurations (number of batteries in parallel or in series), a user can achieve the desired voltage or current requirements. The bank chosen for this analysis is the Crown AGM 220 Ah 12 VDC 2.64 Wh battery bank [63]. While the previously selected solar panels are 24 volt panels, and this battery bank is sold as a pair of 12 volt batteries in parallel, they should be able to be switched to a series bank to achieve the required voltage. Each bank has a capacity of 2.6 kWh, meaning that one bank in each trailer could hold enough energy to power their respective winch for several days, in the case of continuous cloud coverage or inclement weather.

The last major component for a solar power system is an inverter to turn the 24VDC battery supply to a 240VAC supply for the winches and to be transmitted to the end-effector. While many are available, one arbitrary model is a 7kW unit sold by the Inverter Store [64]. All of the remaining expenses for the solar power system would be smaller, custom expenses, such as mountings for the solar panels, wiring, and slip rings for the winches and will not be evaluated further.

6.4 Conclusions

The first aspect of this feasibility analysis is the cost estimate, as laid out by Table 6-4. As it shows, the bulk of the cost is the towers and winches. However, these costs are for only four units of each for prototyping. Should this system become commercial, procurement costs for these parts should be expected to lower as a large portion of the

cost should currently be going towards engineering and not materials or manufacturing. The next largest cost is the solar power system. While the system would likely cost greater than $20,000 when everything is finished, the long-term savings could make it a viable power system. Overall, the estimated cost for a prototype system is $185,000. Provided that the current investment into the permanent system at Mead is in the realm of one million dollars, it is the opinion of this analysis that this system is fiscally feasible.

Table 6-4. Mobile system cost estimation.

Component	Cost per unit	Quantity	Total Cost
Towers	$22,500	4	$90,000
Winches	$16,200	4	$65,000
Solar panels	$320	20	$12,500
Battery Bank	$500	4	$2,000
Power Inverter	$1100	4	$4,500
Misc. Hardware/Fixtures	NA	NA	$4,000
Networking/ Computers	NA	NA	$4,000
End-effector	NA	NA	$3,000
Total			**$185,000**

From an engineering perspective, no challenges have been found to declare this system infeasible; however, there are certain concerns that will require further analysis should design progress. First, power generation and distribution will present challenges. While a

single generator presents the most simplistic and possibly cheapest option, it presents issues by requiring large cables to pass around the field, potentially impeding farming operations. Local generators and solar panels have their issues as well, as previously discussed, but the largest engineering challenge in the area of power management is the task of supplying the end-effector with power.

The second major engineering concern is developing a robust system that can be set up in rough or unstable terrain safely. This includes accounting for surrounding trees and vegetation and their impact on the system; soft, muddy soil and the potentially unstable grounding they offer for the trailers; wildlife and its interactions with the system; and protecting the system from the elements. This primarily would mean protecting winches and end-effector from the influences of nature and wildlife.

The final major engineering concern is simply a question of work required and should not impact the feasibility of the system. That concern is the question of designing a reliable, remote, autonomous robot that will behave as intended in harsh environments.

REFERENCES

[1] A. Walter, B. Studer, and R. Kölliker, “Advanced phenotyping offers opportunities for improved breeding of forage and turf species,” *Ann. Bot.*, vol. 110, no. 6, pp. 1271–1279, Nov. 2012.

[2] B. Parent *et al.*, “Combining field performance with controlled environment plant imaging to identify the genetic control of growth and transpiration underlying yield response to water-deficit stress in wheat,” *J. Exp. Bot.*, p. erv320, Jul. 2015.

[3] D. Chen *et al.*, “Dissecting the phenotypic components of crop plant growth and drought responses based on high-throughput image analysis,” *Plant Cell*, vol. 26, no. 12, pp. 4636–4655, Dec. 2014.

[4] D. Deery, J. Jimenez-Berni, H. Jones, X. Sirault, and R. Furbank, “Proximal Remote Sensing Buggies and Potential Applications for Field-Based Phenotyping,” *Agronomy*, vol. 4, no. 3, pp. 349–379, Jul. 2014.

[5] M. V. Boggess *et al.*, “The need for agriculture phenotyping: ‘moving from genotype to phenotype,’” *J. Proteomics*, vol. 93, pp. 20–39, Nov. 2013.

[6] L. GmbH, “Greenhouse Scanalyzer Systems,” *LemnaTec Phenomics since 1998*. [Online]. Available: http://www.lemnatec.com/products/greenhouse-scanalyzer-system/. [Accessed: 23-Jun-2017].

[7] L. GmbH, “Phenotyping systems to measure traits and plant development,” *LemnaTec Phenomics since 1998*. [Online]. Available: http://www.lemnatec.com/products/laboratory/lab-scanalyzer-ls30/. [Accessed: 23-Jun-2017].

[8] L. GmbH, “Field Phenotyping,” *LemnaTec Phenomics since 1998*. [Online]. Available: http://www.lemnatec.com/products/field-phenotyping/. [Accessed: 23-Jun-2017].

[9] D. Rundquist, A. Gitelson, B. Leavitt, A. Zygielbaum, R. Perk, and G. Keydan, “Elements of an Integrated Phenotyping System for Monitoring Crop Status at Canopy Level,” *Agronomy*, vol. 4, no. 1, pp. 108–123, Feb. 2014.

[10] S. Sankaran *et al.*, “Low-altitude, high-resolution aerial imaging systems for row and field crop phenotyping: A review,” *Eur. J. Agron.*, vol. 70, pp. 112–123, Oct. 2015.

[11] S. C. Chapman *et al.*, “Pheno-Copter: A Low-Altitude, Autonomous Remote-Sensing Robotic Helicopter for High-Throughput Field-Based Phenotyping,” *Agronomy*, vol. 4, no. 2, pp. 279–301, Jun. 2014.

[12] V. Duggal, M. Sukhwani, K. Bipin, G. S. Reddy, and K. M. Krishna, “Plantation monitoring and yield estimation using autonomous quadcopter for precision agriculture,” in *2016 IEEE International Conference on Robotics and Automation (ICRA)*, 2016, pp. 5121–5127.

[13] S. Kedari, P. Lohagaonkar, M. Nimbokar, G. Palve, and P. P. Yevale, “Quadcopter - A Smarter Way of Pesticide Spraying,” *Imp. J. Interdiscip. Res.*, vol. 2, no. 6, May 2016.

[14] M. Zaman-Allah *et al.*, “Unmanned aerial platform-based multi-spectral imaging for field phenotyping of maize,” *Plant Methods*, vol. 11, p. 35, 2015.

[15] “The Advantages Of Drone Remote Sensing For Agricultural Crops| Aerial Surveying & Mapping using Drones,” *SenSat | Aerial Surveying & Mapping using Drones*. [Online]. Available: https://www.sensat.co.uk/single-post/2015/07/25/The-Advantages-Of-Drone-Remote-Sensing-For-Agricultural-Crops. [Accessed: 23-Jun-2017].
[16] “Business Users | Know Before You Fly,” *Know Before You Fly*. .
[17] “Getting Started.” [Online]. Available: https://www.faa.gov/uas/getting_started/. [Accessed: 16-Jul-2017].
[18] J. Escareño, S. Salazar, H. Romero, and R. Lozano, “Trajectory Control of a Quadrotor Subject to 2D Wind Disturbances,” *J. Intell. Robot. Syst.*, vol. 70, no. 1–4, pp. 51–63, Apr. 2013.
[19] “Straight-line path following in windy conditions (PDF Download Available),” *ResearchGate*. [Online]. Available: https://www.researchgate.net/publication/265111551_Straight-line_path_following_in_windy_conditions. [Accessed: 29-Jun-2017].
[20] S. Waslander and C. Wang, “Wind Disturbance Estimation and Rejection for Quadrotor Position Control,” in *AIAA Infotech@Aerospace Conference*, American Institute of Aeronautics and Astronautics.
[21] westonmlewis, “Hercules,” *Advanced Aircraft Company*. .
[22] R. Nan *et al.*, “The Five-Hundred-Meter Aperture Spherical Radio Telescope (FAST) Project,” *Int. J. Mod. Phys. D*, vol. 20, no. 06, pp. 989–1024, Jun. 2011.
[23] D. NormileSep. 26, 2016, and 3:00 Pm, “World’s largest radio telescope will search for dark matter, listen for aliens,” *Science | AAAS*, 26-Sep-2016. [Online]. Available: http://www.sciencemag.org/news/2016/09/world-s-largest-radio-telescope-will-search-dark-matter-listen-aliens. [Accessed: 29-Jun-2017].
[24] S. Behzadipour and A. Khajepour, “Stiffness of Cable-based Parallel Manipulators With Application to Stability Analysis,” *J. Mech. Des.*, vol. 128, no. 1, pp. 303–310, Apr. 2005.
[25] N. Fabjan, “Spidercam - home,” *Spidercam*. [Online]. Available: http://www.Spidercam.tv/. [Accessed: 29-Jun-2017].
[26] M. Hiller, S. Fang, S. Mielczarek, R. Verhoeven, and D. Franitza, “Design, analysis and realization of tendon-based parallel manipulators,” *Mech. Mach. Theory*, vol. 40, no. 4, pp. 429–445, Apr. 2005.
[27] R. Yao, X. Tang, J. Wang, and P. Huang, “Dimensional Optimization Design of the Four-Cable-Driven Parallel Manipulator in FAST,” *IEEEASME Trans. Mechatron.*, vol. 15, no. 6, pp. 932–941, Dec. 2010.
[28] S. Kawamura, W. Choe, S. Tanaka, and S. R. Pandian, “Development of an ultrahigh speed robot FALCON using wire drive system,” in *, 1995 IEEE International Conference on Robotics and Automation, 1995. Proceedings*, 1995, vol. 1, pp. 215–220 vol.1.
[29] K. Maeda, S. Tadokoro, T. Takamori, M. Hiller, and R. Verhoeven, “On design of a redundant wire-driven parallel robot WARP manipulator,” in *1999 IEEE International Conference on Robotics and Automation, 1999. Proceedings*, 1999, vol. 2, pp. 895–900 vol.2.

[30] I. Ebert-Uphoff and P. A. Voglewede, “On the connections between cable-driven robots, parallel manipulators and grasping,” in *2004 IEEE International Conference on Robotics and Automation, 2004. Proceedings. ICRA ’04*, 2004, vol. 5, p. 4521–4526 Vol.5.
[31] B. Zi, B. Y. Duan, J. L. Du, and H. Bao, “Dynamic modeling and active control of a cable-suspended parallel robot,” *Mechatronics*, vol. 18, no. 1, pp. 1–12, Feb. 2008.
[32] S. Fang, D. Franitza, M. Torlo, F. Bekes, and M. Hiller, “Motion control of a tendon-based parallel manipulator using optimal tension distribution,” *IEEEASME Trans. Mechatron.*, vol. 9, no. 3, pp. 561–568, Sep. 2004.
[33] Y. Suilu, W. Zhao, L. Qi, and C. Yixin, “Stiffness analysis of a wire-driven parallel manipulator,” in *2012 IEEE International Conference on Computer Science and Automation Engineering (CSAE)*, 2012, vol. 3, pp. 31–34.
[34] M. Yamamoto, N. Yanai, and A. Mohri, “Trajectory control of incompletely restrained parallel-wire-suspended mechanism based on inverse dynamics,” *IEEE Trans. Robot.*, vol. 20, no. 5, pp. 840–850, Oct. 2004.
[35] L. Bin, L. Yinghui, and Y. Xuegang, “Dynamic modeling and simulation of flexible cable with large sag,” *Appl. Math. Mech.*, vol. 21, no. 6, pp. 707–714.
[36] K. Kozak, Q. Zhou, and J. Wang, “Static analysis of cable-driven manipulators with non-negligible cable mass,” *IEEE Trans. Robot.*, vol. 22, no. 3, pp. 425–433, Jun. 2006.
[37] J. C. Russell and T. J. Lardner, “Statics Experiments on an Elastic Catenary,” *J. Eng. Mech.*, vol. 123, no. 12, pp. 1322–1324, 1997.
[38] E. Costello, “Length of a Hanging Cable,” *Undergrad. J. Math. Model. One Two*, vol. 4, no. 1, Jan. 2011.
[39] G. P. Nikishkov, “Introduction to the Finite Element Method.” 19-Jan-2004.
[40] Z.-F. Shao, X. Tang, L.-P. Wang, and X. Chen, “Dynamic modeling and wind vibration control of the feed support system in FAST,” *Nonlinear Dyn.*, vol. 67, no. 2, pp. 965–985, Apr. 2011.
[41] “AeroQuad - The Open Source Quadcopter.” [Online]. Available: http://www.aeroquadstore.com/. [Accessed: 29-Jun-2017].
[42] “Adafruit 9-DOF Absolute Orientation IMU Fusion Breakout - BNO055 ID: 2472 - $34.95 : Adafruit Industries, Unique & fun DIY electronics and kits.” [Online]. Available: https://www.adafruit.com/product/2472. [Accessed: 30-Jun-2017].
[43] P. Schopp, L. Klingbeil, C. Peters, A. Buhmann, and Y. Manoli, “Sensor Fusion Algorithm and Calibration for a Gyroscope-free IMU,” *Procedia Chem.*, vol. 1, no. 1, pp. 1323–1326, Sep. 2009.
[44] F. Caron, E. Duflos, D. Pomorski, and P. Vanheeghe, “GPS/IMU data fusion using multisensor Kalman filtering: introduction of contextual aspects,” *Inf. Fusion*, vol. 7, no. 2, pp. 221–230, Jun. 2006.
[45] G. Girard, S. Côté, S. Zlatanova, Y. Barette, J. St-Pierre, and P. Van Oosterom, “Indoor Pedestrian Navigation Using Foot-Mounted IMU and Portable Ultrasound Range Sensors,” *Sensors*, vol. 11, no. 8, pp. 7606–7624, Aug. 2011.
[46] “FLYFUN 30A,” *HOBBYWING North America*. [Online]. Available: https://www.hobbywingdirect.com/products/flyfun-30a. [Accessed: 30-Jun-2017].
[47] “Servo control,” *Wikipedia*. 11-Apr-2017.

[48] “APC Propellers.” [Online]. Available: https://www.apcprop.com/v/PERFILES_WEB/listDatafiles.asp. [Accessed: 30-Jun-2017].
[49] “BPH - Cheetah A2217-9 Brushless Outrunner Motor.” [Online]. Available: http://www.bphobbies.com/view.asp?id=v450327&pid=b2632605. [Accessed: 30-Jun-2017].
[50] “Brushless motor calculation,” *OpenROV Forums*. [Online]. Available: https://forum.openrov.com/t/brushless-motor-calculation/613. [Accessed: 30-Jun-2017].
[51] D. Dimitry, “Portable/COWS,” *HEIGHTS Tower Systems*. [Online]. Available: http://heightstowers.com/portable-cows.html. [Accessed: 17-Jun-2017].
[52] “Self Supporting Tower: Open Trailer Towers: TM 53-70,” *Aluma Tower Company*. [Online]. Available: http://www.alumatower.com/wp-content/gallery/tm-53-70/scorpion_14.jpg. [Accessed: 17-Jun-2017].
[53] “Industrial Winches - Air & Electric Models | 202 Series Winch by David Round,” *David Round*. .
[54] “AMSTEEL-BLUE,” *Samson Rope*. [Online]. Available: http://samsonrope.com/Pages/Product.aspx?ProductID=872. [Accessed: 30-Jun-2017].
[55] “Dyneema-Comprehensive-factsheet-UHMWPE.pdf.” 01-Jan-2008.
[56] X. Nan and C. R. Sullivan, “An Improved Calculation of Proximity-Effect Loss in High-Frequency Windings of Round Conductors,” presented at the IEEE Power Electronics Specialists Conference, 2003.
[57] “Proximity effect (electromagnetism),” *Wikipedia*. 06-May-2017.
[58] “DC Cable Sizing Tool - Wire Size Calculator - MM2 & AWG - solar-wind.co.uk.” [Online]. Available: http://www.solar-wind.co.uk/cable-sizing-DC-cables.html. [Accessed: 17-Jun-2017].
[59] “DCM3714VD2H26F0C01 Vicor Corporation | Power Supplies - External/Internal (Off-Board) | DigiKey,” *Digikey*. [Online]. Available: https://www.digikey.com/product-detail/en/vicor-corporation/DCM3714VD2H26F0C01/1102-5480-ND/5629117. [Accessed: 17-Jun-2017].
[60] “PSE1000PFC Artesyn Embedded Technologies | Power Supplies - Board Mount | DigiKey,” *Digikey*. [Online]. Available: https://www.digikey.com/product-detail/en/artesyn-embedded-technologies/PSE1000PFC/PSE1000PFC-ND/4474923. [Accessed: 17-Jun-2017].
[61] “Solar Energy Potential,” *Energy.gov*. [Online]. Available: https://energy.gov/maps/solar-energy-potential. [Accessed: 18-Jun-2017].
[62] “SolarWorld Sunmodule Pro 345W XL Mono 33mm Frame | 345W Solar Panel,” *SolarPanelStore*. [Online]. Available: http://www.solarpanelstore.com/solar-power/large-solarpanels/solarworld_sw/sw-345-mono.html?_vsrefdom=adwords&gclid=Cj0KEQjwyZjKBRDu--WG9ayT_ZEBEiQApZBFuENLBrvFIMd5eEntCqADQrG3HjNREOOTyq8xjMULiVcaAiDb8P8HAQ. [Accessed: 18-Jun-2017].

[63] “Crown AGM 220 Ah 12 VDC 2,640 Wh (2) Battery Bank - Wholesale Solar,” *WholesaleSolar.com*. [Online]. Available: https://www.wholesalesolar.com/1898750/crown/battery-banks/crown-agm-220-ah-12-vdc-2-640-wh-2-battery-bank. [Accessed: 18-Jun-2017].

[64] “7000 Watt Power Inverter 24Vdc to 240Vac 50/60 Hz Industrial Grade by AIMS,” *The Inverter Store*. [Online]. Available: http://www.theinverterstore.com/7000-watt-heavy-duty-power-inverter-240vac-24-volt.html. [Accessed: 18-Jun-2017].

APPENDIX A. Cable-System Simulator

The cable-system simulator was implemented using a MATLAB script. The script was written to be modified and saved as separate functions for individual CDPR designs. For example, the template file was copied, modified, and renamed into three primary MATLAB functions for this research: one for the Mead system, one for the one-twelfth-scale system, and one for the mobile system. The only modification required to match the template to a model is to set the following five system parameters in the program heading.

- Width and depth between towers [ft]
- Tower Heights [ft]
- Weight of the end-effector [lbf]
- Mass of the cables [slug/ft]
- Gravitational constant [ft/sec^2]
- End-effector dimensions [ft]

The internal variables required by the numerical solvers are nondimensionalized and require no modification. End-effector dimensions refers to the Cartesian coordinates of each cable attachment point on the end-effector with respect to the end-effectors coordinate system centered around its center of mass.

To use the function, the user then simply inputs the end-effector coordinates to be analyzed and whether or not MATLAB should generate a figure illustrating the cable

layout. For example, assume that the template is saved as function “SampleAnalysis.” The user then populates the header file with the parameters in Table A-1.

Table A-1. Sample analysis simulator parameters.

Parameter	Value				Unit
Tower_layout	260		260		Ft
Tower_height	50	50	50	50	Ft
Weight_endeffector	30				Lbf
Weight_cable	0.0007				Slug/ft
g	32.2				Ft/sec^2
PayloadDims	-0.5	0.5	0		Ft
	0.5	0.5	0		
	-0.5	-0.5	0		
	0.5	-0.5	0		

The user may then call the function, inputting any position within the 260x260x50 ft envelope. For example, calling

SampleAnalysis(20,130,20,true);

will create a 3d image, illustrated by Figure A-1 below, and will output the following parameters:

- The input coordinates [ft]

- The predicted tension in each cable [lbf]
- The length of each cable, considering sag [ft]
- The inclination angle (ψ_n in Figure 2-1) and heading (θ_n in Figure 2-2) for each cable
- The cable profile parameters, as defined by (A-1)
- The end-effector orientation, including roll, pitch and yaw angles as well as the Cartesian coordinates of the cable attachment points with respect to the end-effector center-of-mass

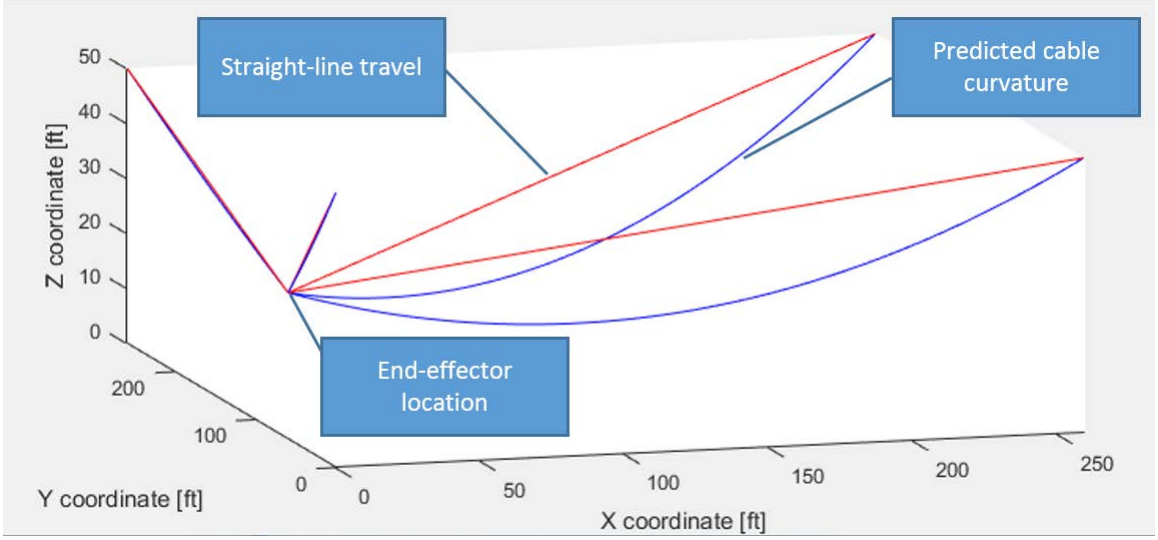

Figure A-1. Sample simulator output

$$y = y_0 + A * \cosh\frac{x_0 + x}{A} \quad \text{(A-1)}$$

As shown by Figure A-1, if the user decides to output the system image, it plots a 3d model of the field with two sets of lines. The red lines represent the straight-line vectors between the cable-feed points to the end-effector. The blue lines represent the sagging profiles of the cables.

The sample script is available at:

https://app.box.com/s/yfpxb8hyf1hru3wm1hjzl6y7zi0fzwmd

APPENDIX B. Cable-System Control Software

This Appendix contains expanded information to aid in the understanding of the contents of Chapter 3 as well as to aid in the deployment and modification of the CDPR system built by the author. It is assumed that Chapter 3 has been previously read by the reader.

The software to control the CDPR is built around two separate Arduino sketches. The first is installed on an Arduino pro mini and is used to control each winch. The second sketch is installed on an Arduino mega and is used to control the entire system. To use these sketches, the following libraries must be installed on the selected computer.

- EEPROM – built-in
- SPI – built-in
- Encoder – by Paul Stoffregen
- RF24 – by TMRh20

Using Arduino 1.6.9 or later, missing libraries may be installed by going to "Sketch → Include Library → Manage Libraries…".

The control logic runs as follows. The Arduino mega processes user inputs, calculates end-effector position and determines the desired speed for each winch. When calculations are complete, it transmits a data string that is received by all of the other system microcontrollers and changes its transceiver from transition to reception mode if it expects feedback from one of the other devices. The first part of this string indicates which microcontroller is the intended target. If the device matches the string, it processes the rest of the string. During normal operation, the remainder of the string is a direction

and speed for the winch to actuate. The microcontroller than sends a transmission back to the mega relaying the length of the cable based on encoder feedback from the winch's motor. The winch then takes the desired speed it received and passes it through a first order filter to prevent rapid acceleration of the cable and the induction of cable vibrations. After the mega receives feedback from the first winch (or a timer runs out) it transmits a similar strings to the remaining winches and the process repeats itself. In the case of lost communication between the controller and any of the winches, the disconnected winch comes to an immediate halt, while the controller transmits an emergency stop command to the remaining winches. As soon as communication is reestablished, the system returns to Manual Control mode.

In the case of power loss, the system may utilize the Arduinos' built-in EEPROM systems to constantly store the current length of the cables and system settings. The winch microcontrollers use the EEPROM to store the damping constant for the first-order velocity filter. The controller uses its EEPROM to store multiple parameters, such as the maximum winch speed and the acceleration and deceleration ranges for automated navigation. These settings may be altered using serial inputs to the controller from a PC.

The provided code is also designed to operate the original IPASS prototype. As that prototype has been dismantled and is not intended to be used again, its portion of the system code is excluded from this appendix.

The scripts to run the CDPR is available at:

https://app.box.com/s/zarmn98ftuve1dyp8lym79fm5quuvbov

The following is the pseudo-code for the system controller. It is intended only to aid in the understanding of the workflow for the code as it is being read.

```
 #include <EEPROM.h>
#include <SPI.h>
#include <RF24.h>

//declare RF radio. define pins for non SPI connections
RF24 radio(49, 53);
const uint64_t pipes[2] = {0xF0F0F0F001, 0xF0F0F0F003};

//define system global parameters and dimensions

//setup pin declarations

void setup() {
  //declare pin modes

  //begin serial communication

  //configure RF transceiver

  if(EEPROM_is_set){
    downloadEEPROMsettings();
  }else{
    configureEEPROM();
  }
}

void loop() {
  //update system timers

  //analyze user inputs (switches and joysticks) and determine system state
  ReadJoys();

  //calculate end-effector position based on current cable lengths
  FindPosition();

  //operations state machine
  //NOTE: Copter control mode neglected from the appendix analysis
  swtich(Winch_control_mode){
       case 1: //Joysticks manually control individual winches.
         //map joystick values to cable speeds and transmit
         ManualWinch();
```

```
      case 2: //Joysticks control end-effector velocity vector.
        //map joystick values to end-effector speed and transmit
        ManualControl();
      case 3: //Serial input defines destination.
        //compare current position to target position from serial input
        //and use to set target velocity
        PositionControl();
      Default: //Winches are off, controller is checking for serial input
        //send dummy message to ensure winches are stopped
        WinchStandby();
        //check for input from PC. if input is a destination, set State 3
        CheckInput();
  }
  //Check communication with winches
  //delay to maintain continuous loop speed

}
```

The following is the pseudo-code for the system winches. It is intended only to aid in the understanding of the workflow for the code as it is being read.

```
#include <EEPROM.h>
#include <SPI.h>
#include <Encoder.h>
#include <RF24.h>

//declare RF radio. define pins for non SPI connections
RF24 radio(A0, 10);

const uint64_t pipes[2] = {0xF0F0F0F001, 0xF0F0F0F003};

//define system global parameters and dimensions

//setup pin declarations

void setup(){
  //declare pin modes

  //begin serial communication

  //configure RF transceiver

  //use swtiches on sides of winch to identify winch

  if(EEPROM_is_set){
    downloadEEPROMsettings();
  }else{
    configureEEPROM();
  }
}

void loop(){
  //update system timers

  //read encoder and update cable length

  switch (State){
    case 1: //normal operation
      //check for radio input and transmit feedback
      Rx_input_Tx_Length();
      //update the speed of the winch
      writeSpeed();
```

```
    default://no connection
      //try to establish radio connection
      setupConnection();
  }
  //check for communicaton loss
}
```

APPENDIX C. Experimental Videographic Data Repository

The bulk of the experimental data from this research were videographic. A repository for most of these videos is available at:

https://app.box.com/s/29wr213tw1xi0jyarpuqvnejj27tf45i

APPENDIX D. Aeromotive Control Software

To allow for the conversion of the aeromotive system to a non-Arduino based system, as well as to simplify the creation of certain required libraries, the aeromotive flight controller code was written in C rather than in Arduino's syntax. The peripheral MCU and controller MCU were both modified from the code used in the proof-of-concept system. As such, they were left in their original Arduino syntax. What follows is a breakdown of the code used on these three devices. The code may be found in the following repository.

https://app.box.com/s/uzcx1kq6d4uz9wiplkit59lhs7b3hur0

While Atmel Studio 7.0 was used to develop the code, any C-based microcontroller suite should be capable of using and modifying this code. The code is compiled from seven different files.

- Main.c: This is the main .c file of the system. It includes #include statements for UserConfiguration.h and AeromotiveControllerV0.1.0.h. It houses the SETUP() and main() functions.
- TimingandSetup.c: This file contains functions for initializing MCU settings, communication with IMUs and the peripheral MCU, and timers.
- SensorsandInputs.c: This file contains functions for reading sensors (IMUs) and communication routines. It also houses processCommands(), which is used to implement user-input commands.

- FlightControlProcessor.c: This function houses all of the functions for performing flight-control operations, including interpreting IMU inputs, running the PD control loop, and setting the motor speeds.
- AeromotiveControllerV0.1.0.h: This file includes all of the libraries, sets the clock speed and baudrate, contains macros for quicker coding, defines several registers, defines structures, and defines most of the shared functions.
- UserConfiguration.h: This file defines pinouts, PID values, system model properties, drive system properties, and motor limits.
- LocalVariablesandMacros.h: This file creates all of the local variables based on the predefined structures. It also defines the model matrix A, as described in Chapter 5.4b as well as the conversion from thrust to throttle, as described in the same section.

Additionally, the code uses several libraries that are not built into Atmel Studio 7.0. All of these libraries were written or else modified from an open-library for use in this project.

- BNO055.h: This library contains functions for interacting with the system IMU's. It communicates over I^2C and can communicate with up to two IMUs.
- Uart.h: This is a modified uart library used to communicate between the two Arduinos.
- I2cmaster.h: This is a modified I^2C library used to communicate with the IMUs.

- Timer0.h: This is a custom timer library (for functions millis() for example) that runs off of timer0 on the Arduino.

The system is designed to take input from the same controller as was used for the one-twelfth-scale CDPR. Before the system starts, it must establish connection with both IMUs and the peripheral controller. On loss of communication with the peripheral controller or the user controller, the drive system is disabled.

The following is the pseudo-code for the IPASS system as it stands. <<file_name.c>> is used to indicate changes between .c files.

<<main.c>>

```
#include "UserConfiguration.h"
#include "AeromotiveControllerV0.1.0.h"
//define global registers and state variable.
volatile uint8_t flightStatus = 0b00000000; //contains flags indicating the current state of operation
volatile uint8_t timerStatus = 0b00000000; // contains flags to indicate whether it is time for certain actions to occur
volatile uint8_t state = 0; //used to control the state machine

void SETUP() {
    InitializeIO(); //initialize timer. Set state led
    InitializePWM(); // set pwm settings for ESCs
    InitializeMotors(); // currently nothing
        InitializeCOMMS(); // initialize UART communication over usb port (output for diagnostics) and check connection with peripheral MCU over uart1
```

```
        InitializeSensors(); //begin I2C and check connection with both IMUs
        //initialize clock and state
        Clock->previousTime = millis();
        state = standby;
}
Int main(){
        #include "LocalVariablesandMacros.h"
        SETUP();
        //CFS# indicates ‘clear flight status register #’
        //RFS# indicates ‘read flight status register #’
        //SFS# indicates ‘set flight status register #’
        CFSenable;//set flight status register: enable system
        CFSattitude;//set rate mode
        CFSpilot;//set to stabilize level
        SFSthrottle1;//set default throttle to given base value
//begin continuous loop
        while (1) {
                updateTimers(&Clock);//update timer. Flip timer flags if required time has
                passes
                if(RFSenable && RFSattitude){// if flightstatus flag and attitude move
                flag are active, set state for attitude mode.
                        state = attitudeMode;
                }else if(RFSenable){//otherwise, set state to rate control.
                        state = rateMode;
                }else{// if flight system is flagged as disable, switch state to standby
```

```
            state = standby;
        }
        //State machine
        switch(state) {
            case standby :
                if(RTST100){//perform these tasks 100 times per second,
                based on Timer status register flags
                    //set throttle to zero and stop motors
                    //measure sensors
                    //check for inputs
                }
            case rateMode :
                if(RTST100){
                    measureCriticalSensors();
                    flightCalculations();
                    checkInput();
                }
            Case attitudeMode :
                if(RTST100){
                    measureCriticalSensors();
                    flightCalculations();
                    checkInput();
                }
        }
    //clear flags and restart infinite loop.
```

```
}

<<FlightControlProcessor.c>>

Void flightClaculations(){

        struct _frame PIDoutput; //establish structure to house this loop's PID values

        updatePID(IMU_feedback, PID settings); //take IMU data and pass it through PID
        controller to obtain desired acceleration values

        calculateThrottle(desired_acceleration_values); //use end-effector model to
        determine required thrust values. Convert said thrust values to throttle values.

        Motors_PWM(); //write said throttle values to motors.

}
```

APPENDIX E. Mobile System Support Documentation

For a 42 ft. tower, rated for 12 sq. Ft. in winds of 80 mph, mounted on a Fold Over Kit & trailer.

Overall height of tower on Stand and trailer is approx 48 ft., not including mast, which will add more height.

Retracted length of tower is 18 ft. Overall length of trailer is approx. 16 ft, not incl. tower.

Supervisor	Est. Ship Time	FOB	SHIP VIA	Terms
DD	20+ Weeks ARO	Pensacola, FL	Van Truck	1/2 down; 1/2 complt.

LINE	QTY	PRODUCT I.D.	DESCRIPTION	UNIT PRICE	TOTAL
1	4	CUA42 12sf@80mph	CUA42 (12 sq. ft.) Telescoping Aluminum Tower, consisting of:	3,901.00	15,604.00
	2	AC22-172	Aluminum Center Section - 8 ft. length		
	2	AC18-131	Aluminum Center Section - 8 ft. length		
	2	AC14-100	Aluminum Center Section - 8 ft. length		
2	4	Flat HBT22-225	Flat Hinge Base, 22-225	342.00	1,368.00
3	4	7' Stand 22-225	Seven Foot Stand, 22-225, for Fold Over Kit	1,130.00	4,520.00
4	4	FOK22-172/225	Fold Over Kit, 22-225/172, all aluminum	1,055.00	4,220.00
5	4	Screw Sys 1.0"	Screw Actuator System, 1.0" dia., for Fold Over Kit	339.00	1,356.00
6	0	Pre-wired GM	Pre-wired Gearmotor Kit, OPTIONAL	1,101.00	-
7	4	TS18-131	Top Shelf, 18-131 drilled for customer bearing	No Charge	-
8	4	RS18-131	Rotor Shelf, 18-131, drilled for customer rotor	97.00	388.00
9	4	GS-065	Yaesu Thrust Bearing, GS-065, up to 2.66" OD mast capacity	62.66	250.64
10	4	Brake System	Safety Brake System, to take load off of winch	485.00	1,940.00
11	4	Alum Mast	Aluminum Mast, 2.0" OD x 0.25" wall x 12 ft. length	84.00	336.00
12	0	CoAX Arm	CoAxial Cable Stand-off arms	39.00	-
13	4	Manual Winch	Manual Hand Crank Winch	No Charge	-
14	4	Enclosed Trailer	Enclosed Trailer, 16 ft. long x 7 ft. wide x 6 ft. tall inside height,	14,897.00	59,588.00
			double axle. Tower tabilizer bar; Four (4) outrigger legs; Electric		
			brake; Front tongue jack.; Trailer is made of steel, aluminum		
			& other materials.		
		Open Trailer,	Open Trailer, 16 ft. long x 6 ft. wide, double axle. Tower	16,700.00	
			*Trailer is per manufacturer's specification. If customer		
			needs special items, please specify so price can be modified.		
			*Quote does not include shipping.		

Thank you for the opportunity to quote your tower project.

Please let us know if you have any questions.

Subtotal	$ 89,570.64
Sales Tax	n/a
Total	**$ 89,570.64**

E-1 Heights Tower Quote

Quote No.	Date	Cust No	Terms	Estimated Delivery	F.O.B.	Expiration
1602367	12/7/2016	UNI003	1/2D, BBS	8-10 WEEKS ARO	ORIGIN	60 DAYS

Item	QTY	Part	Description	Price $	Extension $
002	1	900574	SHELTER TRAILER TOWER (S6/T-50XXH), GALVANIZED STEEL CHASSIS WITH ALL ALUMINUM SHELTER, 6'4"W X 21'4"L FRAME, 6'4" W X5'L X 7' H SHELTER,A-FRAME/T-BAR TONGUE, DUAL5,200LB GALVANIZED TORSIONAXLES (GVWR 10,390LBS) WITH ELECTRIC BRAKES, ST225/75R15_RADIAL TIRES, GALVANIZEDWHEELS, ALUMINUM FENDERS,6-HOLE COUPLER CHANNEL WITH2-5/16 BALL COUPLER, 5,000LB ZINC TONGUE JACK, AND ALUMINUM_ TREADBRITE DECKING. SHELTERFEATURES WELDED AND 3MADHESIVE CONSTRUCTION, WHITEAUTOMOTIVE GRADE PAINT, R-18 TRIPLE INSULATION, 3 POINT_MILITARY LOCKING DOOR LATCHSYSTEM, 120VAC BASIC ELECTRICSYSTEM, ALUMA LOGO ANDPINSTRIPE, INTERIOR FRP PANELING WITH ANODIZED_ALUMINUM TRIM, ANDALUMINUM TREADBRITE FLOOR.CONTAINS (4) SLIDEOUTOUTRIGGERS, 2 MIDDLE & 2 REAR CHASSIS JACK MOUNTS, AND (8)_8,000LB LEVELING JACKS W/ 9FOOT PLATES. INCLUDES LED DOTLIGHTING, BREAKAWAY KIT, 7 PINRV TYPE TRAILER CONNECTOR, SAFETY CHAINS, AND FLASHING_AMBER EMERGENCY LIGHT.COMPLETE WITH MANUAL TIT WINCH, ALUMINUM STORAGE BOX(664M), TRAILER TOOL KIT (TM-TK), AND TOWER GROUNDING_KIT (12-8GR). TOWER (T-50XXH), 46FT (15M), TELESCOPIC,ALUMINUM, CRANK-UP, CONSISTINGOF 2-25FT SECTIONS (D,E). COMPLETE WITH 2"OD X 8FT MAST_WITH FIXED PLATES. GUYED-WL: 70MPH, SA: 23 SQ FT, PL:200LBS. OVERALL TRANSPORTSIZE: 28'3"L X 8'4"W X 11'1"H. APPROX. SHIP WEIGHT: 4,105LBS._	55,250.00	55,250.00

Quote No.	Date	Cust No	Terms	Estimated Delivery	F.O.B.	Expiration
1602367	12/7/2016	UNI003	1/2D, BBS	8-10 WEEKS ARO	ORIGIN	60 DAYS

Item	QTY	Part	Description	Price $	Extension $
001	3	900515	TRAILER TOWER (51-20/T-50XXHD), GALVANIZED STEEL CHASSIS, 5'6"W X 16'11"L DECK WITH A-FRAME/T-BAR TONGUE, 2 WHEELELECTRIC BRAKES WITH BREAKAWAY KIT, 5,200LB GALVANIZEDTORSION AXLE (GVWR5,190LBS), ST235/85R16 RADIAL TIRES, GALVANIZED WHEELS,_ALUMINUM FENDERS, 6-HOLECOUPLER CHANNEL WITH 2-5/16BALL COUPLER, 5,000LB ZINCTONGUE JACK, AND ALUMINUM TREADBRITE DECKING. CONTAINS_ (4) SLIDEOUT OUTRIGGERS WITH(6) 8,000LB LEVELING JACKSW/ 7 FOOT PLATES. INCLUDESLED DOT LIGHTING, 7 PIN RV TYPE TRAILER CONNECTOR, SAFETY_CHAINS, AND FLASHING AMBEREMERGENCY LIGHT. COMPLETEWITH MANUAL TILT WINCH,ALUMINUM STORAGE BOX (664M), TRAILER TOOL KIT_(TM-TK), AND TOWER GROUNDINGKIT (12-8GR). TOWER (T-50XXHD), 50FT (15M),TELESCOPIC, ALUMINUM, CRANK-UP, CONSISTING OF 2-25FT_SECTIONS (D,E) WITH 4FT OFOVERLAP. COMPLETE WITH 2"OD X8 FT L MAST WITH FIXED PLATESAND WORM GEAR WINCH. OVERALL TRANSPORT SIZE: 26'11"L X_7'8"W X 10'3"H. APPROX. SHIPWEIGHT: 2,700LBS. GUYED- WL:70MPH, SA: 25 SQ FT, PL:300LBS	25,900.00	77,700.00

E-2. Aluma Tower Quote

The Following are a sample of quotes provided by DavidRound for custom winches to be used in the Mead system. They were used to estimate the cost for mobile system winches

DAVIDROUND
Engineered Handling Solutions Since 1869
10200 Wellman Rd• Streetsboro, OH • 44241
Tel: 330-656-1600 • Fax: 330-656-1601
E-mail: info@davidround.com

October 8, 2015

Number of pages including this page: ____

ATTENTION: Matt Newman
University of Nebraska
W342 NH
Lincoln, NE 68588-0526
Telephone: 402-394-1507
Fax:

PROJECT: Quote #MD100815.3-100H

Please refer to the above quote number when placing an order or when contacting David Round for additional information. I am pleased to quote the following:

PRODUCT SPECIFICATIONS:

David Round 203 Series Engineered Electric Wire Rope Winch

Model:	**203-.8-120**
Application:	**Pulling**
Usage:	**H4**
Capacity:	**800 LBS**
Line Speed:	**120 FPM**
Drum Storage Cap.:	**340 FT of 5/16" Diameter Wire Rope**
Wire Rope:	**Not Included**
Reeving:	**Single Line**
Drum Style:	**Grooved**
Drum Flanges:	**Dual Outer Flanges**
Motor:	**Motor**
Motor Brake:	**Spring-Applied / Electrically-Released AC Style Motor Brake**
Gearing:	**Fully-Sealed Gearing with Oil Bath Lubrication**
Controls:	**Controls in NEMA 4 enclosure including VFD programmed for 2 speed operation. VFD with capable of using a 0-10 VDC or 4-20 mA speed reference for use with customer supplied control system. Customer responsible for any wiring and/or parameter changes needed to use an outside speed reference signal.** **No pendant, dry contacts supplied for ON/OFF/IN/OUT control functions.**

also available from The David Round Company

	Controls shipped loose for remote mounting. **Note: Customer Responsible for Design and Integration of Electrical Controls for Multi – Unit Use**
Finish:	**Standard Safety Yellow Enamel**
Weight:	**TBD**
Voltage:	**230-3-60**

Price: $17,514.00 each net

Options:
Extended Warranty to 24 Months - $1800.00 each net

Recommended Spare Parts Available at Approval Drawing Sign Off

NOTES:

1) All orders and sales of goods supplied shall be subject to our standard Terms & Conditions of Sale attached. Terms inconsistent with those stated herein, which may appear on Purchaser's formal order, will not be binding on the Seller.
2) Pricing is valid 30 days unless otherwise noted.
3) Approval drawings, if applicable, must be signed and returned within 21 days for pricing to remain valid.
4) Equipment is built to order. Orders are non-cancellable & non-returnable upon acceptance of the purchase order. Cancellation fees will apply if the order is cancelled.
5) Products are offered on an FOB Shipping Point or EX WORKS basis. Prices quoted do not include inbound or outbound freight costs unless otherwise noted. Pricing also does not include duties, fees, customs charges, brokerage charges, legalization fees, insurance or export packaging costs. The Purchaser is responsible for all of these costs plus any redirection fees in the event of a change of delivery address.
6) Pricing does not include taxes. Any applicable taxes are the responsibility of the Purchaser.
7) Payment via "electronic check" is now accepted. We just need a copy of your check emailed to AR@DavidRound.com along with your PO number and contact information.
8) Credit cards accepted: VISA, MasterCard, and American Express. For customers wishing to pay for purchases by credit card a 2.5% convenience fee for the total purchase will be charged.
9) Our preferred carrier is ABF.

SHIPMENT: Best way prepaid and add - FOB factory
WARRANTY: 1 Year
PAYMENT TERMS: 50% down, 50% prior to shipment
DELIVERY: 10-12 weeks upon receipt of order and layout drawing approval (allow 1-2 weeks for submittals)

Regards: Matt Downing

DAVIDROUND
Engineered Handling Solutions Since 1869

10200 Wellman Rd• Streetsboro, OH • 44241
Tel: 330-656-1600 • Fax: 330-656-1601
E-mail: info@davidround.com

October 16, 2015

Number of pages including this page: ____

ATTENTION: Matt Newman
University of Nebraska
W342 NH
Lincoln, NE 68588-0526
Telephone: 402-394-1507
Fax:

PROJECT: Quote #MD100815.3-100Hrev1

Please refer to the above quote number when placing an order or when contacting David Round for additional information. I am pleased to quote the following:

PRODUCT SPECIFICATIONS:

David Round 203 Series Engineered Electric Wire Rope Winch

Model:	**203-.8-120**
Application:	**Pulling**
Usage:	**H4**
Capacity:	**800 LBS**
Line Speed:	**300 FPM**
Drum Storage Cap.:	**340 FT of 5/16" Diameter Wire Rope**
Wire Rope:	**Not Included**
Reeving:	**Single Line**
Drum Style:	**Grooved**
Drum Flanges:	**Dual Outer Flanges**
Motor:	**Motor**
Motor Brake:	**Spring-Applied / Electrically-Released AC Style Motor Brake**
Gearing:	**Fully-Sealed Gearing with Oil Bath Lubrication**
Controls:	**Controls in NEMA 4 enclosure including VFD programmed for 2 speed operation. VFD with capable of using a 0-10 VDC or 4-20 mA speed reference for use with customer supplied control system. Customer responsible for any wiring and/or parameter changes needed to use an outside speed reference signal.** **No pendant, dry contacts supplied for ON/OFF/IN/OUT control functions.**

	Controls shipped loose for remote mounting. **Note: Customer Responsible for Design and Integration of Electrical Controls for Multi – Unit Use**
Finish:	**Customer Specified Black Finish**
Weight:	**TBD**
Voltage:	**230-3-60**

Price: $20,939.00 each net

Options:
Extended Warranty to 24 Months - $1800.00 each net

Recommended Spare Parts Available at Approval Drawing Sign Off

NOTES:

1) All orders and sales of goods supplied shall be subject to our standard Terms & Conditions of Sale attached. Terms inconsistent with those stated herein, which may appear on Purchaser's formal order, will not be binding on the Seller.
2) Pricing is valid 30 days unless otherwise noted.
3) Approval drawings, if applicable, must be signed and returned within 21 days for pricing to remain valid.
4) Equipment is built to order. Orders are non-cancellable & non-returnable upon acceptance of the purchase order. Cancellation fees will apply if the order is cancelled.
5) Products are offered on an FOB Shipping Point or EX WORKS basis. Prices quoted do not include inbound or outbound freight costs unless otherwise noted. Pricing also does not include duties, fees, customs charges, brokerage charges, legalization fees, insurance or export packaging costs. The Purchaser is responsible for all of these costs plus any redirection fees in the event of a change of delivery address.
6) Pricing does not include taxes. Any applicable taxes are the responsibility of the Purchaser.
7) Payment via "electronic check" is now accepted. We just need a copy of your check emailed to AR@DavidRound.com along with your PO number and contact information.
8) Credit cards accepted: VISA, MasterCard, and American Express. For customers wishing to pay for purchases by credit card a 2.5% convenience fee for the total purchase will be charged.
9) Our preferred carrier is ABF.

SHIPMENT: Best way prepaid and add - FOB factory
WARRANTY: 1 Year
PAYMENT TERMS: 50% down, 50% prior to shipment
DELIVERY: 10-12 weeks upon receipt of order and layout drawing approval (allow 1-2 weeks for submittals)

Regards: Matt Downing

DAVIDROUND
Engineered Handling Solutions Since 1869

10200 Wellman Rd• Streetsboro, OH • 44241
Tel: 330-656-1600 • Fax: 330-656-1601
E-mail: info@davidround.com

October 20, 2015

Number of pages including this page: ____

ATTENTION: Matt Newman
University of Nebraska
W342 NH
Lincoln, NE 68588-0526
Telephone: 402-394-1507
Fax:

PROJECT: Quote #MD100815.3-100Hrev3

Please refer to the above quote number when placing an order or when contacting David Round for additional information. I am pleased to quote the following:

PRODUCT SPECIFICATIONS:

David Round 203 Series Engineered Electric Wire Rope Winch

Model:	**203-.8-120**
Application:	**Pulling**
Usage:	**H4**
Capacity:	**800 LBS**
Line Speed:	**300 FPM**
Drum Storage Cap.:	**340 FT of 5/16" Diameter Wire Rope**
Wire Rope:	**Not Included**
Reeving:	**Single Line**
Drum Style:	**Grooved**
Drum Flanges:	**Dual Outer Flanges**
Motor:	**10 HP Motor with Encoder Included**
Motor Brake:	**Spring-Applied / Electrically-Released AC Style Motor Brake**
Gearing:	**Fully-Sealed Gearing with Oil Bath Lubrication**
Controls:	**Controls in NEMA 4 enclosure including VFD programmed for 2 speed operation. VFD with capable of using a 0-10 VDC or 4-20 mA speed reference for use with customer supplied control system. Customer responsible for any wiring and/or parameter changes needed to use an outside speed reference signal.** **No pendant, dry contacts supplied for ON/OFF/IN/OUT control functions.**

	Controls shipped loose for remote mounting. **Note: Customer Responsible for Design and Integration of Electrical Controls for Multi – Unit Use**
Finish:	**Customer Specified Black Finish**
Weight:	**TBD**
Voltage:	**230-3-60**

Price: $22,374.00 each net

Options:
Stainless Steel Grooved Drum - $10,823.00 net
Powder Coating for entire unit - $1850.00 net
Extended Warranty to 24 Months - $2300.00 each net

Recommended Spare Parts Available at Approval Drawing Sign Off

NOTES:

1) All orders and sales of goods supplied shall be subject to our standard Terms & Conditions of Sale attached. Terms inconsistent with those stated herein, which may appear on Purchaser's formal order, will not be binding on the Seller.
2) Pricing is valid 30 days unless otherwise noted.
3) Approval drawings, if applicable, must be signed and returned within 21 days for pricing to remain valid.
4) Equipment is built to order. Orders are non-cancellable & non-returnable upon acceptance of the purchase order. Cancellation fees will apply if the order is cancelled.
5) Products are offered on an FOB Shipping Point or EX WORKS basis. Prices quoted do not include inbound or outbound freight costs unless otherwise noted. Pricing also does not include duties, fees, customs charges, brokerage charges, legalization fees, insurance or export packaging costs. The Purchaser is responsible for all of these costs plus any redirection fees in the event of a change of delivery address.
6) Pricing does not include taxes. Any applicable taxes are the responsibility of the Purchaser.
7) Payment via "electronic check" is now accepted. We just need a copy of your check emailed to AR@DavidRound.com along with your PO number and contact information.
8) Credit cards accepted: VISA, MasterCard, and American Express. For customers wishing to pay for purchases by credit card a 2.5% convenience fee for the total purchase will be charged.
9) Our preferred carrier is ABF.

SHIPMENT: Best way prepaid and add - FOB factory
WARRANTY: 1 Year
PAYMENT TERMS: 50% down, 50% prior to shipment
DELIVERY: 10-12 weeks upon receipt of order and layout drawing approval (allow 1-2 weeks for submittals)

DAVIDROUND
Engineered Handling Solutions Since 1869

10200 Wellman Rd• Streetsboro, OH • 44241
Tel: 330-656-1600 • Fax: 330-656-1601
E-mail: info@davidround.com

November 6, 2015

Number of pages including this page: ____

ATTENTION: Matt Newman
University of Nebraska
W342 NH
Lincoln, NE 68588-0526
Telephone: 402-394-1507
Fax:

PROJECT: Quote #MD100815.3-100Hrev5

Please refer to the above quote number when placing an order or when contacting David Round for additional information. I am pleased to quote the following:

PRODUCT SPECIFICATIONS:

David Round 203 Series Engineered Electric Wire Rope Winch

Model:	**203-.8-120**
Application:	**Pulling**
Usage:	**H4**
Capacity:	**800 LBS**
Line Speed:	**300 FPM**
Drum Storage Cap.:	**340 FT of ¼" Diameter Wire Rope**
Wire Rope:	**Not Included**
Reeving:	**Single Line**
Drum Style:	**Grooved**
Drum Flanges:	**Dual Outer Flanges**
Motor:	**10 HP Motor with Encoder and Fan/Blower Included**
Motor Brake:	**Spring-Applied / Electrically-Released AC Style Motor Brake**
Gearing:	**Fully-Sealed Gearing with Oil Bath Lubrication**
Controls:	**Controls in NEMA 4 enclosure including VFD programmed for 2 speed operation. VFD with capable of using a 0-10 VDC or 4-20 mA speed reference for use with customer supplied control system. Customer responsible for any wiring and/or parameter changes needed to use an outside speed reference signal.** **No pendant, dry contacts supplied for ON/OFF/IN/OUT control functions.**

	Controls shipped loose for remote mounting. **Note: Customer Responsible for Design and Integration of Electrical Controls for Multi – Unit Use**
Finish:	**Customer Specified Black Finish**
Weight:	**TBD**
Voltage:	**230-3-60**

Price: $23,271.00 each net

Options:
Stainless Steel Grooved Drum - $10,823.00 net
Powder Coating for entire unit - $1850.00 net
Extended Warranty to 24 Months - $2300.00 each net

Recommended Spare Parts Available at Approval Drawing Sign Off

NOTES:

1) All orders and sales of goods supplied shall be subject to our standard Terms & Conditions of Sale attached. Terms inconsistent with those stated herein, which may appear on Purchaser's formal order, will not be binding on the Seller.
2) Pricing is valid 30 days unless otherwise noted.
3) Approval drawings, if applicable, must be signed and returned within 21 days for pricing to remain valid.
4) Equipment is built to order. Orders are non-cancellable & non-returnable upon acceptance of the purchase order. Cancellation fees will apply if the order is cancelled.
5) Products are offered on an FOB Shipping Point or EX WORKS basis. Prices quoted do not include inbound or outbound freight costs unless otherwise noted. Pricing also does not include duties, fees, customs charges, brokerage charges, legalization fees, insurance or export packaging costs. The Purchaser is responsible for all of these costs plus any redirection fees in the event of a change of delivery address.
6) Pricing does not include taxes. Any applicable taxes are the responsibility of the Purchaser.
7) Payment via "electronic check" is now accepted. We just need a copy of your check emailed to AR@DavidRound.com along with your PO number and contact information.
8) Credit cards accepted: VISA, MasterCard, and American Express. For customers wishing to pay for purchases by credit card a 2.5% convenience fee for the total purchase will be charged.
9) Our preferred carrier is ABF.

SHIPMENT: Best way prepaid and add - FOB factory
WARRANTY: 1 Year
PAYMENT TERMS: 50% down, 50% prior to shipment
DELIVERY: 10-12 weeks upon receipt of order and layout drawing approval (allow 1-2 weeks for submittals)

Following are catalog pages for the motors and ESCs that DavidRound would have used for their winches.

14 AC Brakemotors – Technical Data

14.1 Key to the data tables

The following table lists the short symbols used in the "Technical Data DR AC Brakemotors" tables.

P_N	Rated power
T_N	Rated torque
n_N	Rated speed
I_N	Rated current
cosφ	Power factor
$\eta_{100\%}$	Efficiency at 100 % of the rated power
I_A/I_N	Starting current ratio
T_A/T_N	Starting torque ratio
T_H/T_N	Ramp-up torque ratio
Code Letter	NEMA code letter
J_{Mot}	Mass moment of inertia of the motor
J_{Mot_BE}	Mass moment of inertia of the brakemotor
BE..	Standard brake size
Z_0 BG	Switching frequency for operation with BG brake controller
Z_0 BGE	Switching frequency for operation with BGE brake controller
T_B	Standard brake torque
m	Mass of the motor
$m_{\_BE}$	Mass of the brakemotor

14.4 Technical data of 4-pole high efficiency motors

1800 rpm - S1

Motor type	P_N T_N [HP] [lb-in]	n_N [rpm]	I_N 230V [A]	I_N 460V [A]	I_N 575V [A]	cosφ	$\eta_{100\%}$ [%][1]	I_A/I_N	T_A/T_N T_H/T_N	Code Letter	J_{Mot} [10^{-3} lb-ft^2]	m [lb][2]
DRS71S4[3]	0.25 8.93	1700	0.9	0.45	0.36	0.69	72.0	4.2	1.9 1.9	G	11.6	17.2
DRS71S4[3]	0.33 12.3	1700	1.24	0.62	0.49	0.69	72.0	4.2	1.9 1.9	G	11.6	17.2
DRS71S4[3]	0.5 18.5	1700	1.84	0.92	0.74	0.69	72.0	4.2	1.9 1.9	G	11.6	17.2
DRS71M4[3]	0.75 27.4	1690	2.5	1.25	1.0	0.71	74.0	4.3	2.2 2.1	G	16.8	20.1
DRE80M4	1 36.2	1740	2.9	1.44	1.15	0.78	82.5	7.1	3 2.1	K	51	31.5
DRE90M4	1.5 53.1	1740	4.5	2.25	1.8	0.73	84.0	7.7	3.6 2.9	L	84.3	40.6
DRE90L4	2 72.5	1740	5.7	2.85	2.3	0.77	85.5	7.5	3.4 3.0	K	103	47.4
DRE100L4	3 107	1735	8.0	4.0	3.2	0.79	87.5	8.1	4 3.3	K	161	63.9
DRE100LC4	5 177	1750	12.9	6.5	5.2	0.83	87.5	7.6	2.5 2.3	J	213	68.4
DRE132S4	5.4 190	1765	13.8	6.9	5.5	0.81	88.5	8.7	2.9 2.5	K	451	102
DRE132M4	7.5 265	1755	18	9	7.2	0.85	89.5	8.1	2.5 1.6	J	605	132
DRE132MC4	10 358	1770	24.5	12.3	9.8	0.82	89.5	8.7	2.1 1.6	K	807	138
DRE160M4	12.5 438	1770	31	15.4	12.3	0.82	91.0	8	3 2.2	J	1068	196
DRE160MC4	15 522	1780	36.5	18.3	14.6	0.82	91.7	8.2	2.9 2	J	1401	207
DRE180M4	20 716	1775	47.5	24	19	0.86	91.7	7.4	2.6 1.9	H	2636	304
DRE180L4	25 885	1775	60	30	24	0.84	93.0	8.1	2.9 2.2	J	3087	335
DRE180LC4	30 1044	1780	71	35.5	28.5	0.84	93.0	7.6	2.4 1.8	J	3990	355
DRE200L4	40 1424	1780	99	49.5	39.5	0.82	93.0	7.4	2.6 2.1	J	5605	573
DRE225S4	50 1761	1775	119	59	47.5	0.84	93.0	7.2	2.7 2.0	H	6958	650
DRE225M4	60 2124	1780	142	71	57	0.85	93.6	7.3	2.8 1.9	H	8146	694

1) Efficiency levels according to IEC 60034-2-1 Ed. 1 (2007) / PLL from Residual Losses, NEMA MG1 and/or DoE
2) Applies for foot-mounted motor (DRS and DRE../FL..)
3) Standard efficiency motor

US DoE CC056A applies to DRE, DRP and DVE motors

Motor type	P_N T_N [HP] [lb-in]	n_N [rpm]	BE..	T_B [lb-in][3]	Z_0 BG[1] BGE[2] [1/h]	J_{Mot_BE} [10^{-3} lb-ft^2]	$m_{\_BE}$ [lb][4]
DRS71S4[5]	0.25 8.93	1700	BE05	22	4800 7600	14.7	22.5
DRS71S4[5]	0.33 12.3	1700	BE05	31	4800 7600	14.7	22.5
DRS71S4[5]	0.5 18.5	1700	BE05	44	4800 7600	14.7	22.5
DRS71M4[5]	0.75 27.4	1690	BE1	88	3300 8800	19.9	25.8
DRE80M4	1 36.2	1740	BE1	88	2800 7200	54.6	38.1
DRE90M4	1.5 53.1	1740	BE2	124	2400 6400	95	50.7
DRE90L4	2 72.5	1740	BE2	177	2400 6400	115	57.3
DRE100L4	3 107	1735	BE5	248	- 3000	175	77.2
DRE100LC4	5 177	1750	BE5	354	- 3000	228	81.6
DRE132S4	5.4 190	1765	BE5	487	- 2200	463	121
DRE132M4	7.5 265	1755	BE11	708	- 1600	629	165
DRE132MC4	10 358	1770	BE11	974	- 1200	843	172
DRE160M4	12.5 438	1770	BE20	1328	- 1000	1187	253
DRE160MC4	15 522	1780	BE20	1328	- 900	1520	264
DRE180M4	20 716	1775	BE20	1770	- 800	2778	374
DRE180L4	25 885	1775	BE30	2655	- 590	3420	423
DRE180LC4	30 1044	1780	BE30	2655	- 520	4322	441
DRE200L4	40 1424	1780	BE30 BE32	2655[6] 3540[7]	- 550	5938 6151	661 695
DRE225S4	50 1761	1775	BE30 BE32	2655[6] 4425[7]	- 320	7291 7505	738 771
DRE225M4	60 2124	1780	BE30 BE32	2655[6] 5310[7]	- 270	8479 8692	782 815

1) Operation with BG brake control system
2) Operation with BGE brake control system
3) Standard braking torque for IEC brakemotor
4) Applies for foot-mounted motor (DRS and DRE..BE../FI..)
5) Standard efficiency motor
6) Alternate reduced brake torque
7) Double-disc brake

US DoE CC056A applies to DRE, DRP and DVE motors

SMVector NEMA1 | Standard Duty Inverter

Lenze

RoHS COMPLIANT

World Class Control

Modes of Operation
- Open Loop Flux Vector, Speed or Torque Control with/without Auto Tuning
- V/Hz (Constant or Variable)
- Base Frequency Adjustable to Motor Specs
- Enhanced V/Hz with Auto-tuning

Acceleration/Deceleration Profiles
- Two Independent Accel Ramps
- Two Independent Decel Ramps
- Linear, S-Type
- Auxiliary Ramp(or Coast)-to-Stop

Fixed Accel Boost for Improved Starting

500 Hz Output Frequency

High Carrier (PWM Sine-Coded) Frequency
- 4, 6, 8, 10 kHz

Universal Logic Assertion (Selectable)
- Positive or Negative Logic Input
- Digital Reference Available

Braking Functions
- DC Injection Braking
- Optional Dynamic Braking
- Flux Braking w/ Adjustable Flux Level & Decel Time

Speed Commands
- Keypad, Potentiometer
- Jog, 8 Preset Speeds
- Floating Point Control
- Sequencer, 16 Segments
- Voltage: Scalable 0 –10 VDC
- Current: Scalable 4 – 20 mA

Process Control
- PID Modes: Direct and Reverse Acting
- PID Sleep Mode w/ Adjustable Recovery Threshold
- Analog Output (Speed, Load, Torque, kW)
- Network Speed (Baud Rate)
- Terminal and Keypad Status
- Elapsed Run or Power On Time (Hours)

Status Outputs
- Programmable Form "A" Relay Output
- Programmable Open Collector Output
- Scalable 0-10 VDC / 2-10 VDC Analog Output
- 4-20mA w/500 Ohm Total Impedance

Environment

Ambient Temperature
- -10 to 55°C
- Derate 2.5% per °C Above 40°C

Comprehensive Diagnostic Tools

Real Time Monitoring
- 8 Register Fault History
- Software Version
- Drive Network ID
- DC Bus Voltage (V)
- Motor Voltage (V)
- Output Current (%)
- Motor Current (A)
- Motor Torque (%)
- Power (kW)
- Energy Consumption (kWh)
- Heatsink Temperature (°C)
- 0 – 10 VDC Input (User Defined)
- 4 – 20 mA Input (User Defined)
- PID Feedback (User Defined)

Vigilant System Protection

Voltage Monitoring
- Low and High DC Bus V Protection
- Low Line V Compensation

Current Monitoring
- Motor Overload Protection
- Current Limiting Safeguard
- Ground Fault
- Short Circuit Protection

Four ReStarts
- Three Flying and One Auto
- User Enabled

Loss of Follower Management
- Protective Fault
- Go to Preset Speed or Preset Setpoint
- Initiate System Notification

Over Temperature Protection

International Voltages

+10/-15% Tolerance
120/240V, 1Ø
200/240V, 1 or 3Ø
200/240V, 3Ø
400/480V, 3Ø
480/600V, 3Ø

Global Standards

UL GOST
cUL C-Tick
CE Low Voltage (EN61800-5-1)
CE EMC (EN61800-3) with optional EMC filter

Keypad & Display

Simple Six Button Programming
- Start
- Stop
- Forward/Reverse
- Scroll Up
- Scroll Down
- Enter/Mode

Informative LED Display

Vivid Illumination
Easily Read from a Distance

Five Status LEDs
- Run
- Automatic Speed mode
- Manual Speed Mode
- Forward Rotation
- Reverse Rotation

Status Display
- Motor Status
- Fault Management
- Operational Information

NEMA1 (Up to 10HP) Keypad

NEMA1 (15HP and greater) Keypad

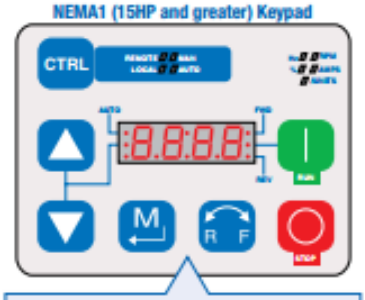

Additional CTRL Button

Switch between control modes
- Local-Manual
- Local Auto
- Remote-Manual
- Remote Auto

Additional LED Indicators

Define the units being displayed
- Hz
- RPM
- %
- Amps
- /Units

Control Terminals

Digital Inputs
- Dedicated Start/Stop
- (3) Programmable

Digital Outputs
- Form "A" Relay
- Open Collector

Analog Inputs
- 0 - 10 VDC
- 4 - 20 mA

Analog Outputs
- 0 - 10 VDC
- 2 - 10 VDC

Power Supplies
- 10 VDC Potentiometer Ref
- 12 VDC, 20 mA DI Ref or 0VDC Com
- 12 VDC, 50 mA Supply

Common

Additional Control Terminals (15 HP & up)

1 Programmable Digital Input
1 Common
RS-485 Modbus Communications
- TXA
- TXB

Lenze Americas • 630 Douglas Street • Uxbridge, MA 01569 • USA • Sales 800 217-9100 • Service 508 278-9100 • www.lenzeamericas.com

Lenze SMVector NEMA1 | Standard Duty Inverter

Ratings

120/240V* - 1Ø Input (3Ø Output)

Power		Output Current	NEMA1	
Hp	kW	I_a (A)	Model	Size
0.33	0.25	1.7	ESV251N01SXB	G1
0.5	0.37	2.4	ESV371N01SXB	G1
1	0.75	4.2	ESV751N01SXB	G1
1.5	1.1	6.0	ESV112N01SXB	G2

*120/240V models provide 0-230V output even with 120V input applied.

200/240V - 1 or 3Ø Input (3Ø Output)

Power		Output Current	NEMA1	
Hp	kW	I_a (A)	Model	Size
0.33	0.25	1.7	ESV251N02SXB***	G1
0.5	0.37	2.4	ESV371N02YXB	G1
1	0.75	4.2	ESV751N02YXB	G1
1.5	1.1	6.0	ESV112N02YXB	G2
2	1.5	7.0	ESV152N02YXB	G2
3	2.2	9.6	ESV222N02YXB	G2

***Model ESV251N02SXB is single-phase input only.

200/240V - 3Ø Input (3Ø Output)

Power		Output Current	NEMA1	
Hp	kW	I_a (A)	Model	Size
1.5	1.1	6.0	ESV112N02TXB	G2
2	1.5	7.0	ESV152N02TXB	G2
3	2.2	9.6	ESV222N02TXB	G2
5	4	16.5	ESV402N02TXB	G3
7.5	5.5	23	ESV552N02TXB	H1
10	7.5	29	ESV752N02TXB	H1
15	11	42	ESV113N02TXB	J1
20	15	54	ESV153N02TXB	J1

400/480V - 3Ø Input (3Ø Output)

Power		Output Current	NEMA1	
Hp	kW	I_a (A)	Model	Size
0.5	0.37	1.3/1.1	ESV371N04TXB	G1
1	0.75	2.4/2.1	ESV751N04TXB	G1
1.5	1.1	3.5/3.0	ESV112N04TXB	G2
2	1.5	4.0/3.5	ESV152N04TXB	G2
3	2.2	5.5/4.8	ESV222N04TXB	G2
5	4	9.4/8.2	ESV402N04TXB	G3
7.5	5.5	12.6/11	ESV552N04TXB	H1
10	7.5	16.1/14	ESV752N04TXB	H1
15	11	24/21	ESV113N04TXB	J1
20	15	31/27	ESV153N04TXB	J1
25	18.5	39/34	ESV183N04TXB	J1
30	22	46/40	ESV223N04TXB	J1
40	30	60/52	ESV303N04TXB	K1
50	37.5	75/65	ESV373N04TXB	K2
60	45	88/77	ESV453N04TXB	K3

600V - 3Ø Input (3Ø Output)

Power		Output Current	NEMA1	
Hp	kW	I_a (A)	Model	Size
1	0.75	1.7	ESV751N06TXB	G1
2	1.5	2.7	ESV152N06TXB	G2
3	2.2	3.9	ESV222N06TXB	G2
5	4	6.1	ESV402N06TXB	G3
7.5	5.5	9	ESV552N06TXB	H1
10	7.5	11	ESV752N06TXB	H1
15	11	17	ESV113N06TXB	J1
20	15	22	ESV153N06TXB	J1
25	18.5	27	ESV183N06TXB	J1
30	22	32	ESV223N06TXB	J1
40	30	41	ESV303N06TXB	K1
50	37.5	52	ESV373N06TXB	K2
60	45	62	ESV453N06TXB	K3

Dimensions

Dimensions

	H		W		D	
	in.	mm	in.	mm	in.	mm
G1	7.50	190	3.90	99	4.40	111
G2	7.60	191	3.90	99	5.50	138
G3	7.60	191	3.90	99	5.80	147
H1	9.90	250	5.20	130	6.30	160
J1	12.50	318	7.00	176	8.10	205
K1	14.19	360	8.72	221	10.07	256
K2	17.19	436	8.72	221	10.07	256
K3	20.19	513	8.72	221	10.07	256

SMV NEMA 1 (IP31)

Bottom Entry with IP21 Finger Guard

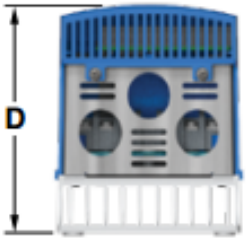

Bottom Entry with NEMA 1 (IP31) Steel Conduit Plate

Options

Communication Modules *

Item Number	Item Description
ESVZAC0	CANopen Communications Interface Module
ESVZAR0	RS-485/Modbus Communications Interface Module
ESVZAP0	PROFIBUS DP Communications Interface Module
ESVZAD0	DeviceNet Communications Interface Module
ESVZAE0	EtherNet/IP Communications Interface Module
* Only one Communication module can be installed and used at a time.	

Keypad

ESVZXK1	Remote Keypad w/ drive interface module & cable up to 10HP (7.5kW)
ESVZXH0	Remote Keypad w/ cable 15HP (11kW) and up

Additional I/O **

ESVZAL0	Additional Form C Relay Output Module
ESVZAL1	Additional I/O Module w/ 1 Form C Relay Output and 2 Digital Inputs
** Additional I/O modules cannot be used with Communication modules or Remote keypad ESVZXK1.	

Dynamic Braking Modules with Built-in Resistors

		Motor Voltage		
HP	(kW)	208 to 230 V Part Number	400 to 480 V Part Number	480 to 600 V Part Number
0.33 - 0.5	(0.25-0.37)	EZXDB3712A1	EZXDB3714A1	N/A
1 - 1.5	(0.75 - 1.1)	EZXDB1122A1	EZXDB1124A1	EZXDB1126A1
2 - 3	(1.5 - 2.2)	EZXDB2222A1	EZXDB2224A1	EZXDB2226A1
5	(4)	EZXDB4022A1	EZXDB4024A1	EZXDB4026A1
7.5	(5.5)	EZXDB5522A1	EZXDB5524A1	EZXDB5526A1
10	(7.5)	EZXDB7522A1	EZXDB7524A1	EZXDB7526A1

Dynamic Braking Modules without Built-in Resistors

15 - 20	(11 - 15)	EZXDC1532A1	N/A	N/A
15 - 30	(11 - 22)	N/A	EZXDC2234A1	EZXDC2236A1

Open Dynamic Braking Resistors with mounting brackets

15 - 20	(11 - 15)	841-009	841-009	841-010
25 - 30	(18.5 - 22)	N/A	841-011	841-012

APPENDIX F. CAD Models

As a part of this research, many devices were modeled and manufactured. The CAD files for many of those parts are available at:

https://app.box.com/s/glir42kh2cggnulvhijim4isz1jhprcs

The parts are split into two sections: one for the cable system and one for the IPASS end-effector. The following sub-assemblies may be found in the cable system directory:

- Tripod tower designs
- Final winch parts
- System layout
- IMU end-effector
- Pendulum/load-cell end-effector
- System controller

The IPASS directory contains files for both four propeller and six propeller configurations. Both directories should contain off-the-shelf components with McMaster part numbers in the part names. The circuitry used for all of these devices were made using protoboard. As a result, no formal drawings exist for their design. Videos and images of the circuits are available in the CAD directory listed above.